USGS
science for a changing world

هيئة المساحة الجيولوجية السعودية
SAUDI GEOLOGICAL SURVEY

Thickness of the Saudi Arabian Crust

Chapter M of
Active Volcanism on the Arabian Shield—Geology, Volcanology, and Geophysics of Northern Harrat Rahat and Vicinity, Kingdom of Saudi Arabia

U.S. Geological Survey Professional Paper 1862
Saudi Geological Survey Special Report SGS–SP–2021–1

U.S. Department of the Interior
U.S. Geological Survey

Cover. Photograph looking east-northeast at a wadi floored by the mugearite of Um Znabah 2 (196 kilo-annum [ka]) and overlain by the trachyte of Al Efairia (88 ka), the largest pyroclastic deposit mapped in northern Harrat Rahat. The mugearite of Um Znabah 2 forms rubbly outcrops in the middle distance and flows around the tallest mountain on the skyline, composed of Proterozoic marble. All hills and mountains on the skyline are metamorphosed Proterozoic sedimentary and volcanic deposits of the Furayh Group (Hijaz terrane). U.S. Geological Survey photograph by T.W. Sisson, February 12, 2014. Background image shows northern Harrat Rahat lava flows, maars, and lava domes. U.S. Geological Survey photograph by Andrew Calvert, January 25, 2012.

Thickness of the Saudi Arabian Crust

By Alexander R. Blanchette, Simon L. Klemperer, Walter D. Mooney, and Hani M. Zahran

Chapter M of

Active Volcanism on the Arabian Shield—Geology, Volcanology, and Geophysics of Northern Harrat Rahat and Vicinity, Kingdom of Saudi Arabia

Edited by Thomas W. Sisson, Andrew T. Calvert, and Walter D. Mooney

U.S. Geological Survey Professional Paper 1862
Saudi Geological Survey Special Report SGS–SP–2021–1

U.S. Department of the Interior
U.S. Geological Survey

U.S. Geological Survey, Reston, Virginia: 2023

For more information on the USGS—the Federal source for science about the Earth, its natural and living resources, natural hazards, and the environment—visit https://www.usgs.gov or call 1–888–ASK–USGS.

For an overview of USGS information products, including maps, imagery, and publications, visit https://store.usgs.gov.

Suggested citation:
Blanchette, A.R., Klemperer, S.L., Mooney, W.D., and Zahran, H.M., 2023, Thickness of the Saudi Arabian crust, chap. M *of* Sisson, T.W., Calvert, A.T., and Mooney, W.D., eds., Active volcanism on the Arabian Shield—Geology, volcanology, and geophysics of northern Harrat Rahat and vicinity, Kingdom of Saudi Arabia: U.S. Geological Survey Professional Paper 1862 [also released as Saudi Geological Survey Special Report SGS–SP–2021–1], 49 p., https://doi.org/10.3133/pp1862M.

ISSN 1044-9612 (print)
ISSN 2330-7102 (online)

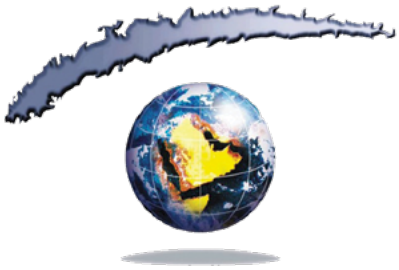

هيئة المساحة الجيولوجية السعودية
SAUDI GEOLOGICAL SURVEY

Ministry of Industry and Mineral Resources
BANDAR BIN IBRAHIM BIN ABDULLAH AL-KHORAYEF, Minister and SGS Chairman

Saudi Geological Survey
Abdullah bin Mufter Al-Shamrani, Chief Executive Officer

Saudi Geological Survey, Jiddah, Kingdom of Saudi Arabia: 2023

Contents

Figures

Tables

Conversion Factors

International System of Units to U.S. customary units

Multiply	By	To obtain
	Length	
meter (m)	3.281	foot (ft)
meter (m)	1.094	yard (yd)
kilometer (km)	0.6214	mile (mi)
	Area	
square kilometer (km^2)	247.1	acre
square kilometer (km^2)	0.3861	square mile (mi^2)
	Volume	
cubic kilometer (km^3)	0.2399	cubic mile (mi^3)
	Flow rate	
kilometer per second (km/s)	0.6214	mile per second (mi/s)

Temperature in degrees Celsius (°C) may be converted to degrees Fahrenheit (°F) as follows:

$$°F = (1.8 \times °C) + 32.$$

Abbreviations

1D	one dimensional
A.H.	in the year of the Hijra
CCP	common conversion point
C.E.	Common Era
H_0	null hypothesis
H_1	alternative hypothesis
Hz	hertz
IRIS	Incorporated Research Institutions for Seismology
LAB	lithosphere-asthenosphere boundary
Ma	mega-annum
MMN	Makkah-Madīnah-Nafud volcanic line
Moho	Mohorovičić discontinuity
M_w	moment magnitude
MWU	Mann-Whitney U test
NEZ	north-east-vertical coordinate system
PASSCAL	Portable Array Seismic Studies of the Continental Lithosphere
PDF	probability density function
PRF	P-wave receiver function
PWS	phase-weighted stacking
RTZ	radial-transverse-vertical coordinate system
SGS	Saudi Geological Survey
s	second
s/km	second per kilometer
USGS	U.S. Geological Survey
V_P	P-wave (pressure) velocity
V_S	S-wave (shear) velocity

Active Volcanism on the Arabian Shield
Edited by T.W. Sisson, A.T. Calvert, and W.D. Mooney
U.S. Geological Survey Professional Paper 1862
Saudi Geological Survey Special Report SGS–SP–2021–1

Chapter M

Thickness of the Saudi Arabian Crust

By Alexander R. Blanchette,[1] Simon L. Klemperer,[1] Walter D. Mooney,[2] and Hani M. Zahran[3]

Abstract

As part of a joint Saudi Geological Survey (SGS) and U.S. Geological Survey (USGS) project, we analyzed P-wave receiver functions from seismic stations covering most of the Kingdom of Saudi Arabia to map the thickness of the crust across the Arabia Plate. We present an update of crustal-thickness estimates and fill in gaps for the western Arabian Shield and the rifted margin at the Red Sea (the coastal plain), as well as the eastern Arabian Platform. We applied a conventional *H-k* stacking algorithm and included careful attention to stacking weights, two forms of sedimentary corrections for stations located on the Arabian Platform, and additional processing for noisy stations. We obtained useful results at 154 stations from 898 teleseismic events over a 2-year period from 1995–1997 (for non-SGS stations) and a 6-year period from 2008–2014 (for SGS stations). Average crustal thickness (that is, depth to the Mohorovičić discontinuity [Moho] below the surface) beneath the Red Sea coastal plain (the rift margin) is 29 kilometers (km), beneath the volcanic fields (known in Arabic as harra [plural] or harrat [singular]) is 35 km, beneath the Arabian Shield (excluding harrats) is 37 km, and beneath the Arabian Platform is 38 km. Crustal thinning appears not to extend east of the rift escarpment, suggesting uniform extension that is no broader at depth than at the surface. In contrast to some previous claims that the Arabian Platform crust is thicker than that of the Arabian Shield, we find no statistically significant difference between their whole crustal thicknesses. However, the average subsedimentary crustal thickness (that is, the crystalline crust) for stations on the Arabian Platform is 34 km, 3 km thinner than the crust of the Arabian Shield. Individual station P-wave (pressure) velocity and S-wave (shear) velocity ratios (V_P/V_S) are highly variable for the Arabia Plate, ranging from 1.60 to 1.97 and averaging 1.75, with a standard deviation of 0.07. There are no statistically significant differences between V_P/V_S ratios of the different geologic regions of Saudi Arabia. Similar V_P/V_S ratios, coupled with similar crustal thicknesses for harrats and the Arabian Shield, indicate that Cenozoic magmatism has contributed negligibly to crustal growth.

Introduction

The present-day thickness and composition of the Earth's crust and its lateral variability are the product of its evolution from initial formation and evolution through multiple tectonic episodes. As part of a joint Saudi Geological Survey (SGS) and U.S. Geological Survey (USGS) project, we sought to infer the thickness of the present-day Arabia Plate crust with minimal assumptions. We computed P-wave receiver functions (PRFs) and measured the traveltime differences between teleseismic P-waves and the converted phases (Ps, 3p1s, 2p2s) they generated at the boundary between the crust and mantle (that is, the Mohorovičić discontinuity [Moho]). Compared to previous PRF studies of crustal thickness of the Kingdom of Saudi Arabia (Sandvol and others, 1998; Julià and others, 2003; Al-Damegh and others, 2005; Tkalčić and others, 2006; Tang and others, 2016, 2019), we: (1) use more stations that were active for a longer recording period, (2) more thoroughly explore the methodological parameter space to obtain estimates of uncertainties, (3) correct for sedimentary cover where known, and (4) make statistical comparisons between different geologic regions.

The Arabian Shield constitutes the eastern part of the Arabian-Nubian Shield and is separated from the Nubian Shield by the Red Sea rift, a divergent plate boundary that merges with the Dead Sea Transform boundary at its north end (fig. 1*B*). The Arabian-Nubian Shield was formed by the accretion of multiple terranes, primarily around 800–550 million years ago (Ma) (Stern and Johnson, 2010). The Arabian craton began to subside at 725 Ma and its eastern and northern parts gradually accumulated as much as 15 kilometers (km) of sediments (Konert and others, 2001, summarized by Stern and Johnson, 2010). The arrival of the Afar plume at ~30 Ma triggered extension in East Africa, the Gulf of Aden, and the Red Sea region (Bosworth and others, 2005; Bosworth, 2015). Voluminous flood basalts in Ethiopia

[1]Stanford University.

[2]U.S. Geological Survey.

[3]Saudi Geological Survey.

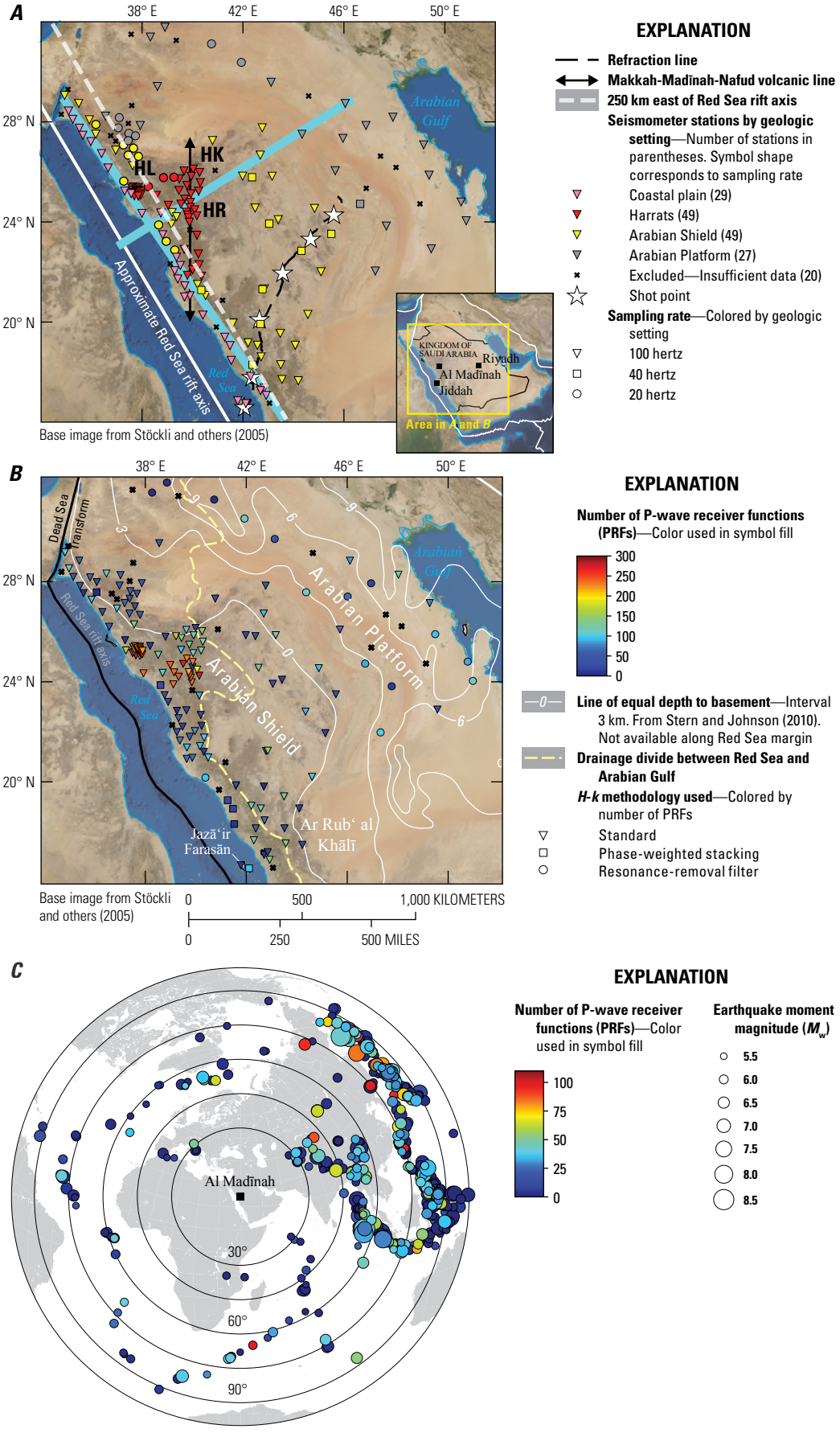

Figure 1. Maps of the study area in the Kingdom of Saudi Arabia and earthquakes analyzed in this study. Inset map shows plate boundaries in white. *A*, True-color image map showing the locations of Saudi Geological Survey (SGS) and Incorporated Research Institutions for Seismology (IRIS) Portable Array Seismic Studies of the Continental Lithosphere (PASSCAL) seismometers. Harrats are named following Camp and others (1991): HL, Harrat Lunayyir; HK, Harrat Khaybar; HR, Harrat Rahat. Common-conversion-point (CCP) profiles parallel and orthogonal to the Red Sea rift shown by thick aqua lines (drawn to be 50 kilometers [km] wide, the region stacked in CCP images in fig. 8) were drawn to maximize station density rather than to be truly parallel or orthogonal to the straight-line approximation of the Red Sea rift axis (white line). Refraction line and shot points from Healy and others (1983). *B*, Map showing the 154 seismic stations for which we report crustal thickness. The drainage divide between the Red Sea and the Arabian Gulf corresponds to the Great Escarpment south of Jiddah, and in that region is close to the dashed white line in *A*, 250 km from the Red Sea rift. *C*, Polar plot of earthquakes used in this analysis.

and Yemen were succeeded in Syria, Saudi Arabia, Jordan, and Yemen by expansive but generally thin alkali-basalt fields, known in Arabic as harra (plural) or harrat (singular) (Coleman, 1993; Bosworth and others, 2005; Bosworth, 2015). Recent magmatism was recorded in the 2009 intrusion event at Harrat Lunayyir and by historical eruptions at Harrat Rahat in 1256 C.E. (654 in the year of the Hijra [A.H.]) and probably at Harrat Khaybar in 641 C.E. (20 A.H.), which are located along the Makkah-Madīnah-Nafud (MMN) volcanic line (fig. 1*A*) (Camp and Roobol, 1992; Pallister and others, 2009; Champion and others, 2023; Stelten and others, 2023), as well as by a possible eruption near Dhamār, Yemen, in 1937 C.E. (Neumann van Padang, 1963).

In this chapter we discuss the newly expanded seismic dataset and then the calculation of receiver functions, including data quality control. We obtained useful results at 154 stations (fig. 1*A*, *B*) from 898 teleseismic events (fig. 1*C*) over a 2-year period from 1995–1997 (for non-SGS stations) and a 6-year period from 2008–2014 (for SGS stations). We describe the standard *H-k* stacking approach that measures crustal thickness and crustal pressure-wave (P-wave) to shear-wave (S-wave) velocity ratio (V_P/V_S ratio) from conversions between P- and S-waves, along with four key improvements over previous work in Saudi Arabia: (1) careful analysis of the effects of the chosen stacking weights; (2) use of a resonance-removal filter (Yu and others, 2015), followed by a sedimentary *H-k* stack on stations whose signals are difficult to analyze owing to sedimentary reverberations; (3) application of phase-weighted stacking (PWS) (Crotwell, 2007) for noisy signals; and, most importantly, (4) application of an additional sedimentary correction based on the well-mapped sedimentary thicknesses of the Arabian Platform (Konert and others, 2001 [reproduced by Stern and Johnson, 2010]). We discuss the statistical approach to determine if apparent differences between subsets of the data are real, and then present the results by geologic setting.

Data and Methods

Preprocessing and Quality Control

We examined data from 165 broadband seismic stations of the SGS National Seismic Network (Endo and others, 2007) that are now deployed in all of Saudi Arabia except for Ar Rub‘ al Khālī (Empty Quarter) (fig. 1*B*), the vast sand desert in the southern part of the Arabian Peninsula. In addition to the SGS seismic stations, we have also incorporated nine seismic stations from an Incorporated Research Institutions for Seismology (IRIS) Portable Array Seismic Studies of the Continental Lithosphere (PASSCAL) array from 1995–1997 (Vernon, 1995). The recorders used by both SGS and IRIS are Trillium T40 and T120 and Streckeisen STS2 seismometers (Blanchette and others, 2023). We obtained useful results at 154 stations (fig. 1*A*, *B*) from 898 teleseismic events (fig. 1*C*) over a 2-year period from 1995–1997 (for the IRIS-PASSCAL stations), and a 6-year period from 2008–2014 (for the SGS stations). We were unable to derive meaningful results at the remaining 20 stations that are not further considered here (table 1). Each three-component recording was used to construct a PRF (Langston, 1979). The PRF method is a well-established technique to image seismic boundaries within the lithosphere, including the Moho and the base of sedimentary rocks that overlie the crystalline crust.

We rotated event recordings from their north-east-vertical (NEZ) coordinate system to the radial-transverse-vertical (RTZ) coordinate system, based on the theoretical back azimuth of each recorded teleseismic earthquake, in order to isolate the first arrival (P-wave) on the vertical component and the converted S-wave on the radial component. We picked arrival times for every station-event pair using a short-term average (STA) over long-term average (LTA) algorithm (Earle and Shearer, 1994), and manually refined these arrival times to correct for slight errors in the picking algorithm by visually inspecting the data.

We band-pass filtered the raw data from 0.2 to 1.5 hertz (Hz) and trimmed the filtered traces such that each trace begins 20 seconds (s) before the first P-wave arrival and extends to 80 seconds after. PRFs were calculated by deconvolving the vertical (Z) signal from the radial (R) signal using an iterative-time domain approach (Ligorria and Ammon, 1999). Some previous workers simply visually inspected the calculated PRFs for quality assurance (for example, Sandvol and others, 1998; Thurner and others 2015; Miller and others, 2018); Tang and others (2016) used a minimum-fit criterion. In this study, we quantitatively used both a minimum-fit criterion and a cross-correlation filter.

The minimum-fit criterion required that we were able to reproduce the radial and transverse components of motion with a fit that is equal to or better than 70 percent when we convolve the respective components of the PRF with the vertical component. The 70 percent minimum-fit criterion is chosen to enforce a decent match between the original signal and the PRF that does not discard an excessive amount of data. The initial dataset was composed of 22,716 receiver functions and 18,242 (~80 percent) of the receiver functions met the 70 percent minimum-fit requirement. The cross-correlation filter constructs a template PRF by stacking all PRFs for a given station and calculates the maximum cross-correlation coefficient of each event with the template. To minimize assumptions about the structure beneath each station, no moveout correction was applied to the PRFs, and we required a low minimum-threshold cross-correlation coefficient of 0.6 on the radial component of the PRFs only. Of the 18,242 receiver functions that passed the minimum-fit criteria, 15,519 (~68 percent of the raw dataset) passed the cross-correlation filter requirement. The final number of receiver functions that passed both the minimum-fit and the cross-correlation filter requirements is far lower on the Arabian Platform (~11 percent of the final usable PRFs) than on the Arabian Shield (~24 percent) or in the harrats (~51 percent; fig. 1*B*).

A very high proportion of the useable receiver functions was generated by moment magnitude (M_w) >6 subduction zone earthquakes northeast of the recording array (fig. 1*C*), compared to the less numerous and smaller midocean ridge events at most other back azimuths.

Standard *H-k* Stacking

PRFs utilize teleseismic P-wave energy from earthquakes that are 30–90° away from the receiver. Some of the P-wave energy is converted to transmitted S-wave motion at first-order (abrupt) impedance boundaries in the lithosphere. This S-wave is denoted Ps (capital letters denote waves that are initially down-going and lowercase letters indicate purely up-going waves). Three other arrivals (also called multiples) are also commonly observed on higher quality P-wave receiver functions: the PpPs (or 3p1s) arrival, and two phases that arrive together (for a one dimensional [1D] Earth model) with the same sense of motion (PsPs and PpSs) and are collectively referred to as 2p2s (fig. 2). The piercing point at the Moho varies between phases and with the earthquake distance but is farthest away from the seismic station (about 50 km; fig. 2*C*) for the 3p1s multiple at the shortest teleseismic offset used, here 30°. For clarity, we denote the depth of the interface at which the waves are refracting and converting with a subscript (for example, $P_{35}s$ is a P-to-S conversion at 35 km depth). The traveltimes (t, in seconds [s]) of each phase as a function of crustal thickness (H, in kilometers [km]), P-wave velocity (V_p, in kilometers per second [km/s]), V_p/V_S ratio (k), and ray parameter (p, in seconds per kilometer [s/km]) are given by equations 1–3:

$$t_{Ps}\left(H,\ k,\ V_P, p\right) = H\left[\sqrt{\frac{k^2}{V_P^2} - p^2} - \sqrt{\frac{1}{V_P^2} - p^2}\right] \quad (1)$$

$$t_{3p1s}\left(H,\ k,\ V_P, p\right) = H\left[\sqrt{\frac{k^2}{V_P^2} - p^2} + \sqrt{\frac{1}{V_P^2} - p^2}\right] \quad (2)$$

$$t_{2p2s}\left(H,\ k,\ V_P, p\right) = 2H\sqrt{\frac{k^2}{V_P^2} - p^2} \quad (3)$$

H-k stacking (Zhu and Kanamori, 2000) is a standard approach used to analyze PRFs for H and k beneath a given seismic station, normally assuming a homogenous isotropic layer over a half-space beneath the seismic station. Standard *H-k* stacking employs a grid search across *H-k* space for the stacking amplitude at a single station:

$$s\left(H,\ k\right) = \frac{1}{N}\sum_{n=1}^{N}\left[w_1 r_n\left(t_{Ps}\right) + w_2 r_n\left(t_{3p1s}\right) - w_3 r_n\left(t_{2p2s}\right)\right] \quad (4)$$

where

s is the stack amplitude sum,

r_n is the amplitude of the nth radial receiver function for the station at the predicted phase arrival time for the appropriate H, k, V_p, and p values,

w_i is the stacking weight for each phase i, and

N is the number of receiver functions.

The normalization condition applied to the stacking weights is $w_1 + w_2 + w_3 = 1$, and we describe *H-k* stacks and their results as "$w_1/w_2/w_3$" to emphasize the weights used. The third term of equation 4 represents the 2p2s phases and is subtracted because it has the opposite polarity with respect to the other phases. The sum, s, reaches its maximum value for any seismic station at the average crustal thickness and velocity ratio beneath that station.

We searched over a grid spanning $20 \le H \le 80$ km and $1.60 \le k \le 2.10$ to sample all plausible crustal thicknesses and compositions, using an assumed average crustal wavespeed (V_{Pavg} = 6.5 km/s; Mooney and others, 1985). *H-k* estimates vary only weakly with V_{Pavg}, increasing H by less than ~10 km per km/s and k by less than ~0.05 per km/s (Karplus and others, 2019). Conventionally, the uncertainty in H and k values is computed by:

$$\sigma_H^2 = 2\sigma_s\left(\frac{\partial^2 s}{\partial H^2}\right)^{-1} \quad (5)$$

$$\sigma_k^2 = 2\sigma_s\left(\frac{\partial^2 s}{\partial k^2}\right)^{-1} \quad (6)$$

where σ_H, σ_k, and σ_s are the standard deviations of H, k, and the stack amplitude (s) evaluated at the H and k values that maximize the stack (Zhu and Kanamori, 2000).

We cite uncertainties of two standard deviations (±2σ) throughout this paper for individual stations and in tables 2–7, except in the "Discussion" section, where we cite uncertainties of ±1σ (tables 8 and 9) for ensemble means.

It is common to use a default set of stacking weights, regardless of the signal-to-noise ratios of the different phases at different stations (see for example, Al-Damegh and others, 2005; Karplus and others, 2019). Instead, we examined the individual contribution of each converted phase at each station to determine the final weights, selecting from among three options (0.4/0.3/0.3, 0.33/0.33/0.33, and 0.5/0.5/0.0) to give the sharpest peak in *H-k* space for the Moho conversions, after Ogden and others (2019). Additional combinations were used to stack shallower conversions, within or at the base of the sedimentary cover, as discussed below. For example, at Arabian Shield station AFFS (fig. 3; table 6), each phase (fig. 3*C–E*) provides clean constraints in *H-k* space. We

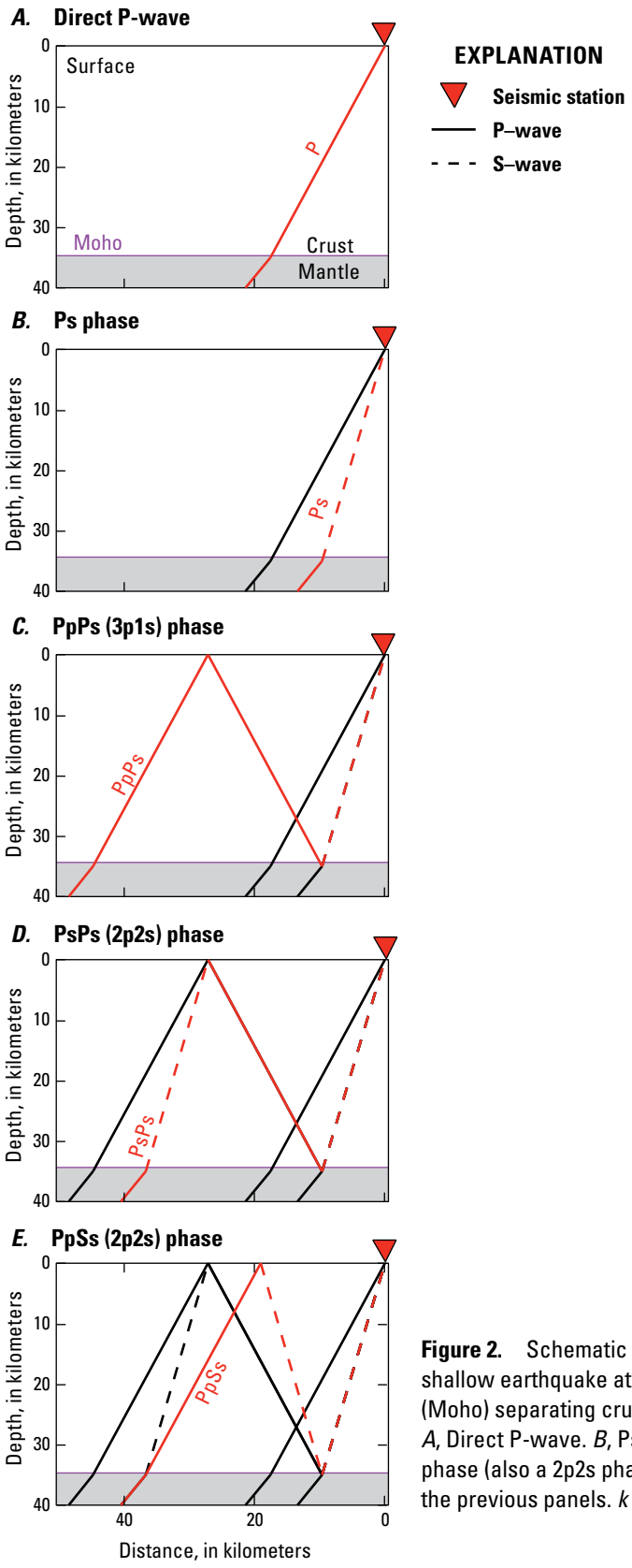

Figure 2. Schematic diagrams of ray paths of P-wave receiver function phases from a shallow earthquake at 30° distance for a 35-kilometer (km)-deep Mohorovičić discontinuity (Moho) separating crust (V_P = 6.1 km/s, k = 1.73) and upper mantle (V_P = 8.04 km/s, k = 1.80). *A*, Direct P-wave. *B*, Ps phase. *C*, PpPs (or 3p1s) phase. *D*, PsPs (or 2p2s) phase. E, PpSs phase (also a 2p2s phase). Red lines are the labelled phase; black lines are the phase(s) in the previous panels. $k = V_P/V_S$ ratio, where V_P is P-wave velocity and V_S is S-wave velocity.

generated *H-k* solutions for multiple combinations of weights and compared the predicted moveout curves of each phase for each *H-k* solution with the data to ensure the *H-k* solutions represent stacked coherent signal, not noise (fig. 4). For station AFFS, our preferred weights are 0.4/0.3/0.3 (fig. 3*F*).

In contrast to station AFFS, at coastal station MWLHS (fig. 5; table 5), the 2p2s phases provide potentially misleading information (fig. 5*E*), and our preferred stacking weights are 0.5/0.5/0.0. We illustrate this issue in figure 6, where the 2p2s stack (fig. 5*E*) suggests possible Moho depths of about 21 km or about 43 km. However, the predicted $2p_{21}1s$ and $2p_{43}1s$ arrivals (where subscripts denote depth of model converter) correspond to unusually high amplitudes on the more numerous PRFs with a small slowness of $p \approx 0.45$ s/km (the most distant earthquakes from the northeast) and not to any corresponding negative (blue in fig. 6) amplitudes on the sparse PRFs with larger p. Hence, we ignore the 2p2s stack in selecting the final weights of 0.5/0.5/0.0 (fig. 5*F*). It should be noted that although standard deviations calculated via equations 5 and 6 are appropriate for well-resolved *H-k* plots with sub-equal contributions from the various phases (for example, figs. 3F, 5F), they are gross underestimates for poor data quality particularly where only a single phase is available or dominates the stacks (for example, figs. 3*C–E*, 5*C*–E). For station AFFS, our preferred result (H = 35.2±0.4 km, k = 1.75±0.02) is 8 σ_H and 6 σ_k from the value given by only the Ps phase (fig. 3*C*).

Multiple Removal to Improve *H-k* Stacking

Standard *H-k* stacking works well at recovering the thickness of the crust, provided that the Moho is the only layer with a sharp enough impedance contrast to generate strong P-wave to S-wave conversions (Langston, 2011; Yu and others, 2015) and that the crust can be reasonably well-characterized with a single average wavespeed. However, some stations on the Arabian Platform are underlain by as much as 10 km of low-wavespeed sedimentary rocks (fig. 1*B*) (Konert and others, 2001 [reproduced by Stern and Johnson, 2010]), producing interbed conversions and multiples (reverberations) that can interfere with the Moho Ps arrival and its subsequent multiples. A significant number (15 out of 154) of the seismic stations successfully analyzed here were affected by sedimentary multiples and required additional analysis.

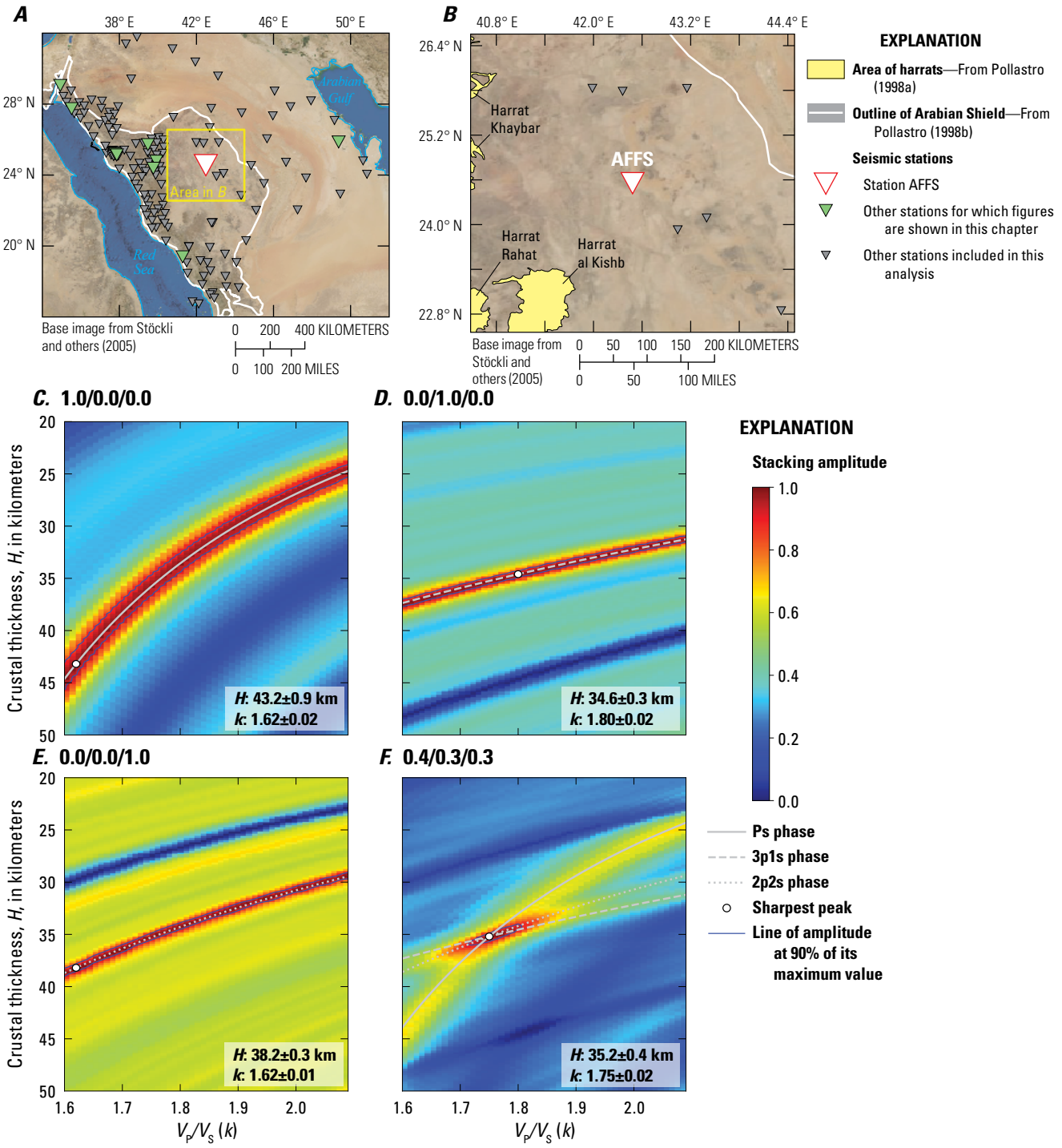

Figure 3. Location maps and plots of the receiver function analysis for Arabian Shield seismic station AFFS in the Kingdom of Saudi Arabia (table 6). *A*, Map of the Arabian Peninsula region. *B*, Zoomed-in map of the region around station AFFS. *C*, Plot of Ps single-phase *H-k* stack (with $w_1/w_2/w_3$ stacking weights of 1.0/0.0/0.0). *D*, Plot of 3p1s single-phase *H-k* stack (0.0/1.0/0.0). *E*, Plot of 2p2s single-phase *H-k* (0.0/0.0/1.0). *F*, Plot of optimized *H-k* stack (0.4/0.3/0.3) indicating a crustal thickness (*H*) of 35.2±0.4 kilometers (km) and V_P/V_S ratio (*k*) of 1.75±0.02. V_P is P-wave velocity and V_S is S-wave velocity; %, percent.

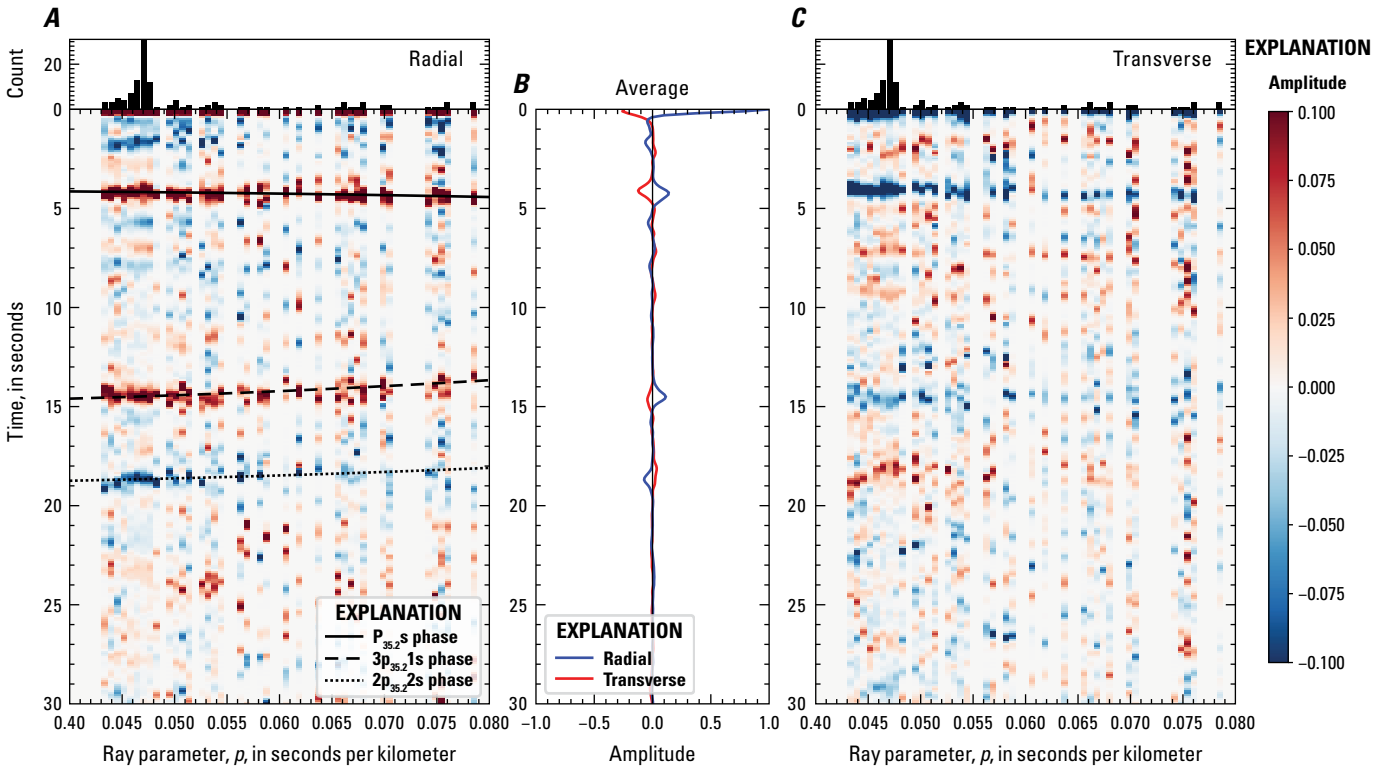

Figure 4. Plots of P-wave receiver function (PRF) gathers for Arabian Shield seismic station AFFS in the Kingdom of Saudi Arabia (fig. 3; table 6). *A*, Radial component of PRFs versus ray parameter (*p*). Individual PRFs are normalized to the maximum amplitude within the time window shown, binned, and normalized by the number of traces per bin (count). *B*, Average of all individual normalized radial and transverse components of PRFs. Transverse components additionally multiplied by 0.3. *C*, Transverse component of PRFs versus ray parameter, normalized as in part *A* and multiplied by 0.3 as in part *B*. Multiplication by 0.3 is an arbitrary scaling to make the normalized energy on the radial plot (part *A*) and transverse plot (part *C*) easier to compare. Note that all panels share the same time axis.

We attempted direct removal of the sedimentary reverberations from these PRFs using a resonance-removal filter calculated from the autocorrelations of the PRFs (Yu and others, 2015). This method estimates the apparent thickness and V_P/V_S ratio of the sedimentary layer, as well as a thickness and V_P/V_S ratio for the subsedimentary crystalline crust. This approach works best for sedimentary layers thicker than ~0.25 km for which the reverberations have frequencies and traveltimes that interfere with the Moho conversions. However, this method may be inapplicable for layers thicker than ~8 km for which the wavespeed contrast at the sediment-basement contact is sufficiently small or gradational that the reverberations do not have a high amplitude. We successfully filtered 15 stations with 2.6–10.7 km of sedimentary rock (Konert and others, 2001 [reproduced by Stern and Johnson, 2010]). We then determined the crustal thicknesses using the *H-k* method on the filtered PRFs.

As in conventional *H-k* stacking, to get sedimentary thickness, we assumed a sedimentary P-wave velocity of 4.0 km/s based on refraction-profiling results showing $2.0 \leq V_P \leq 5.7$ km/s in the northern Arabian Platform (Seber and others, 1993; Brew and others, 1997) and 3–5 km/s within the western Arabian Platform (Mooney, 1984), and carried out a grid search across *H-k* space. The sedimentary thickness, h_s, is determined reasonably well by the Ps conversion from the sediment-basement interface, but determining the sedimentary V_P/V_S ratio, k_s, requires good constraints on the corresponding 3p1s and 2p2s multiples that tend to have low amplitudes (for example, see fig. 23*F*, where h_s is well constrained and V_P/V_S ratio is virtually unconstrained).

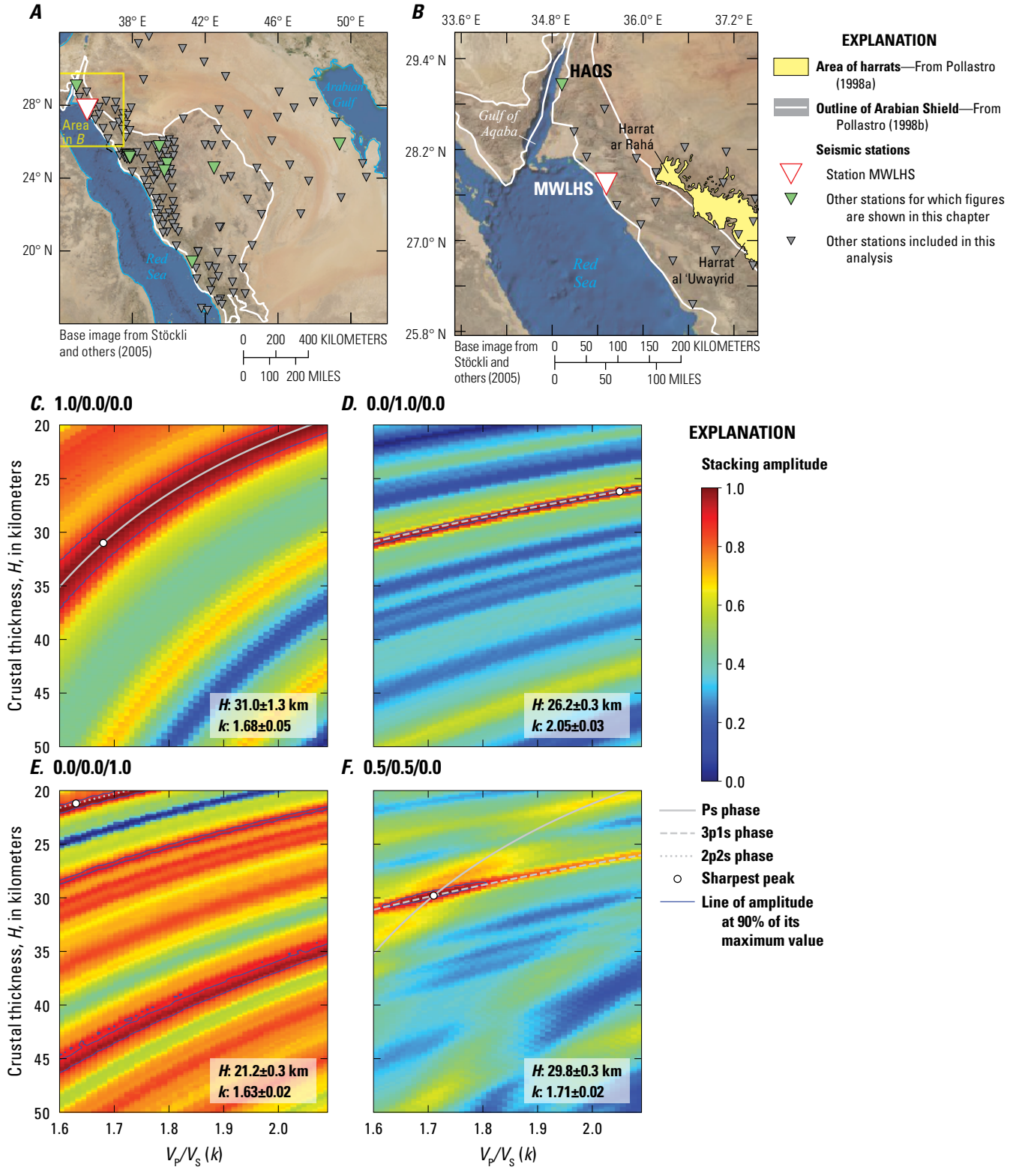

Figure 5. Location maps and plots of receiver function analysis for coastal seismic station MWLHS in the Kingdom of Saudi Arabia (table 5). *A*, Map of the Arabian Peninsula region. *B*, Zoomed-in map of the region around station MWLHS. *C*, Plot of Ps single-phase *H-k* stack (with $w_1/w_2/w_3$ stacking weights of 1.0/0.0/0.0). *D*, Plot of 3p1s single-phase *H-k* stack (0.0/1.0/0.0). *E*, Plot of 2p2s single-phase *H-k* stack (0.0/0.0/1.0). *F*, Plot of optimized *H-k* stack (0.5/0.5/0.0) indicating a crustal thickness (*H*) of 29.8±0.3 kilometers (km) and V_P/V_S ratio (*k*) of 1.71±0.02. V_P is P-wave velocity and V_S is S-wave velocity; %, percent.

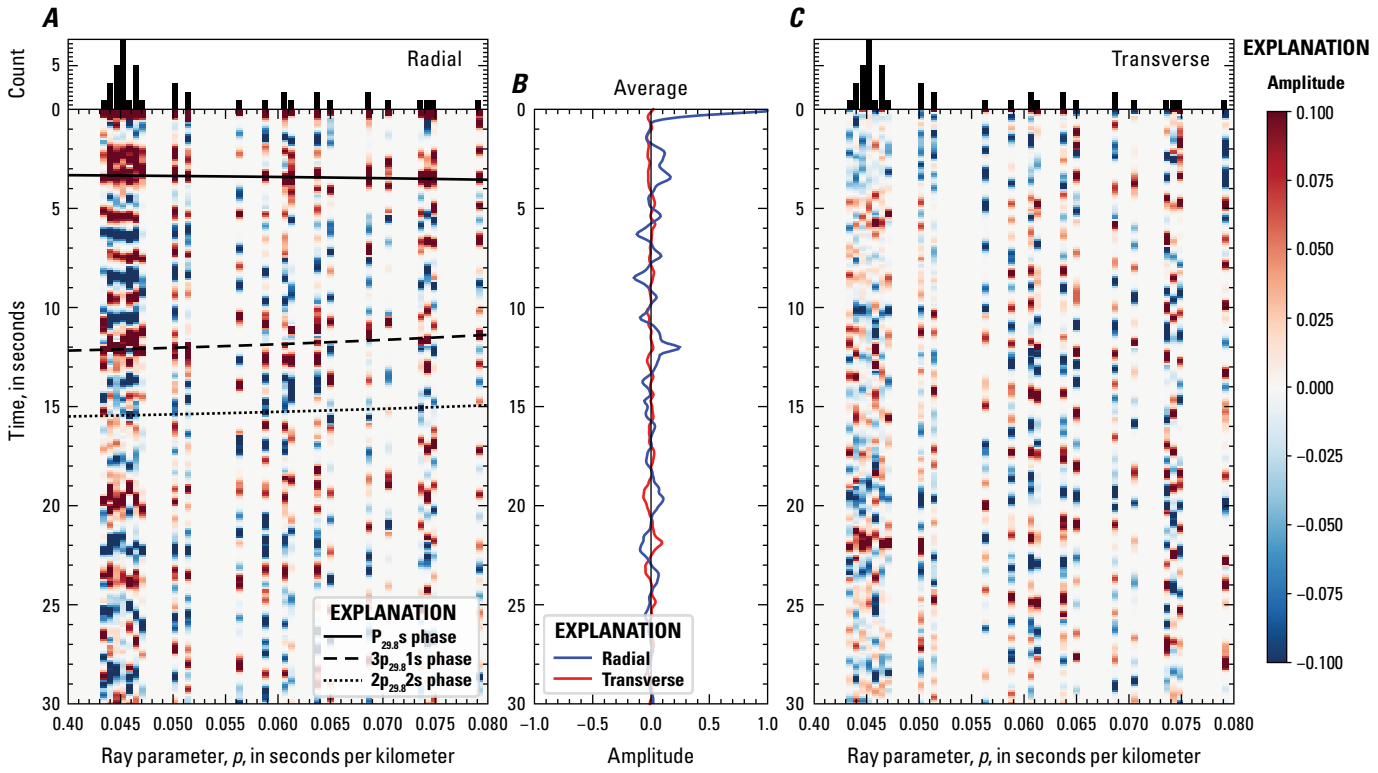

Figure 6. Plots of P-wave receiver function (PRF) gathers for coastal seismic station MWLHS in the Kingdom of Saudi Arabia (fig. 5; table 5). *A*, Radial component of PRFs versus ray parameter (*p*). Individual PRFs are normalized to the maximum amplitude within the time window shown, binned, and normalized by the number of traces per bin (count). *B*, Average of all individual normalized radial and transverse components of PRFs. Transverse components additionally multiplied by 0.3. *C*, Transverse component of PRFs versus ray parameter, normalized as in part *A* and multiplied by 0.3 as in part *B*. Multiplication by 0.3 is an arbitrary scaling to make the normalized energy on the radial plot (part *A*) and transverse plot (part *C*) easier to compare. Note that all panels share the same time axis.

Phase-Weighted *H-k* Stacking

At five stations (QNF01, QNF02, AMGES, FRSS, and DESA; tables 5, 6) for which neither the standard *H-k* stacking nor the resonance-removal filter proved useful, we successfully applied phase-weighted stacking (PWS) (Crotwell, 2007; Ogden and others, 2019) to remove incoherent noise from the signal. In this method, the coherency between the converted (Ps) and multiple (3p1s, 2p2s) arrivals is used to modulate the stacking amplitude $s(H, k)$:

$$s(H,k) = \frac{1}{3N}\left|\sum_{n=1}^{N}\left[e^{i\phi_n(t_{Ps})} + e^{i\phi_n(t_{3p1s})} - e^{i\phi_n(t_{2p2s})}\right]\right|^{v}$$

$$\sum_{n=1}^{N}\left[w_1 r_n(t_{Ps}) + w_2 r_n(t_{3p1s}) - w_3 r_n(t_{2p2s})\right] \qquad (7)$$

where φ_n are the instantaneous phases of the PRF (derived from the Hilbert transform of the PRF) at the predicted Ps, 3p1s, and 2p2s arrival times for the appropriate H and k values, and v is an arbitrary exponent. Using $v = 0$ corresponds to regular *H-k* stacking, with $v = 1$ (Crotwell, 2007, and this study) and $v = 2$ (Ogden and others, 2019) representing progressively more aggressive PWS.

PWS uses the relative coherence of the arrivals to determine their contribution to the *H-k* stack. If the instantaneous phase φ of the PRFs at the three predicted arrival times is equal (as expected for noise-free signals), the weighted sum of the PRFs at these three times is given full weight in the *H-k* stack, whereas if φ at the three arrival times is contradictory (as one would expect from random noise), the weighted sum of the PRFs is given much lower, or zero, weight. In the application of PWS, we did not try to select optimum weights, w, for Ps, 3p1s, and 2p2s, but rather assigned each phase a value of ⅓. We attempted PWS *H-k* stacking only for stations for which we could not otherwise obtain reliable results. We obtained reliable results from an additional five stations. The remaining 20 stations (table 1) defied our efforts to obtain a reliable crustal thickness, either because they have very low signal-to-noise ratios and (or) there are very few PRFs at these stations.

Sedimentary Corrections to Crustal Thickness

The single-layer interpretations of the *H-k* stacks (whether conventional or using PWS) assume a constant wavespeed for the entire crust. However, the traveltime of the Ps phase per kilometer of sedimentary rock (in a low-V_p, high-k basin) is larger than in the high-V_p, low-k crystalline crust. Hence, the presence of appreciable low-velocity sedimentary cover makes crustal thicknesses directly measured from *H-k* stacking (H_{raw}) too large by an amount that increases in proportion to the thickness of sedimentary rocks. For a sedimentary layer thickness, h_s, above a crystalline crust thickness, h_b (such that true crustal thickness $H_{corrected} = h_s + h_b$), the traveltime of the converted Ps phase with respect to a direct P phase is given by:

$$t_{Ps} = h_b\left(\sqrt{\frac{k_b^2}{V_{Pb}^2} - p^2} - \sqrt{\frac{1}{V_{Pb}^2} - p^2}\right) + h_s\left(\sqrt{\frac{k_s^2}{V_{Ps}^2} - p^2} - \sqrt{\frac{1}{V_{Ps}^2} - p^2}\right) \quad (8)$$

where subscripts b and s denote crystalline basement and sedimentary values. Therefore, H_{raw} is given by:

$$H_{raw} = \frac{t_{Ps} - h_s\left(\sqrt{\frac{k_s^2}{V_{Ps}^2} - p^2} - \sqrt{\frac{k_b^2}{V_{Pb}^2} - p^2} + \sqrt{\frac{1}{V_{Pb}^2} - p^2} - \sqrt{\frac{1}{V_{Ps}^2} - p^2}\right)}{\sqrt{\frac{k_c^2}{V_{Pc}^2} - p^2} - \sqrt{\frac{1}{V_{Pc}^2} - p^2}} \quad (9)$$

where subscript c denotes the assumed whole crustal values for P-wave velocity and the V_p/V_s ratio used in the *H-k* stacking.

To correct H_{raw} to the true Moho depth H, we use the sedimentary thickness h_s (equivalent to the basement depth) that is well known across the Arabian Platform from extensive hydrocarbon exploration (Konert and others, 2001 [reproduced by Stern and Johnson, 2010]) (fig. 1*B*). We define the difference between the true crustal thickness and the raw thickness as the error: $\varepsilon = H_{final} - H_{raw}$. For PRFs, the ray parameter p ranges from 0.04 to 0.08 s/km, and in figure 7*A* we show the variation of ε with sedimentary thickness h_s (that is, $\frac{\partial \varepsilon}{\partial h_s}$) as a function of sedimentary V_p and V_p/V_s ratios for constant $p = 0.06$ s/km. For a sedimentary layer thickness of h_s, with $V_p = 4.0$ km/s and $k_s = 1.75$ (Brocher, 2005; fig. 7), H_{raw} must be reduced by ~$0.6h_s$. Figure 7*B* shows the variation of ε with slowness p (that is, $\frac{\partial \varepsilon}{\partial p}$) is irrelevant for the range of p used here. In the following sections, we present the full crustal thickness H (Moho depth below the surface), after reduction by $0.6h_s$ using sedimentary thicknesses of Konert and others (2001; reproduced by Stern and Johnson, 2010), and we discuss crystalline

Table 1. Stations for which no meaningful results were obtained.

[Coordinates referenced to the World Geodetic System of 1984]

Station	Latitude (°N)	Longitude (°E)	Station	Latitude (°N)	Longitude (°E)
QREAT	31.50	37.57	SMAN	26.18	48.07
TREF	31.26	39.36	HIL02	26.06	40.90
HQLS	29.30	35.06	RMAH	25.35	46.88
SRFHA	29.03	44.61	NHRD	24.72	49.02
QLBS	28.65	37.59	RHT17	23.68	39.90
RSHS	28.30	34.80	KAUST	22.33	39.12
URD11	27.94	37.46	BAHS2	20.87	41.19
URD06	27.45	36.76	QNFDS	19.80	40.94
URD05	27.23	36.96	MKHL	17.37	42.68
MQLS	26.63	47.45	JAZS2	16.76	43.05

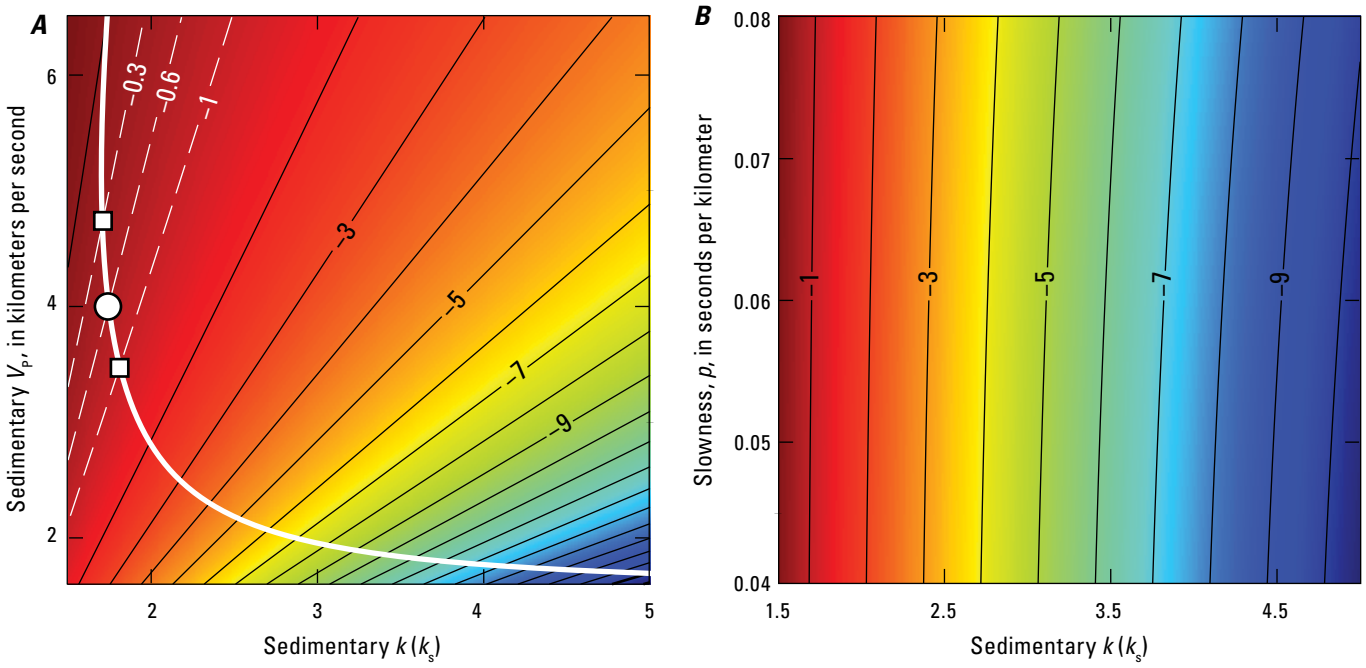

Figure 7. Plots of sedimentary correction factor $\left(\frac{\partial e}{\partial h_s}\right)$ for varying sedimentary P-wave velocities (V_P), P-wave receiver function ray parameter (p; also called slowness), and V_P/V_S ratios (k_s). *A*, Sedimentary correction factor variation with V_P and k for a crystalline crust that has V_P = 6.5 kilometers per second (km/s) and k = 1.73. Solid white line shows an empirical relation between sedimentary V_P and k from Brocher (2005). Dashed white lines show the range of corrections tested. The white circle (preferred correction, 0.6) and white squares (extreme corrections tested, 0.3 and 1.0) mark the intersections of dashed white lines with Brocher's (2005) empirical relations. *B*, Sedimentary correction factor variation with source-earthquake slowness p and sedimentary k_s. ε, error; h_s, sedimentary rock thickness; $k = V_P/V_S$ ratio, where V_P is P-wave velocity and V_S is S-wave velocity.

crustal thickness $h_b = H - h_s$. At stations for which we carried out the resonance-removal and sedimentary-stacking method (Yu and others, 2015), we applied the $0.6h_s$ reduction to the difference between the *H-k* sedimentary thicknesses and the known sedimentary thicknesses. This correction was applied because, in general, the *H-k* sedimentary thicknesses are less than the known sedimentary thicknesses, meaning we are still overestimating the total crustal thickness. There are exactly two stations for which we obtained sedimentary *H-k* values greater than the thicknesses we expected, therefore, at those two stations, the correction is in the opposite direction.

Comparison of *H-k* to Common-Conversion-Point Processing

The importance of the sedimentary correction is shown by comparing *H-k* results before and after correction, overlain on common-conversion-point (CCP) images (fig. 8) along profiles parallel and orthogonal to the Red Sea rift axis (fig. 1*A*). The CCP stacks were calculated on a latitude-longitude grid with 50-km spacing between nodes in each horizontal direction and 2-km spacing vertically. Each CCP node has a 50-km radius, over which rays were stacked—that is, rays parallel to each profile are used by two adjacent CCP nodes; orthogonal rays are used only once. Hence, the alignment of the orthogonal profile toward the greatest earthquake density (fig. 1*C*) is one reason the orthogonal CCP image (fig. 8*B*) is smoother than the parallel CCP image (fig. 8*A*). To create grid-oblique CCP cross sections, we chose only grid nodes within 25 km of the transect. Points along the transects that had more than one node within the 25-km limit are composed of the average of the nodes. On the profile parallel to the Red Sea rift axis, the *H-k* stacking and CCP stacking results are generally in good agreement, including in places where there are large abrupt shifts in imaged Moho depth, for example near lat 24° N., where the station layout along the linear profile switches from stations only on the Arabian Shield (Moho at ~40 km depth) to a station only on the coastal plain (Moho at ~20 km depth) and back on the shield again (fig. 8*A*). Minor discrepancies likely result from assuming the same 1D velocity model across all stations for CCP stacking, whereas *H-k* stacking solves for a unique layer over a half-space velocity model at each station. An additional source of discrepancy comes from CCP stacking using

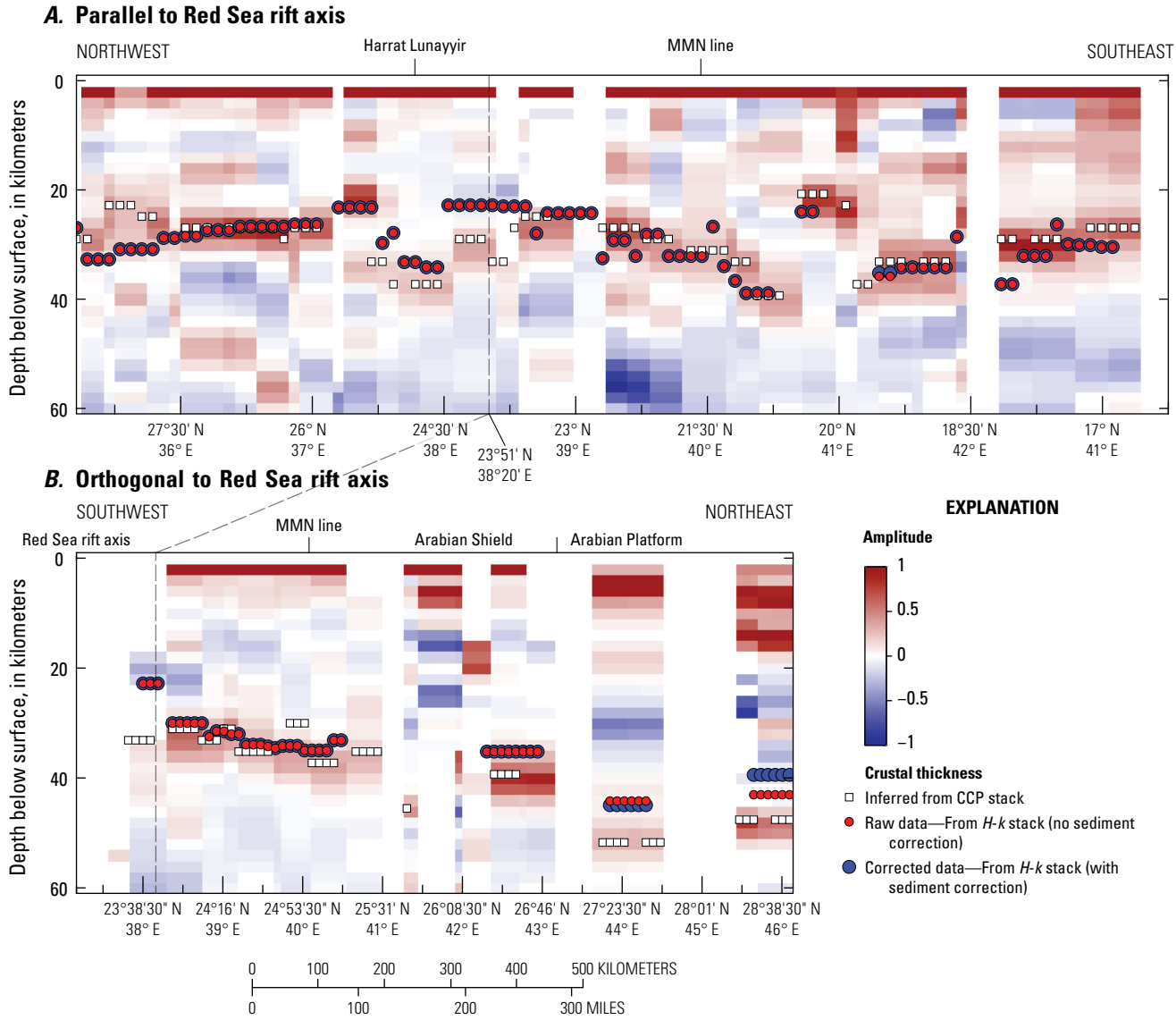

Figure 8. Common-conversion-point (CCP) cross sections in the Kingdom of Saudi Arabia (see fig. 1*A* for locations). The CCP section locations are chosen to maximize station density rather than to be truly parallel or orthogonal to the straight-line approximation of the Red Sea rift axis (fig. 1*A*). *A*, CCP stack parallel to the Red Sea rift axis. *B*, CCP stack orthogonal to the Red Sea rift axis. Crustal thickness is shown for CCP stacks, raw *H-k* stacks, and corrected *H-K* stacks (preferred). Dashed gray line marks the intersection of the two transects. Because different stations are projected onto the two profiles, different images and *H-k* depths appear at the intersection. Amplitude color scale is calculated similarly to receiver function gathers, but CCP conversion amplitudes are higher than *H-k* averages because velocity corrections are applied for different ray parameters and because multiple stations are summed. MMN line, Makkah-Madīnah-Nafud volcanic line.

multiple stations at some nodes, whereas *H-k* stacking purely considers a single station. Large differences (for example, near lat 27.5° N.) appear to be caused by the inability of CCP stacking to handle multiple candidate Ps peaks, whereas *H-k* stacking enforces consistency between the Ps, 3p1s, and 2p2s phases. The profile orthogonal to the Red Sea shows a consistent sense of offset, with the Moho depth estimated by the *H-k* method being shallower than that by CCP stacking by as much as 8 km where the sedimentary section is thickest along the profile, as expected from the analysis as described above. Despite the apparently well-resolved Moho on the CCP image, care must be taken during interpretation of such an image because of the additional traveltime delay caused by the sediments.

Results

We next show *H-k* analyses corroborated by direct inspection of PRFs, including examples from and compiling crustal-thickness results for each of the geologic regions in this study: harrats, coastal plain, Arabian Shield, and Arabian Platform (fig. 1*A*).

Harrat Lunayyir

Harrat Lunayyir (figs. 1*A*, 9*A*) has the greatest station density of the SGS network, with 18 seismometers within an approximately 50-by-50 km area (Blanchette and others, 2018), which were installed during and after the 2009 dike intrusion. This dike intrusion was accompanied by more than 30,000 earthquakes, some as strong as M_w 5.7 (Pallister and others, 2010). One station (LNY07; table 5) in this sub-network is less than 250 km from the Red Sea rift axis and has elevation less than 400 meters (m) above sea level; it is classified as a coastal station in this study.

Station LNY02 (fig. 9; table 2) is a representative seismic station near the center of Harrat Lunayyir (fig. 9). The PRFs at station LNY02 (fig. 10*A*) show a coherent arrival that we identify as the Ps phase, with a positive amplitude (red), arriving 4–5 s after the initial P-wave arrival. Assuming a simplified 1D velocity model (V_P = 6.5 km/s, k = 1.80), with zero sediment thickness (h_s = 0) and a Moho depth of 34 km, we can reasonably match the traveltimes of this arrival as $P_{34}s$ (Moho conversion from 34 km depth), and the later positive arrival at a delay time of ~14 s as $P_{34}pP_{34}s$, that is, the 3p1s Moho multiple. In practice, we examined the *H*-*k* stacks (fig. 9*C*–*E*) and corroborated with the PRF displays (fig. 10*A*) before selecting the final choice of weights (fig. 9*F*). At station LNY02, the Ps phase alone (fig. 9*C*) provides a well-defined zone in *H*-*k* space of possible solutions, but it is insensitive to the actual solution along this trade-off curve. Similarly, the PpPs phase (fig. 9*D*) provides a different but well-defined zone of possible solutions in *H*-*k* space that is also insensitive to *H* and, particularly, *k*. Although the 2p2s multiples can be used to form an *H*-*k* stack (fig. 9*E*), this does not conform to the other two phases, and corresponds to a diffuse region of negative and low-amplitude energy on the PRF (fig. 10*A*). We chose stacking weights of 0.5/0.5/0.0 at this station and obtained *H* and *k* values of 34.0±0.6 km and 1.80±0.03 (fig. 9*F*). These values match those of Tang and others (2016), who reported *H* = 34.1±0.4 km and *k* = 1.80±0.02 (2σ uncertainties). Results from equivalent analyses of all Harrat Lunayyir stations are given in table 2, with an average Moho depth of 33.7 km and crustal *k* of 1.78.

In a 1D and isotropic Earth model, we expect the transverse component of the PRF to be composed purely of noise (Savage, 1998; Schulte-Pelkum and Mahan, 2014), so coherent transverse energy (fig. 10*B, C*) likely represents an obliquely dipping boundary beneath the station. It is possible that such a dipping structure and corresponding lateral velocity heterogeneity has defocused the 2p2s multiple (fig. 10*A*). Such considerations suggest a heuristic uncertainty of at least ±1 km in Moho depth and ±0.05 in V_P/V_S ratios.

Table 2. *H-k* stacking results for Harrat Lunayyir stations in the Kingdom of Saudi Arabia.

[Coordinates referenced to the World Geodetic System of 1984. w_i are the stacking weights for each phase. *H*, depth to Mohorovičić discontinuity (Moho) in kilometers (km); $k = V_P/V_S$ where V_P is P-wave velocity and V_S is S-wave velocity; $2\sigma_H$ and $2\sigma_k$, uncertainty at the two standard deviation level for *H* and *k*, respectively]

Station	Latitude (°N)	Longitude (°E)	w_1	w_2	w_3	*H* (km)	$2\sigma_H$	*k*	$2\sigma_k$
LNY01	25.22	37.96	0.4	0.3	0.3	32.6	0.6	1.85	0.04
LNY02	25.14	37.86	0.5	0.5	0.0	34.0	0.6	1.80	0.03
LNY03	25.38	37.85	0.5	0.5	0.0	36.0	0.6	1.68	0.03
LNY04	25.27	37.65	0.4	0.3	0.3	32.4	0.7	1.86	0.04
LNY05	25.05	37.70	0.4	0.3	0.3	37.4	0.7	1.61	0.03
LNY06[1]	25.21	37.78	0.5	0.5	0.0	34.4	0.5	1.81	0.03
LNY08	25.03	37.85	0.5	0.5	0.0	35.0	0.6	1.78	0.03
LNY09	25.40	37.66	0.4	0.3	0.3	37.0	0.5	1.64	0.02
LNY10	25.27	37.86	0.4	0.3	0.3	33.0	0.5	1.84	0.03
LNY11	25.32	37.77	0.4	0.3	0.3	31.8	0.4	1.97	0.03
LNY12	25.27	37.77	0.5	0.5	0.0	32.8	0.9	1.75	0.05
LNY13	25.17	37.63	0.4	0.3	0.3	31.2	0.5	1.85	0.03
LNY14	25.25	37.77	0.4	0.3	0.3	33.0	0.7	1.82	0.04
LNY15	25.26	37.80	0.4	0.3	0.3	33.0	0.6	1.80	0.03
LNY16	25.35	37.60	0.4	0.3	0.3	32.6	0.8	1.75	0.04
LNY17	25.24	37.80	0.5	0.5	0.0	33.8	0.7	1.79	0.04
LNYS	25.08	37.94	0.5	0.5	0.0	35.2	0.7	1.76	0.04
MURBA	25.41	38.25	0.5	0.5	0.0	31.6	0.5	1.73	0.03
TRAS	25.06	38.57	0.4	0.3	0.3	35.0	0.7	1.62	0.03

[1]See text for discussion of multiple peaks.

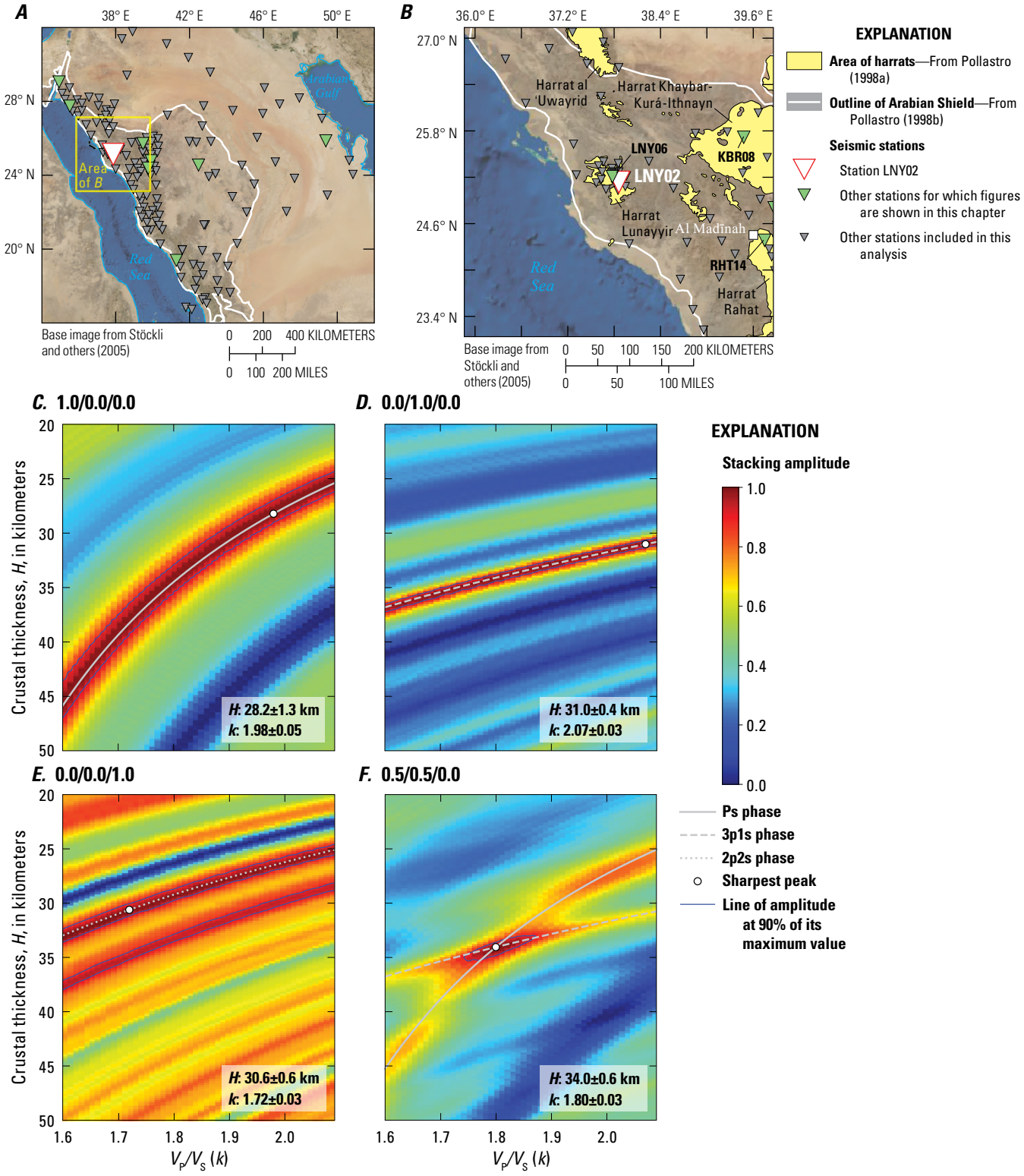

Figure 9. Location maps and plots of the receiver function analysis for seismic station LNY02 in Harrat Lunayyir in the Kingdom of Saudi Arabia (table 2). *A*, Map of the Arabian Peninsula region. *B*, Zoomed-in map of the region around station LNY02. *C*, Plot of Ps single-phase *H-k* stack (with $w_1/w_2/w_3$ stacking weights of 1.0/0.0/0.0). *D*, Plot of 3p1s single-phase *H-k* stack (0.0/1.0/0.0). *E*, Plot of 2p2s single-phase *H-k* stack (0.0/0.0/1.0). *F*, Plot of optimized *H-k* stack (0.5/0.5/0.0) indicating a crustal thickness (*H*) of 34.0±0.6 kilometers (km) and V_P/V_S ratio (*k*) of 1.80±0.03. V_P is P-wave velocity and V_S is S-wave velocity; %, percent.

The coherent arrival between the Ps and 3p1s phases (6–7 s; fig. 10*A*) cannot be explained as a conversion or a multiple from the Moho; nor is it a sidelobe of the Moho $P_{34}s$ phase, behind which it is delayed by ≥2 s, which is more than the central period (*T*) of the data (*T*/2 <1.5 s). The negative amplitude of this arrival is, however, consistent with a P-to-S conversion from a deeper, negative velocity discontinuity with wavespeed decreasing downward. We identify this arrival as the Ps conversion at the lithosphere-asthenosphere boundary (LAB) (Blanchette and others, 2018). The incoherence of the expected $2p_{34}2s$ phases is not caused by superposition with the LAB-generated phases (fig. 10*A*). The seismic velocity contrast across the LAB is thought to be of smaller magnitude and spread over a wider vertical transition zone than the contrast across the Moho (Artemieva, 2011). These factors would yield a lower frequency, lower amplitude signal than the Moho conversion. We hypothesize this is the reason we did not observe multiple arrivals from the LAB at this or any other station. Although the LAB arrival is evident on numerous stations, in this study we reserve attention for the Moho.

There is one Harrat Lunayyir station, LNY06 (table 2), for which *H-k* stacking is ambiguous. Station LNY06 is only ~12 km from station LNY02 (fig. 11*A, B*), but has "ringy" data (many coherent phases, possibly multiple reflections from within or at the base of basalt flows) (fig. 12*A*), and shows two distinct peaks in *H-k* space (fig. 11*F*) at depths of 30.4±0.5 km and 34.4±0.5 km. Although we would be unable to pick the correct Moho conversion from this station alone, the other 17 nearby stations across Harrat Lunayyir have 31.2<*H*<37.4 km, so that the most plausible result at station LNY06 for *H* is 34.4±0.5 km, which we report here.

Stations LNY06 and LNY02 both appear to show a converter from the LAB but at respective delay times of ~6.25 s and ~6.5 s, suggesting variable LAB depth (figs. 10, 12).

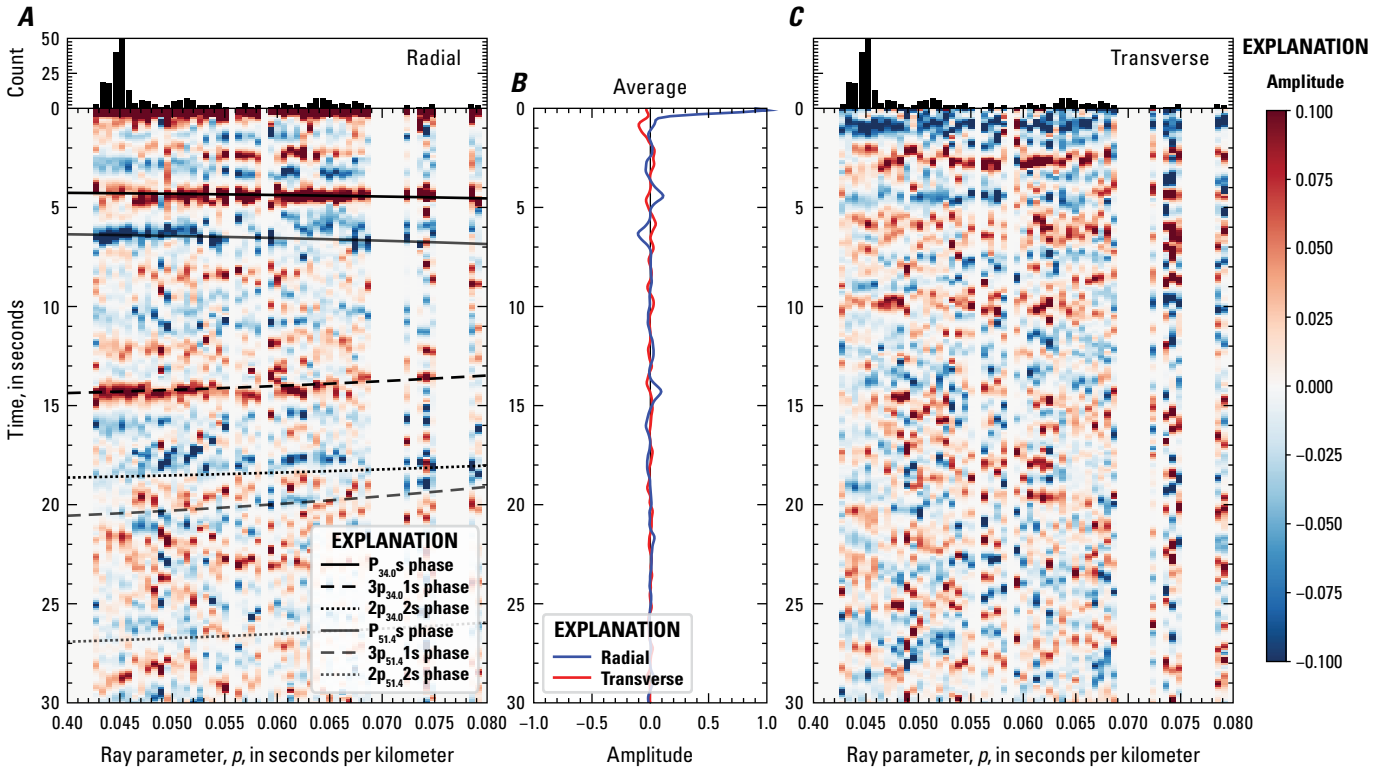

Figure 10. Plots of P-wave receiver function (PRF) gathers for seismic station LNY02 in Harrat Lunayyir in the Kingdom of Saudi Arabia (fig. 9; table 2). *A*, Radial component of PRFs versus ray parameter (*p*). Individual PRFs are normalized to the maximum amplitude within the time window shown, binned, and normalized by the number of traces per bin (count). Gray lines are theoretical moveout curves for phases generated through a mantle lid with V_P = 8.04 kilometers per second (km/s) and *k* = 1.94 that extends from 34.0 to 51.4 km. *B*, Average of all individual normalized radial and transverse components of PRFs. Transverse components additionally multiplied by 0.3. *C*, Transverse component of PRFs versus ray parameter, normalized as in part *A* and multiplied by 0.3 as in part *B*. Multiplication by 0.3 is an arbitrary scaling to make the normalized energy on the radial plot (part *A*) and transverse plot (part *C*) easier to compare. Note that all panels share the same time axis. V_P is P-wave velocity and V_S is S-wave velocity.

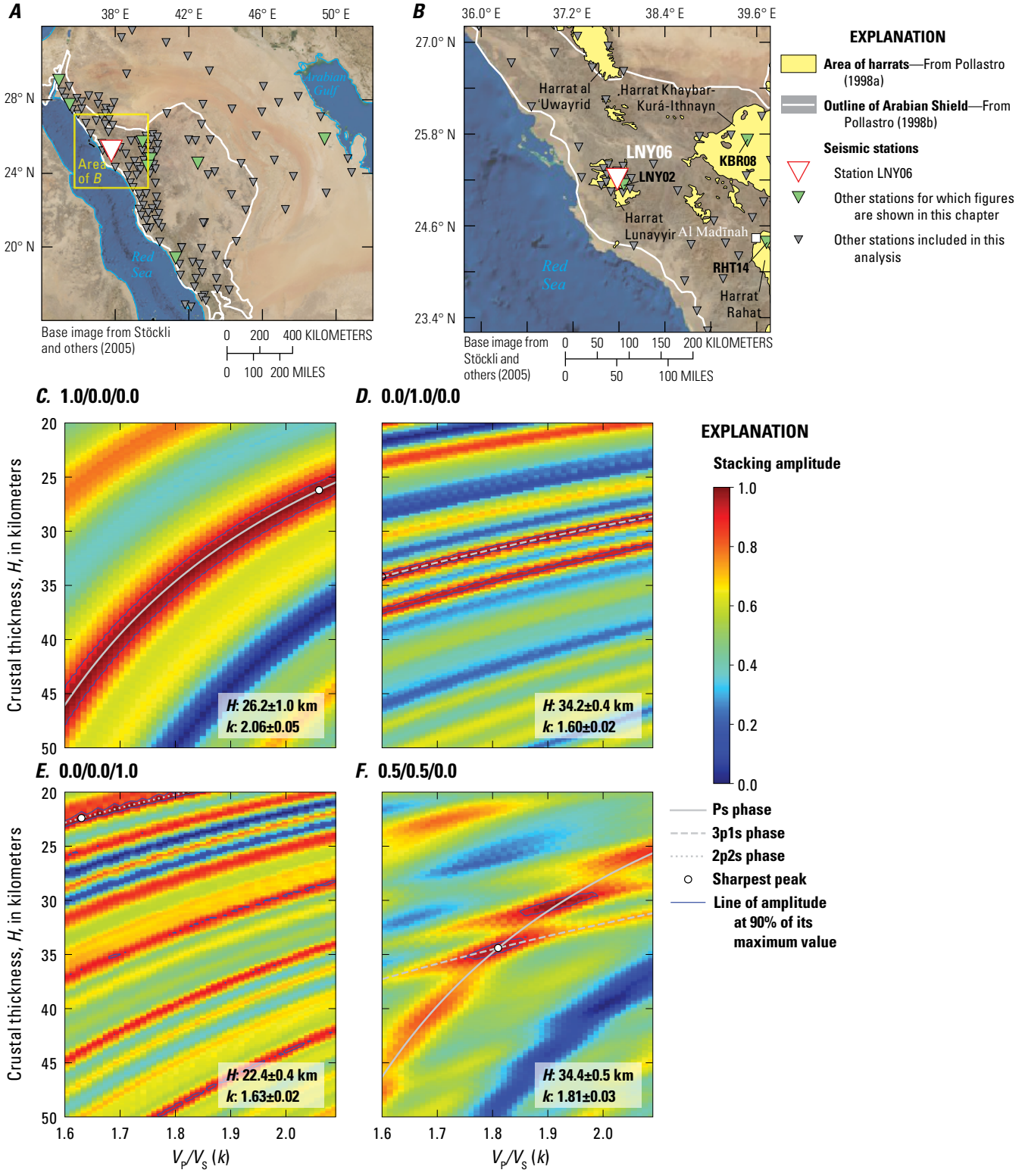

Figure 11. Location maps and plots of the receiver function analysis for seismic station LNY06 in Harrat Lunayyir in the Kingdom of Saudi Arabia (table 2). *A*, Map of the Arabian Peninsula region. *B*, Zoomed-in map of the region around station LNY06. *C*, Plot of Ps single-phase *H-k* stack (with $w_1/w_2/w_3$ stacking weights of 1.0/0.0/0.0). *D*, Plot of 3p1s single-phase *H-k* stack (0.0/1.0/0.0). *E*, Plot of 2p2s single-phase *H-k* stack (0.0/0.0/1.0). *F*, Plot of optimized *H-k* stack (0.5/0.5/0.0) indicating a crustal thickness (*H*) of 34.4±0.5 kilometers (km) and V_P/V_S ratio (*k*) of 1.81±0.03. V_P is P-wave velocity and V_S is S-wave velocity; %, percent.

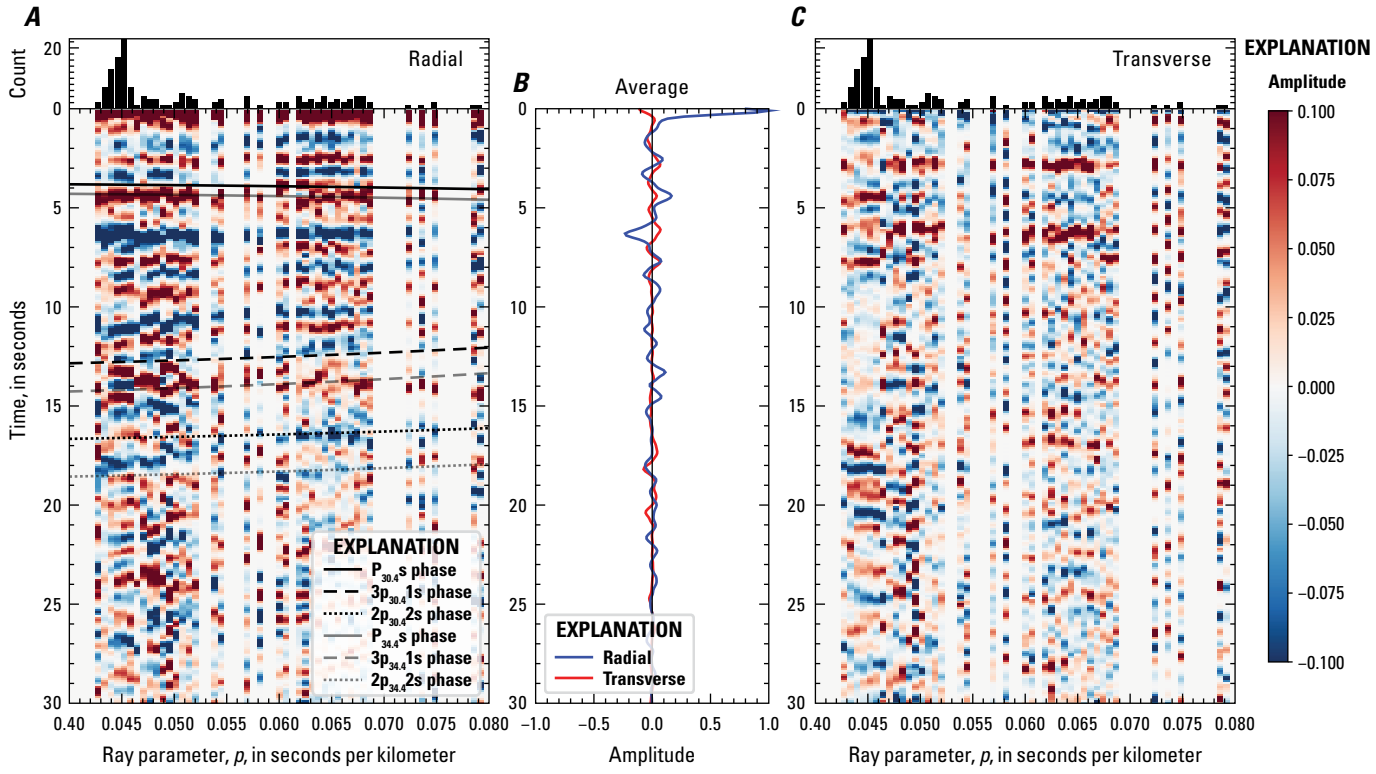

Figure 12. Plots of P-wave receiver function (PRF) gathers for Arabian Shield seismic station LNY06 in Harrat Lunayyir in the Kingdom of Saudi Arabia (fig. 11; table 2). *A*, Radial component of PRFs versus ray parameter (*p*). Individual PRFs are normalized to the maximum amplitude within the time window shown, binned, and normalized by the number of traces per bin (count). *B*, Average of all individual normalized radial and transverse components of PRFs. Transverse components additionally multiplied by 0.3. *C*, Transverse component of PRFs versus ray parameter, normalized as in part *A* and multiplied by 0.3 as in part *B*. Multiplication by 0.3 is an arbitrary scaling to make the normalized energy on the radial plot (part *A*) and transverse plot (part *C*) easier to compare. Note that all panels share the same time axis.

Harrat Khaybar

The composite Harrat Khaybar-Kurá-Ithnayn is the northernmost concentration of alkalic volcanic centers along the MMN line (Camp and others, 1991; Roobol and Camp, 1991; Camp and Roobol, 1992) (fig. 1) that was emplaced since ~12 Ma during the second stage of Red Sea rifting (Blanchette and others, 2018). Whereas prior to 2012 there was only one seismometer on the western edge of Harrat Khaybar (station KBRS; table 3), there is now an array of 11 stations within Harrat Khaybar (fig. 13).

The seismometer KBR08 (table 3), on the western edge of Harrat Khaybar (fig. 13*A*), has PRFs (fig. 14*A*) that share many similarities with the observations discussed for Harrat Lunayyir stations (fig. 12*A*). There is a coherent, positive-amplitude (red) Moho Ps phase at ~4–5 s delay time, followed by a negative-polarity LAB Ps phase at ~7 s (fig. 14*A*). The 3p1s phase is coherent and arrives between ~14 and 15 s. As for station LNY02, there is a hint of a 2p2s phase at ~17–20 s, but the 3-s span and low amplitude suggest lateral wavespeed heterogeneity. Significant Moho dip is ruled out by the consistent phase of Ps at all back azimuths (not shown; see Blanchette and others, 2023) (Schulte-Pelkum and Mahan, 2014).

These observations from station KBR08 receiver functions are consistent with its single-phase *H*-*k* stacks (fig. 13*C*–*E*). The Ps stack (fig. 13*C*) and 3p1s stack (fig. 13*D*) are well resolved, but the 2p2s arrivals (fig. 13*E*) are too diffuse, spanning too broad a range of *H* to provide much sensitivity. We use weights of 0.5/0.5/0.0 to obtain $H = 36.4 \pm 0.5$ km and $k = 1.72 \pm 0.02$, identical within uncertainty to previous results (35.1±0.6 km and 1.74±0.04) for station KBRS, which is just 23 km away (Tang and others, 2016). The analysis for station KBRS results in *H* and *k* values of 38.2±0.5 km and 1.76±0.02, respectively, emphasizing the distinction between formal and heuristic uncertainties. Results for all Harrat Khaybar stations are given in table 3, with an average Moho depth *H* of 35.5 km and crustal *k* of 1.75.

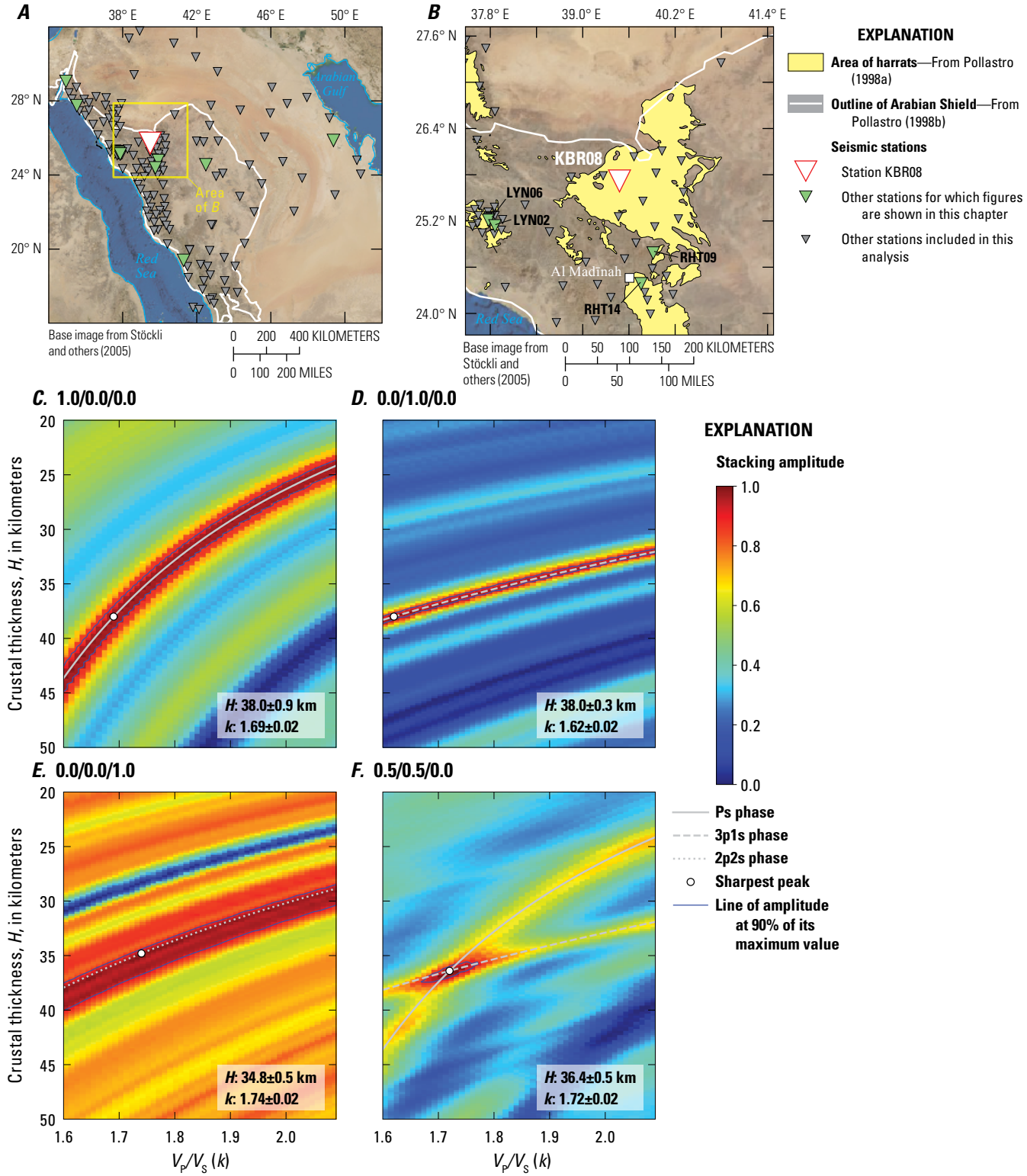

Figure 13. Location maps and plots of the receiver function analysis for seismic station KBR08 in Harrat Khaybar in the Kingdom of Saudi Arabia (table 3). *A*, Map of the Arabian Peninsula region. *B*, Zoomed-in map of the region around station KBR08. *C*, Plot of Ps single-phase *H-k* stack (with $w_1/w_2/w_3$ stacking weights of 1.0/0.0/0.0). *D*, Plot of 3p1s single-phase *H-k* stack (0.0/1.0/0.0). *E*, Plot of 2p2s single-phase *H-k* stack (0.0/0.0/1.0). *F*, Plot of optimized *H-k* stack (0.5/0.5/0.0) indicating a crustal thickness (*H*) of 36.4±0.5 kilometers (km) and V_P/V_S ratio (*k*) of 1.72±0.02. V_P is P-wave velocity and V_S is S-wave velocity; %, percent.

Table 3. *H-k* stacking results for Harrat Khaybar stations in the Kingdom of Saudi Arabia.

[Coordinates referenced to the World Geodetic System of 1984. w_i are the stacking weights for each phase. *H*, depth to Mohorovičić discontinuity (Moho) in kilometers (km) below the surface; $k = V_P/V_S$ where V_P is P-wave velocity and V_S is S-wave velocity; $2\sigma_H$ and $2\sigma_k$, uncertainty at the two standard deviation level for *H* and *k*, respectively]

Station	Latitude (°N)	Longitude (°E)	w_1	w_2	w_3	*H* (km)	$2\sigma_H$	*k*	$2\sigma_k$
KBR01	25.46	39.78	0.4	0.3	0.3	36.2	0.7	1.74	0.04
KBR02	25.23	40.24	0.4	0.3	0.3	35.8	0.5	1.78	0.02
KBR03	25.82	39.95	0.4	0.3	0.3	36.2	0.5	1.76	0.02
KBR04	25.98	40.28	0.5	0.5	0.0	34.0	0.4	1.77	0.02
KBR05	25.57	40.31	0.5	0.5	0.0	34.0	0.5	1.79	0.04
KBR06	26.11	40.03	0.5	0.5	0.0	34.6	0.5	1.76	0.03
KBR07	25.26	39.46	0.5	0.5	0.0	35.0	0.5	1.75	0.02
KBR08	25.72	39.48	0.5	0.5	0.0	36.4	0.5	1.72	0.02
KBR09	26.03	39.67	0.4	0.3	0.3	36.6	0.6	1.70	0.02
KBR10	25.13	39.94	0.5	0.5	0.0	35.0	0.7	1.77	0.02
KBR13	25.77	38.85	0.5	0.5	0.0	34.0	0.5	1.75	0.02
KBRS	25.79	39.26	0.4	0.3	0.3	38.2	0.5	1.76	0.02

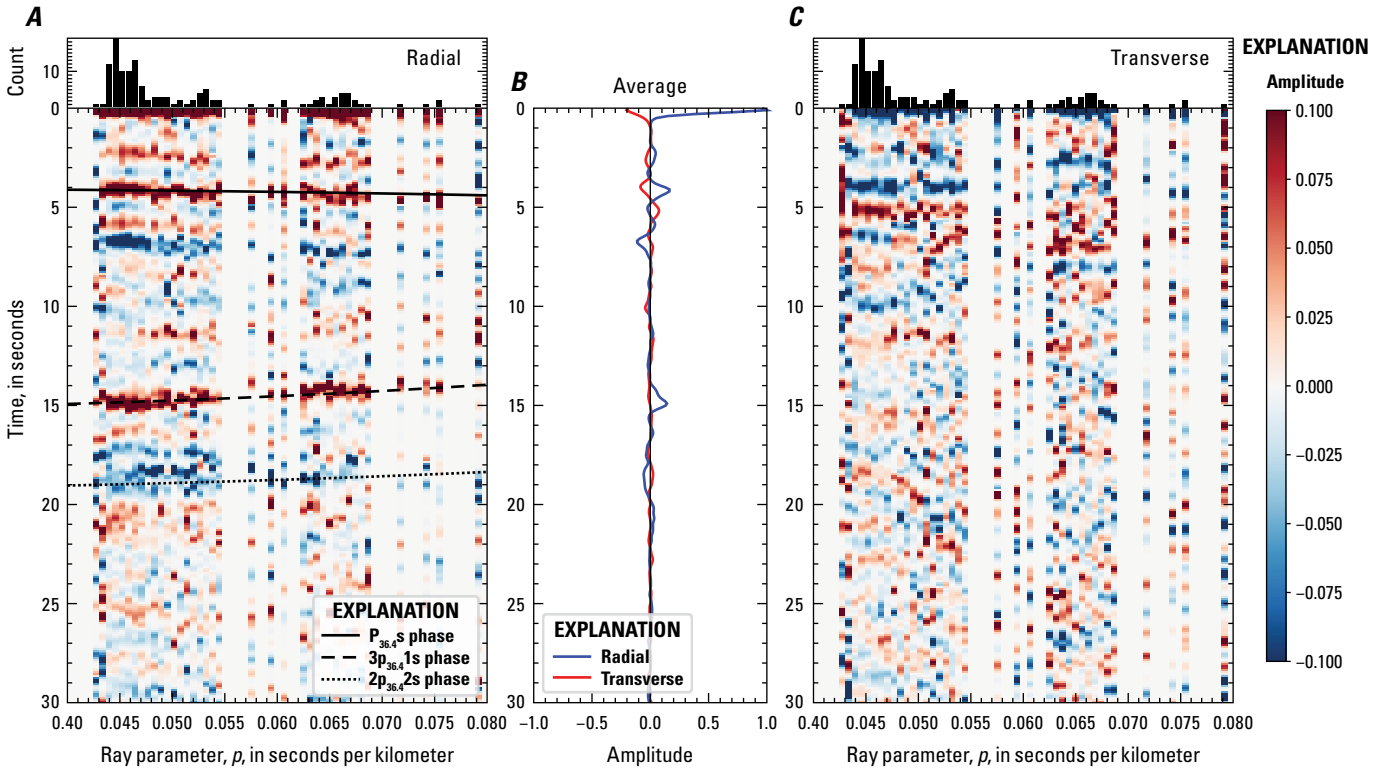

Figure 14. Plots of P-wave receiver function (PRF) gathers for seismic station KBR08 in Harrat Khaybar in the Kingdom of Saudi Arabia (fig. 13; table 3). *A*, Radial component of PRFs versus ray parameter (*p*). Individual PRFs are normalized to the maximum amplitude within the time window shown, binned, and normalized by the number of traces per bin (count). *B*, Average of all individual normalized radial and transverse components of PRFs. Transverse components additionally multiplied by 0.3. *C*, Transverse component of PRFs versus ray parameter, normalized as in part *A* and multiplied by 0.3 as in part *B*. Multiplication by 0.3 is an arbitrary scaling to make the normalized energy on the radial plot (part *A*) and transverse plot (part *C*) easier to compare. Note that all panels share the same time axis.

Harrat Rahat

Northern Harrat Rahat last erupted in 1256 C.E. (Camp and others, 1987) and was the focus of the 2013–2017 cooperative SGS-USGS project to investigate volcano and seismic hazards to the city of Al Madīnah al Munawwarah. There are 14 seismic stations within the densely instrumented northern part of Harrat Rahat (figs. 1, 15*B*). Three stations within this sub-network (RHT05, RHT06, and RHT13) are more than 30 km (~one crustal thickness) from Cenozoic basalt flows (Pollastro, 1998a) and are here classified as on the Arabian Shield (fig. 1; table 6). Station RHT16 and six other stations were installed in the southern part of Harrat Rahat, along the southern extent of the MMN line (table 4; fig. 1*A*), and are here classified as within the harrat.

Station RHT09 is on lava flows north of Al Madīnah that traveled south from Harrat Khaybar or Kurá toward Harrat Rahat (Roobol and Camp, 1991) (fig. 15*A*). The receiver functions at this station (fig. 16*A*) are as clear as those at station KBR08. There is a broad, low-amplitude positive arrival between 0 and 2 s, with a moveout opposite to that expected from a shallow Ps conversion. This phase appears to have slightly smaller differential traveltimes from events originating with a back azimuth of ~70–130°, unlike the Ps phase. The Moho Ps arrival and the 3p1s phase are both narrow and high amplitude. The 2p2s arrivals are strongest at ray parameters (p) ≤0.055 s/km, likely owing to the uneven earthquake source distribution (figs. 1*C*, 16*A*). These phases are consistent with the single-phase stacks (fig. 15*C–E*), and the stacking results are relatively insensitive to the weights chosen (fig. 15*F*). We chose to use 0.4/0.3/0.3 as the optimized stacking weights with resulting H and k of 35.0±0.6 km and 1.75±0.03, respectively, which is essentially identical to those of Tang and others (2016) who obtained H = 35.1±0.4 km and k = 1.74±0.02.

Station RHT14 is located on the youngest lava flows close to Al Madīnah (fig. 17*A*). The P-wave receiver functions for this station are dominated by strong ringing that was not significantly reduced by the resonance filter (fig. 18*A*) but still contain useful information about the crust. A positive arrival of unknown origin follows the direct P-wave by <1 s. The 1256 C.E. lava flow is only 5–10 m thick (Dietterich and others, 2018, 2023), and a gravity survey shows that about 100 m of lavas and possible low-density sediments overlie the

Table 4. *H-k* stacking results for Harrat Rahat stations in the Kingdom of Saudi Arabia.

[Coordinates referenced to the World Geodetic System of 1984. w_i are the stacking weights for each phase. H, depth to Mohorovičić discontinuity (Moho) in kilometers (km) below the surface; $k = V_P/V_S$ where V_P is P-wave velocity and V_S is S-wave velocity; $2\sigma_H$ and $2\sigma_k$, uncertainty at the two standard deviation level for H and k, respectively]

Station	Latitude (°N)	Longitude (°E)	w_1	w_2	w_3	H (km)	$2\sigma_H$	k	$2\sigma_k$
FDAS	21.83	40.36	0.4	0.3	0.3	36.8	0.7	1.68	0.03
GHASH	22.72	40.23	0.5	0.5	0.0	36.0	0.4	1.73	0.02
HAJR	22.90	39.67	0.5	0.5	0.0	36.0	0.5	1.68	0.03
JURS	21.87	39.80	0.4	0.3	0.3	33.0	0.6	1.73	0.03
MDRK2	22.29	40.26	0.5	0.5	0.0	34.8	0.4	1.77	0.02
MDRS	22.09	40.00	0.4	0.3	0.3	36.2	0.4	1.68	0.02
RHT01	24.27	39.81	0.5	0.5	0.0	34.4	0.5	1.86	0.03
RHT02	24.48	40.09	0.4	0.3	0.3	34.8	0.5	1.77	0.03
RHT03	24.25	40.17	0.4	0.3	0.3	35.8	0.8	1.73	0.03
RHT04	23.99	39.88	0.4	0.3	0.3	35.4	0.6	1.77	0.03
RHT07	24.67	39.04	0.4	0.3	0.3	32.4	0.6	1.71	0.02
RHT08	24.71	39.54	0.4	0.3	0.3	34.8	0.5	1.76	0.03
RHT09	24.78	39.91	0.4	0.3	0.3	35.0	0.6	1.75	0.03
RHT10	24.58	39.90	0.4	0.3	0.3	34.6	0.5	1.78	0.02
RHT11	24.92	39.69	0.5	0.5	0.0	35.4	0.5	1.73	0.03
RHT14	24.39	39.76	0.4	0.3	0.3	35.8	1.0	1.76	0.03
RHT15	24.17	39.84	0.4	0.3	0.3	35.4	0.4	1.80	0.02
RHT16	23.47	40.17	0.4	0.3	0.3	36.4	0.4	1.74	0.02

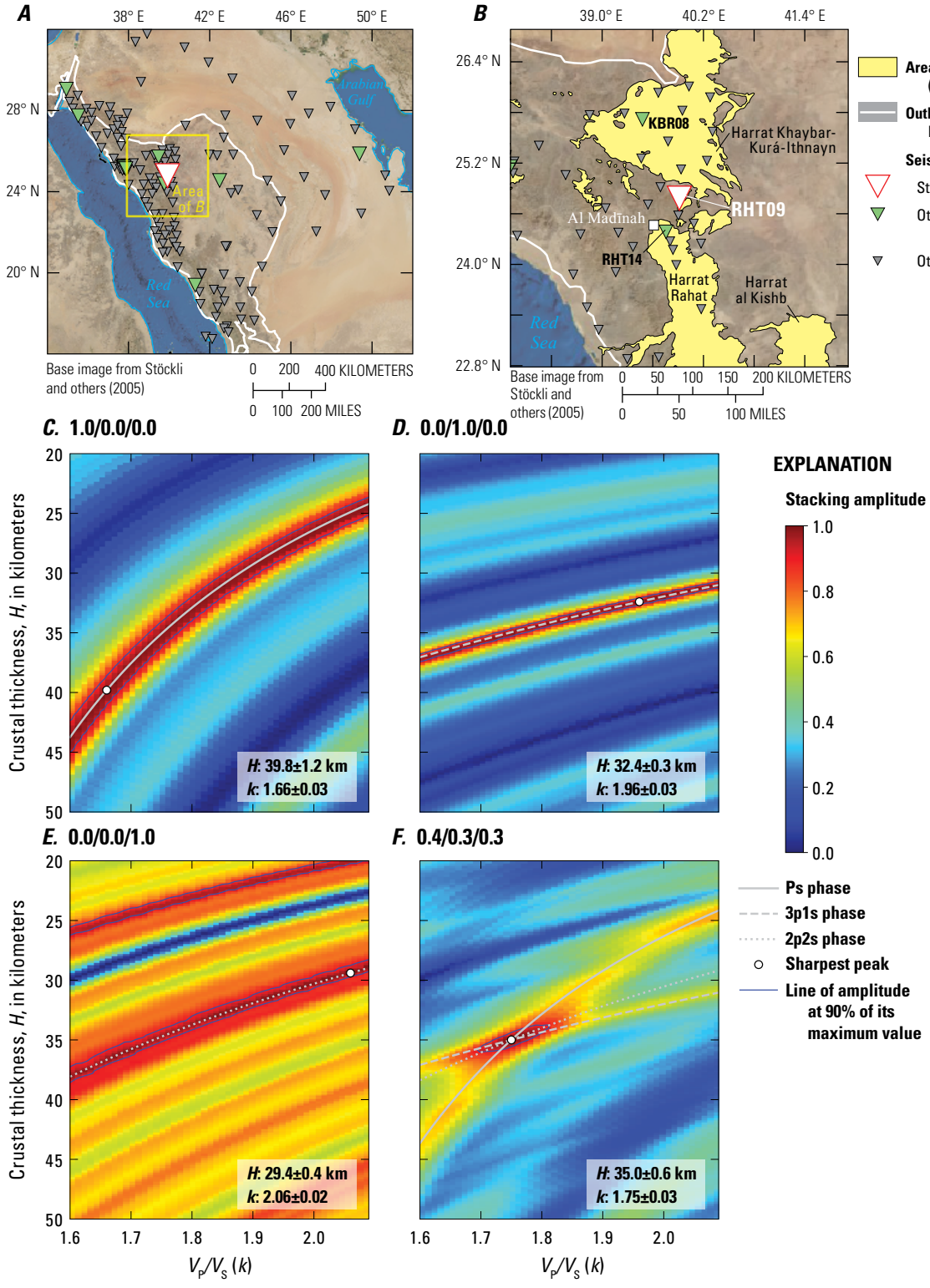

Figure 15. Location maps and plots of the receiver function analysis for seismic station RHT09 between Harrats Rahat and Khaybar in the Kingdom of Saudi Arabia (table 4). *A*, Map of the Arabian Peninsula region. *B*, Zoomed-in map of the region around station RHT09. *C*, Plot of Ps single-phase *H-k* stack (with $w_1/w_2/w_3$ stacking weights of 1.0/0.0/0.0). *D*, Plot of 3p1s single-phase *H-k* stack (0.0/1.0/0.0). *E*, Plot of 2p2s single-phase *H-k* stack (0.0/0.0/1.0). *F*, Plot of optimized *H-k* stack (0.4/0.3/0.3) indicating a crustal thickness (*H*) of 35.0±0.6 kilometers (km) and V_P/V_S ratio (*k*) of 1.75±0.03. V_P is P-wave velocity and V_S is S-wave velocity; %, percent.

Precambrian basement in that area (Langenheim and others, 2019, 2023). Such thickness of seismically slow Cenozoic rocks would produce a signal delayed by only ~0.02 s, which is insufficient to produce this arrival, but adjacent basement exposures are minimally metamorphosed sandstones, siltstones, and shales of the late Proterozoic Furayh Group (Pellaton, 1981) that overlie deeper crystalline rocks of the Arabian Shield (Johnson and others, 2013), possibly accounting for the enigmatic arrival.

Like the direct P-wave, the Moho Ps phase (4–5 s) is also followed by complicated reverberations. There are weak and diffuse 3p1s and 2p2s arrivals that are better identified by their agreement with predicted arrival times than by their absolute amplitudes (fig. 18*A*). These 3p1s and 2p2s arrivals provide ringy images in the single-phase *H-k* stacks (fig. 17*C*, *D*). Although the analytical uncertainty would be lower if we excluded the 2p2s arrivals from the *H-k* analysis, we chose 0.4/0.3/0.3 stacking weights to incorporate the information in the 2p2s phase and obtained *H* and *k* values of 35.8±1.0 km and 1.76±0.03, respectively. The *H-k* stacking results for the rest of the Harrat Rahat stations are listed in table 4. The average Moho depth for Harrat Rahat stations is 35.2 km and crustal *k* is 1.75 (table 8).

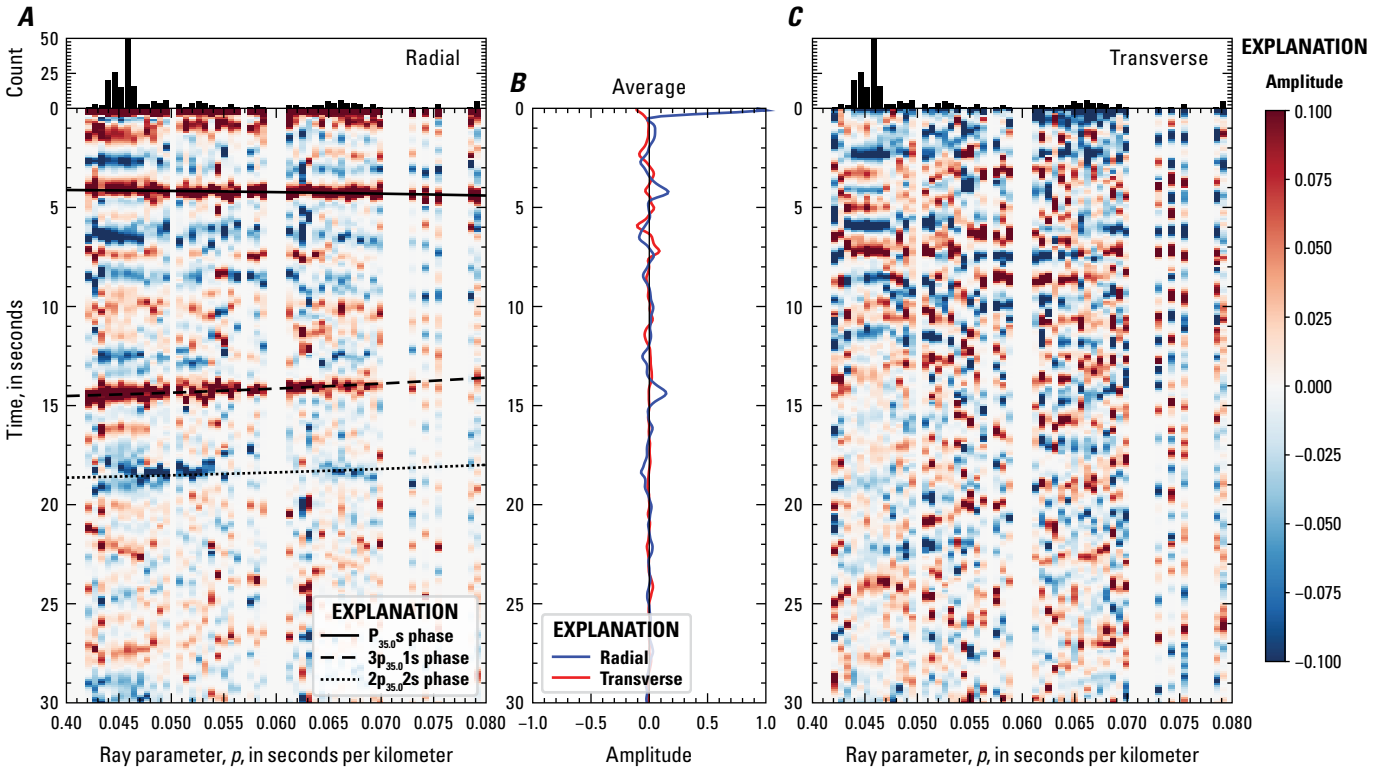

Figure 16. Plots of P-wave receiver function (PRF) gathers for seismic station RHT09 between Harrats Rahat and Khaybar in the Kingdom of Saudi Arabia (fig. 15; table 4). *A*, Radial component of PRFs versus ray parameter (*p*). Individual PRFs are normalized to the maximum amplitude within the time window shown, binned, and normalized by the number of traces per bin (count). *B*, Average of all individual normalized radial and transverse components of PRFs. Transverse components additionally multiplied by 0.3. *C*, Transverse component of PRFs versus ray parameter, normalized as in part *A* and multiplied by 0.3 as in part *B*. Multiplication by 0.3 is an arbitrary scaling to make the normalized energy on the radial plot (part *A*) and transverse plot (part *C*) easier to compare. Note that all panels share the same time axis.

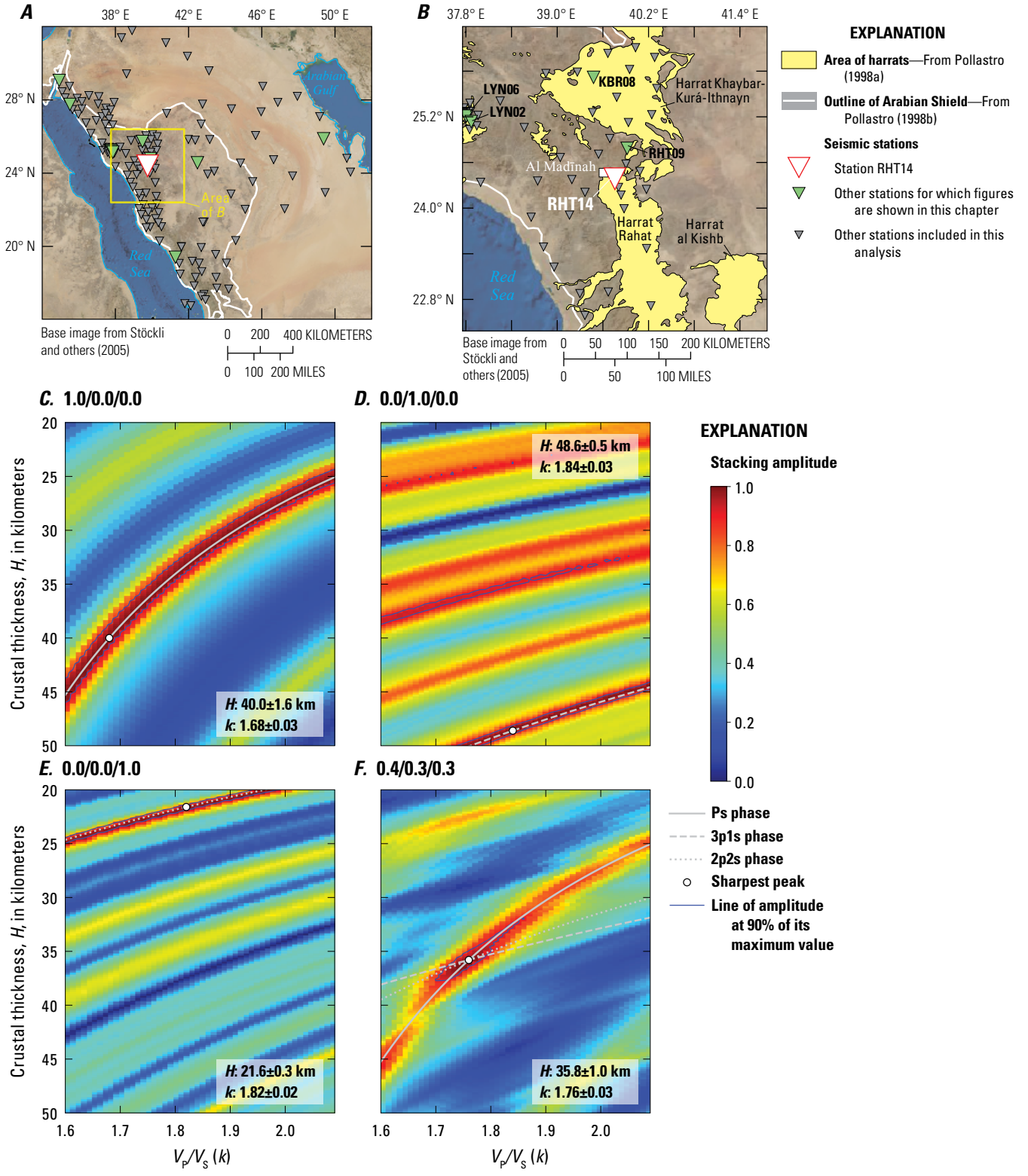

Figure 17. Location maps and plots of the receiver function analysis for seismic station RHT14 in Harrat Rahat in the Kingdom of Saudi Arabia (table 4). *A*, Map of the Arabian Peninsula region. *B*, Zoomed-in map of the region around station RHT14. *C*, Plot of Ps single-phase *H-k* stack (with $w_1/w_2/w_3$ stacking weights of 1.0/0.0/0.0). *D*, Plot of 3p1s single-phase *H-k* stack (0.0/1.0/0.0). *E*, Plot of 2p2s single-phase *H-k* stack (0.0/0.0/1.0). *F*, Plot of optimized *H-k* stack (0.4/0.3/0.3) indicating a crustal thickness (*H*) of 35.8±1.0 kilometers (km) and V_P/V_S ratio (*k*) of 1.76±0.03. V_P is P-wave velocity and V_S is S-wave velocity; %, percent.

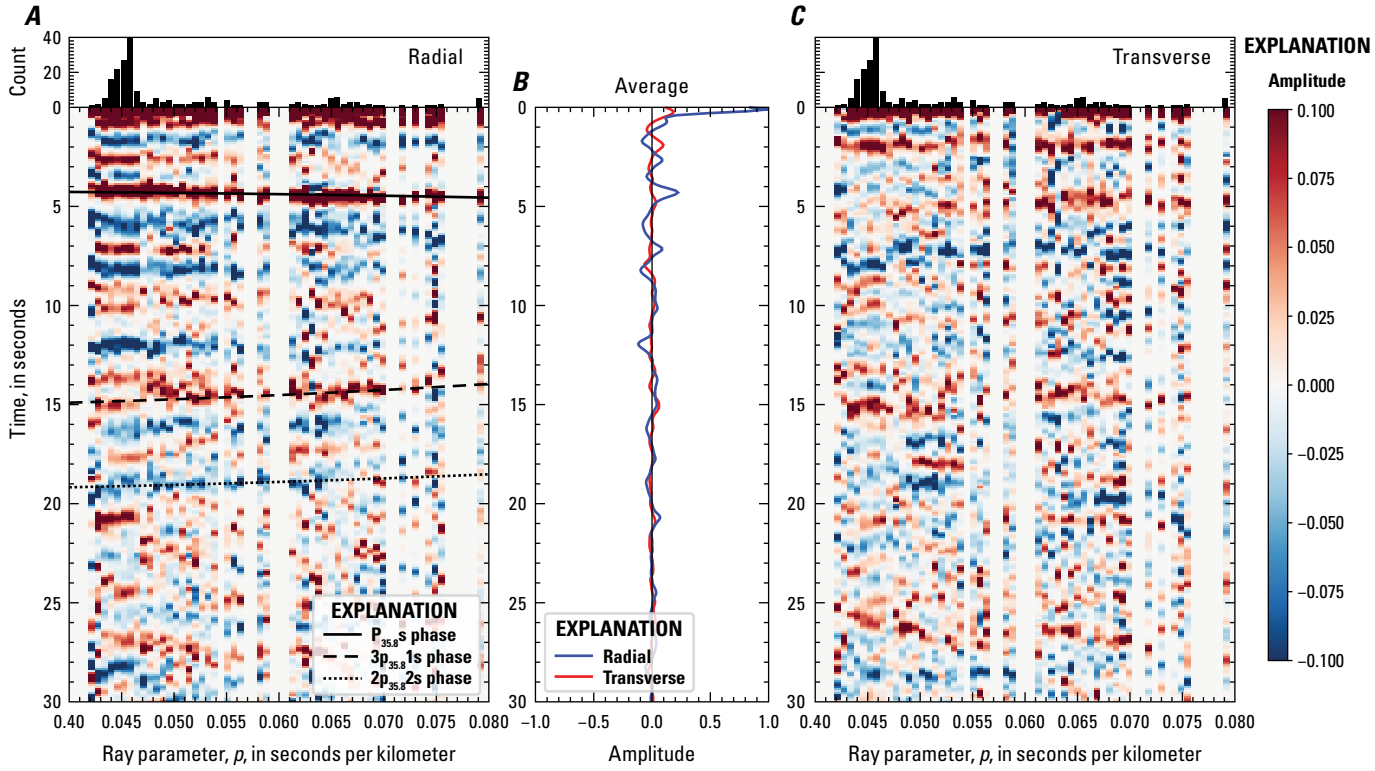

Figure 18. Plots of P-wave receiver function (PRF) gathers for seismic station RHT14 in Harrat Rahat in the Kingdom of Saudi Arabia (fig. 17; table 4). *A*, Radial component of PRFs versus ray parameter (*p*). Individual PRFs are normalized to the maximum amplitude within the time window shown, binned, and normalized by the number of traces per bin (count). *B*, Average of all individual normalized radial and transverse components of PRFs. Transverse components additionally multiplied by 0.3. *C*, Transverse component of PRFs versus ray parameter, normalized as in part *A* and multiplied by 0.3 as in part *B*. Multiplication by 0.3 is an arbitrary scaling to make the normalized energy on the radial plot (part *A*) and transverse plot (part *C*) easier to compare. Note that all panels share the same time axis.

Coastal Plain (Red Sea Rift Margin)

A total of 29 SGS stations are within 250 km of the Red Sea rift axis and at elevations ≤400 m above sea level (fig. 1*A*). The Great Escarpment (dashed white line in fig. 1*B*), a prominent topographic feature defining the Red Sea rift shoulder, is typically ~100 km from the coast and rises above 1,000 m in southern Saudi Arabia but is at lower elevation north of Jiddah. The range front steps west to the north of Yanbu‘ (~24° N.) and becomes topographically complex, with the coastal plain narrowing to 10–50 km from there to the intersection with the Dead Sea Transform at the Gulf of Aqaba (fig. 1*B*). We include these 29 stations as lying within the Red Sea rift, including two stations close to the Gulf of Aqaba and Dead Sea Transform and two stations on Jazā‘ir Farasān (Farasan Islands).

The two northernmost coastal (BDAS) and Arabian Shield (HAQS) stations lie on the Dead Sea Transform, the ~1,000-km-long right-lateral strike-slip fault that stretches from the northern tip of the Red Sea to the East Anatolian Fault. The crust near the Dead Sea Transform has been previously measured to be 32–37 km thick from wide-angle reflection and refraction experiments (El-Isa and others, 1987; DESERT Group, 2004; ten Brink and others, 2006; Mechie and others, 2009) and PRF analyses (Mohsen and others, 2005, 2011). Because of the extensive previous work on this structure, we simply report results from the two SGS seismic stations nearest the Dead Sea Transform at ~15 km (HAQS;

Table 5. *H-k* stacking results for the coastal plain (Red Sea rift margin) area stations in the Kingdom of Saudi Arabia.

[Stations listed from north to south. Coordinates referenced to the World Geodetic System of 1984. w_i are the stacking weights for each phase. *H*, depth to Mohorovičić discontinuity (Moho) in kilometers (km) below the surface (thickness for stations with sedimentary cover); $k = V_P/V_S$ where V_P is P-wave velocity and V_S is S-wave velocity; $2\sigma_H$ and $2\sigma_k$, uncertainty at the two standard deviation level for *H* and *k*, respectively. Corrected thickness = $H-0.6\times h_{s\text{-}SJ2010}$, where $h_{s\text{-}SJ2010}$ is sedimentary thickness from Konert and others (2001; reproduced by Stern and Johnson, 2010) plus elevation above sea level. Where h_s is available from sedimentary *H-k* stacks, corrected thickness = $H+h_s-0.6\times(h_{s\text{-}SJ2010}-h_s)$. —, no value calculated]

Station	Latitude (°N)	Longitude (°E)	w_1	w_2	w_3	*H* (km)	$2\sigma_H$	*k*	$2\sigma_k$	Corrected thickness (km)
BDAS	28.43	35.09	0.5	0.5	0.0	33.6	0.5	1.64	0.03	—
KRABS	28.10	35.26	0.5	0.5	0.0	31.8	0.6	1.60	0.05	—
MWLHS	27.75	35.52	0.5	0.5	0.0	29.8	0.3	1.71	0.02	—
NDEBA	27.47	35.65	0.5	0.5	0.0	29.4	0.7	1.71	0.03	—
DBAS	27.21	35.97	0.5	0.5	0.0	28.4	0.8	1.71	0.03	—
WJHS	26.73	36.39	0.5	0.5	0.0	27.8	0.9	1.72	0.04	—
EWJHS	26.16	36.66	0.4	0.3	0.3	27.4	0.6	1.73	0.03	—
UMJS	25.23	37.31	0.4	0.3	0.3	25.4	0.5	1.63	0.02	—
LNY07	25.13	37.57	0.4	0.3	0.3	32.4	0.5	1.77	0.03	—
YOBS	24.36	38.74	0.4	0.3	0.3	31.0	0.6	1.75	0.03	—
YNBS	24.34	37.99	0.4	0.3	0.3	24.0	0.7	1.94	0.04	—
NSAFS	23.49	38.82	0.4	0.3	0.3	29.0	0.7	1.67	0.03	—
FRJS	22.59	39.36	0.4	0.3	0.3	30.2	1.0	1.66	0.05	—
KHLS2	22.26	39.52	0.4	0.3	0.3	33.0	0.4	1.72	0.02	—
KHLS	22.05	39.30	0.4	0.3	0.3	25.4	0.6	1.86	0.04	—
JEDS	21.72	39.42	0.5	0.5	0.0	27.6	0.6	1.64	0.04	—
SHMS	21.45	39.69	0.4	0.3	0.3	27.8	0.6	1.77	0.03	—
LBNS	21.05	39.90	0.5	0.5	0.0	31.0	0.6	1.78	0.03	—
SHBS	21.00	39.68	0.4	0.3	0.3	27.2	0.5	1.76	0.03	—
LTHS[1]	20.28	40.41	0.4	0.3	0.3	23.6	0.4	1.68	0.05	25.2
			0.05	0.70	0.25	1.55	0.10	1.50	0.40	
QNF01[2]	19.39	41.28	⅓	⅓	⅓	36.6	0.3	1.71	0.01	36.0
QNF02[2]	19.06	41.49	⅓	⅓	⅓	35.0	0.4	1.70	0.01	—
AMGES[2]	18.46	41.54	⅓	⅓	⅓	29.6	0.2	1.94	0.01	—
DRBS	17.83	42.30	0.4	0.4	0.3	33.0	0.6	1.67	0.02	—
BESHS	17.37	42.84	0.4	0.3	0.3	34.4	0.7	1.71	0.02	—
AKWA	17.26	42.70	0.5	0.5	0.0	27.4	0.7	1.69	0.03	—
JAZS	17.07	42.92	0.4	0.3	0.3	31.4	1.2	1.64	0.04	—
FRSS2	16.85	41.79	0.5	0.5	0.0	25.4	0.5	1.97	0.03	25.0
FRSS[2]	16.74	42.11	⅓	⅓	⅓	16.0	0.3	1.77	0.03	15.6

[1]Top row of values are subsedimentary crustal *H-k* stacking results; bottom row of values are sedimentary *H-k* stacking results obtained with the resonance-removal method.

[2]Phase-weighted stacking (PWS) *H-k* stacking results.

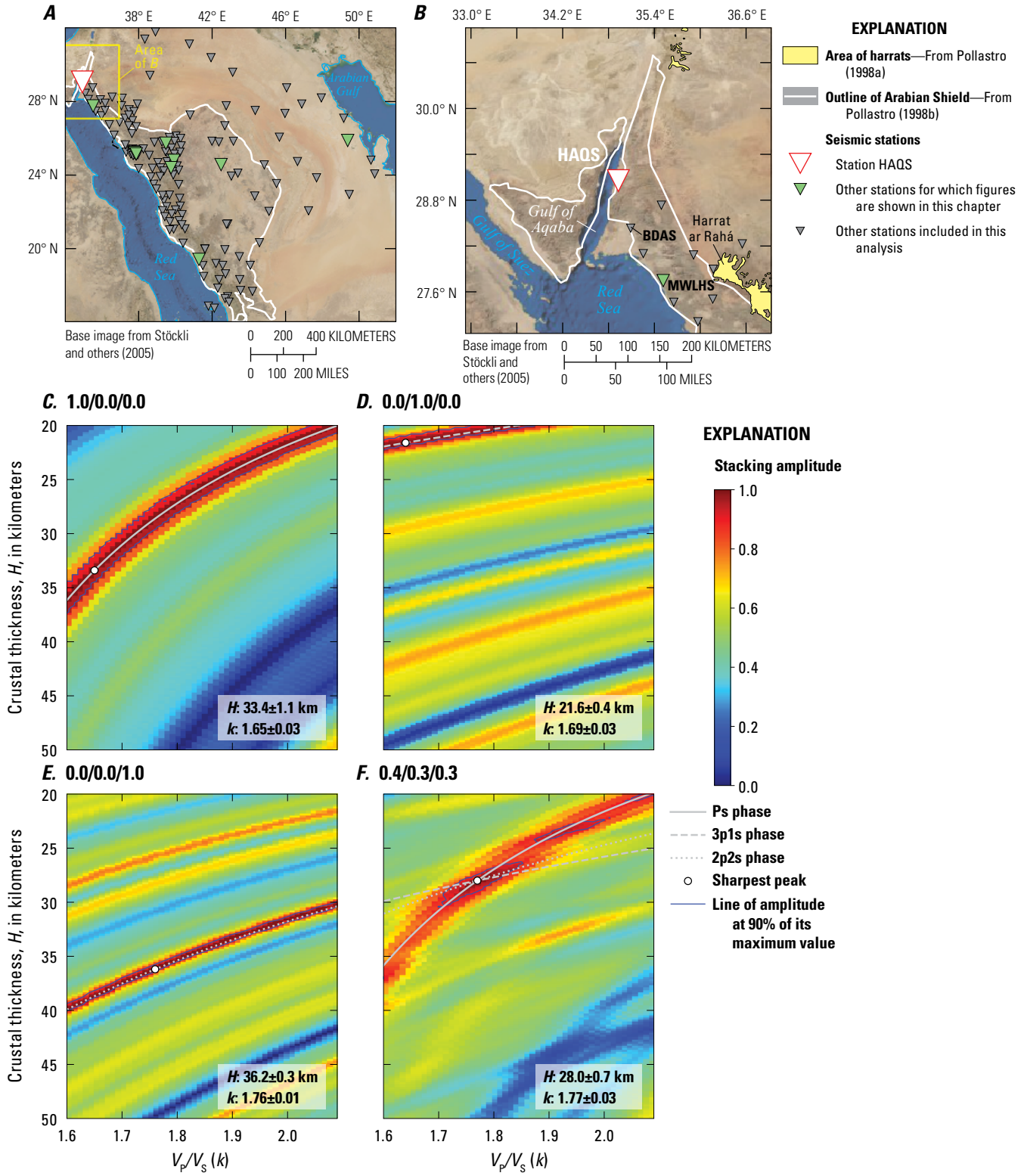

Figure 19. Location maps and plots of the receiver function analysis for Arabian Shield seismic station HAQS in the Kingdom of Saudi Arabia (table 6). *A*, Map of the Arabian Peninsula region. *B*, Zoomed-in map of the region around station HAQS. *C*, Plot of Ps single-phase *H-k* stack (with $w_1/w_2/w_3$ stacking weights of 1.0/0.0/0.0). *D*, Plot of 3p1s single-phase *H-k* stack (0.0/1.0/0.0). *E*, Plot of 2p2s single-phase *H-k* stack (0.0/0.0/1.0). *F*, Plot of optimized *H-k* stack (0.4/0.3/0.3) indicating a crustal thickness (*H*) of 28.0±0.7 kilometers (km) and V_P/V_S ratio (*k*) of 1.77±0.03. V_P is P-wave velocity and V_S is S-wave velocity; %, percent.

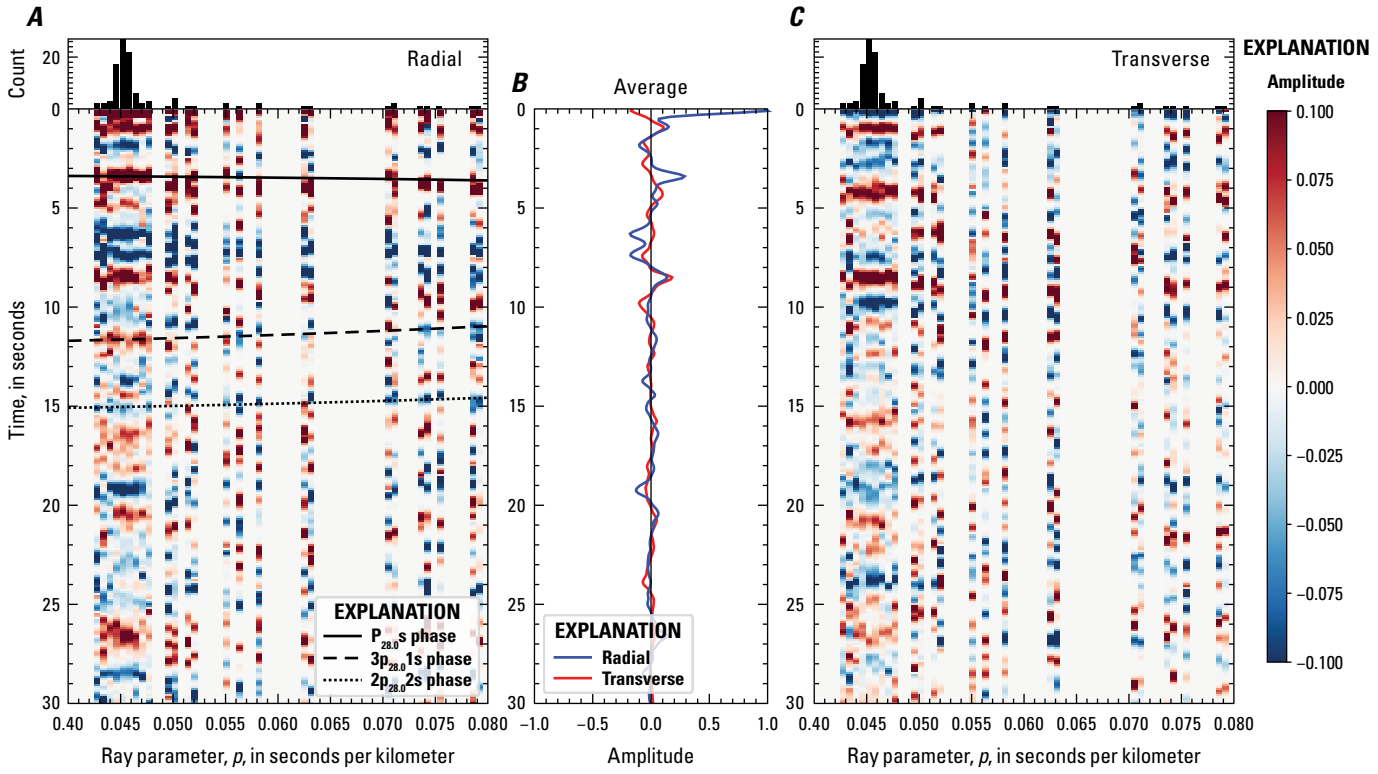

Figure 20. Plots of P-wave receiver function (PRF) gathers for Arabian Shield seismic station HAQS in the Kingdom of Saudi Arabia (fig. 19; table 6). *A*, Radial component of PRFs versus ray parameter (*p*). Individual PRFs are normalized to the maximum amplitude within the time window shown, binned, and normalized by the number of traces per bin (count). *B*, Average of all individual normalized radial and transverse components of PRFs. Transverse components additionally multiplied by 0.3. *C*, Transverse component of PRFs versus ray parameter, normalized as in part *A* and multiplied by 0.3 as in part *B*. Multiplication by 0.3 is an arbitrary scaling to make the normalized energy on the radial plot (part *A*) and transverse plot (part *C*) easier to compare. Note that all panels share the same time axis.

table 6) and 50 km (BDAS; table 5). We show station HAQS (figs. 19, 20) as exemplary of these northernmost stations, even though we list it in table 6 as an Arabian Shield station because of its elevation at 450 m. At station HAQS, we chose optimal weights of 0.4/0.3/0.3 and obtain *H* and *k* values of 28.0±0.7 km and 1.77±0.03, respectively.

Coastal station QNF01 (table 5) lies on the coast of the southern Red Sea rift margin (fig. 21*A*) and is one of the stations for which we were unable to obtain a reliable estimate of *H* and *k* via standard *H-k* stacking, as both the *H-k* plots (fig. 21*C–E*) and the PRFs (fig. 22) are noisy. Instead, we used PWS *H-k* stacking (fig. 21*F*) that requires consistency between the Ps, 3p1s, and 2p2s phases (fig. 21*C–E*) and yielded H = 36.6±0.3 km and k = 1.71±0.01. Moveout curves for each of these phases are plotted in figure 22*A* and appear to match coherent signal in the PRFs, even though the resulting crustal thickness of 36.6 km indicates a surprising lack of crustal thinning here.

Tertiary sedimentary rocks are locally more than 4 km thick at the coast (Cole and others 1995), but most of the seismic stations are deployed on or close to crystalline basement and were not corrected for overlying sediments. The probable exceptions are station QNF01 (figs. 21, 22) in the Ghawwas basin (for which PWS was required to achieve a solution), which we corrected for an assumed 1-km sedimentary thickness (Hughes and Johnson, 2005), and the Jazā‘ir Farasān (Farasan Islands) stations (FRSS and FRSS2), which we corrected for 0.6 km of sedimentary rocks (Almalki and Bantan, 2016). Table 5 gives *H-k* results for all the Red Sea rift and coastal stations.

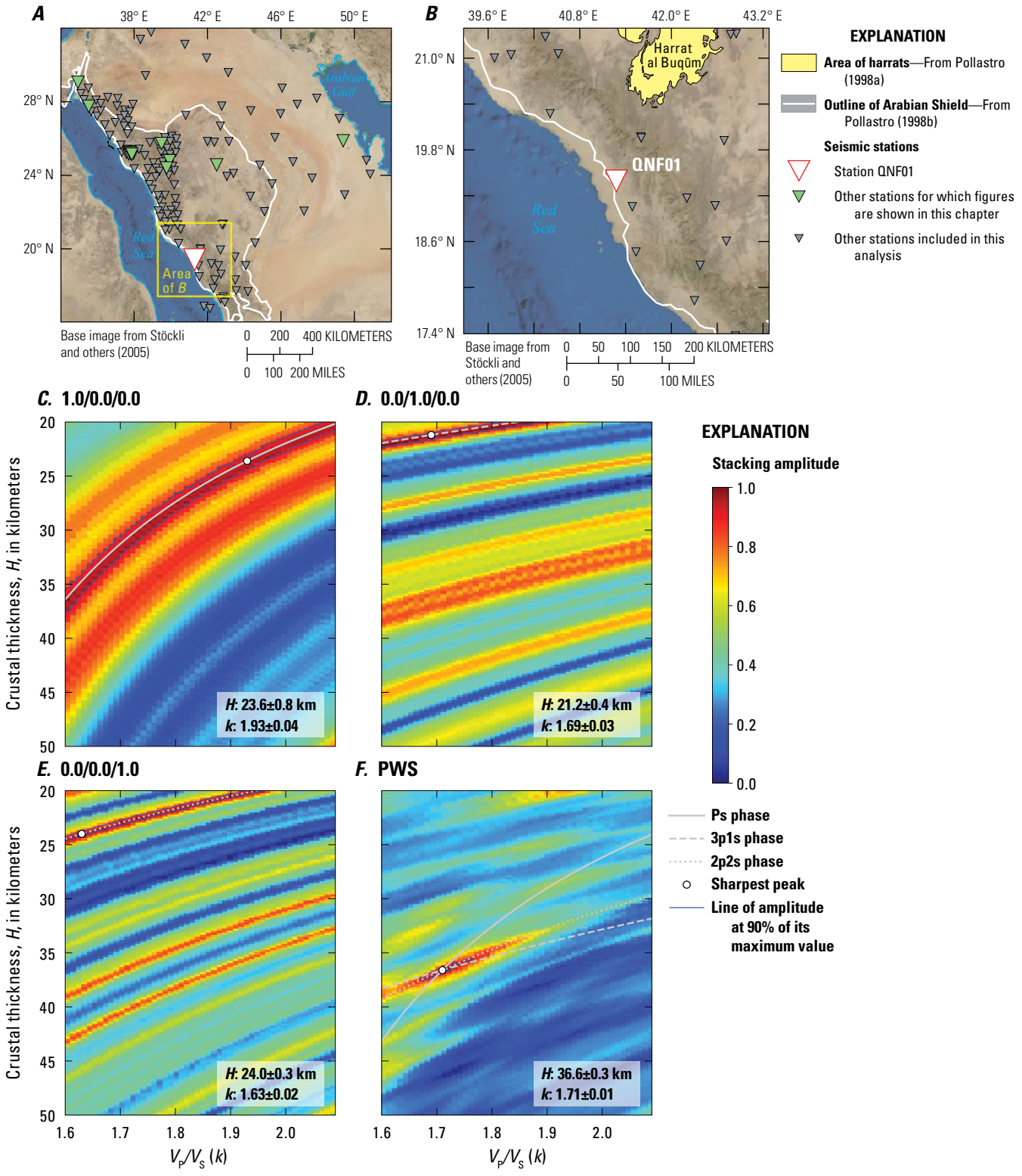

Figure 21. Location maps and plots of the receiver function analysis for coastal seismic station QNF01 in the Kingdom of Saudi Arabia (table 5). *A*, Map of the Arabian Peninsula region. *B*, Zoomed-in map of the region around station HAQS. *C*, Plot of Ps single-phase *H-k* stack (with $w_1/w_2/w_3$ stacking weights of 1.0/0.0/0.0). *D*, Plot of 3p1s single-phase *H-k* stack (0.0/1.0/0.0). *E*, Plot of 2p2s single-phase *H-k* stack (0.0/0.0/1.0). *F*, Plot of optimized *H-k* stack obtained via raw phase-weighted stacking (PWS), indicates a crustal thickness (*H*) of 36.6±0.3 kilometers (km) and V_P/V_S ratio (*k*) of 1.71±0.01. V_P is P-wave velocity and V_S is S-wave velocity; %, percent.

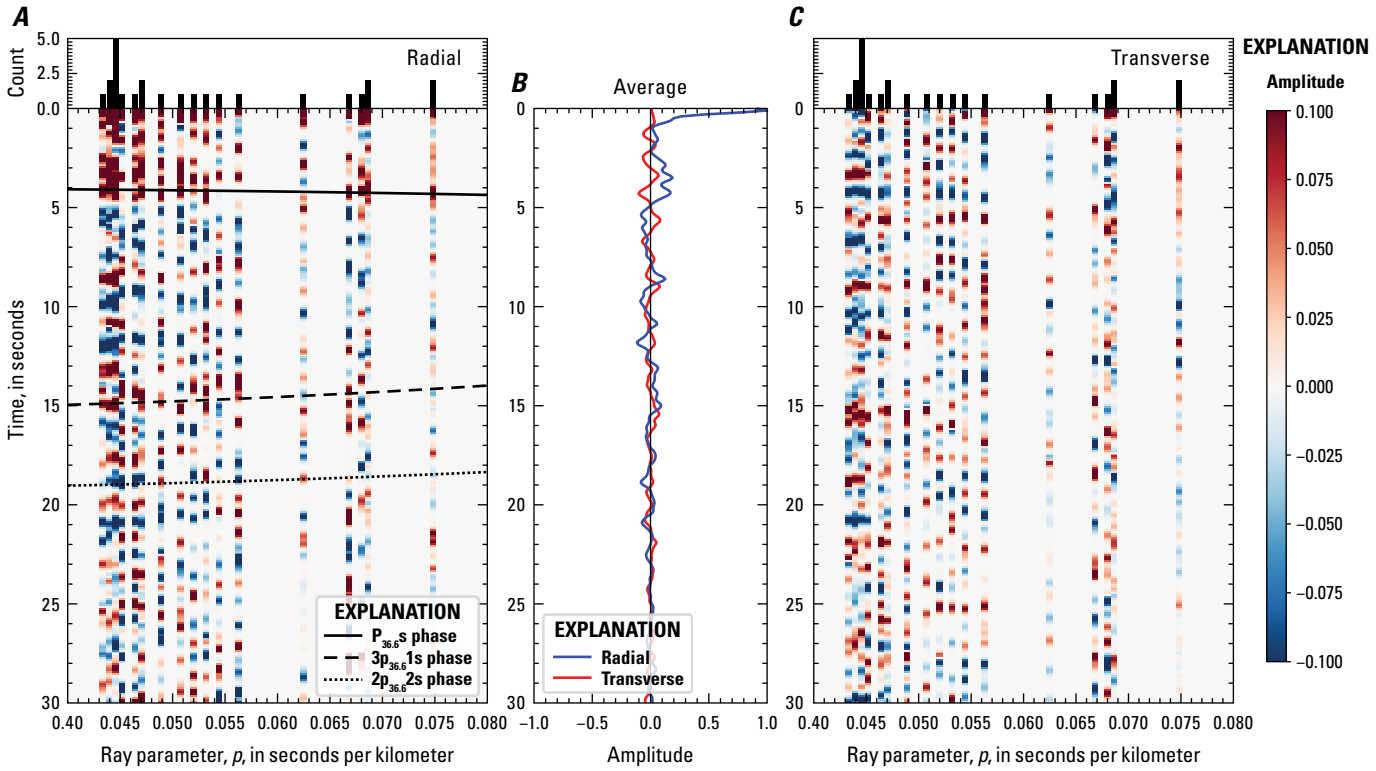

Figure 22. Plots of P-wave receiver function (PRF) gathers for coastal seismic station QNF01 in the Kingdom of Saudi Arabia (fig. 21; table 5). *A*, Radial component of PRFs versus ray parameter (*p*). Individual PRFs are normalized to the maximum amplitude within the time window shown, binned, and normalized by the number of traces per bin (count). *B*, Average of all individual normalized radial and transverse components of PRFs. Transverse components additionally multiplied by 0.3. *C*, Transverse component of PRFs versus ray parameter, normalized as in part *A* and multiplied by 0.3 as in part *B*. Multiplication by 0.3 is an arbitrary scaling to make the normalized energy on the radial plot (part *A*) and transverse plot (part *C*) easier to compare. Note that all panels share the same time axis.

Arabian Shield

Arabian Shield station AFFS (fig. 3*A*; table 6) lies just west of the boundary between the Arabian Shield and Arabian Platform and is installed on crystalline basement. The clear Moho Ps phase at 4–5 s (fig. 4*A*) resembles signals from the harrat stations (for example, LNY02, KBR08, and RHT09; figs. 10, 14, 16). The transverse component of the PRF for station AFFS is as clear as the radial component on the amplitude-normalized sections (fig. 4*B*), perhaps owing to a dipping structure at the Moho. *H-k* stacking results for all Arabian Shield stations are listed in table 6.

Arabian Platform

Arabian Platform stations have predictably worse data quality than stations on the Arabian Shield (fig. 1*B*) (owing to higher noise levels compared to stations on hard rock). Only 12 percent of Arabian Shield stations, but ~25 percent of Arabian Platform stations, did not produce an acceptable *H-k* result. Data quality generally worsens, and the number of acceptable PRFs decreases, as the sedimentary thickness increases to the east and intra-sedimentary reverberations become stronger. We show one example of an Arabian Platform station (BOQS; table 7) near the Arabian Gulf (fig. 23*A*) for which resonance removal was required.

Table 6. *H-k* stacking results for the Arabian Shield area stations in the Kingdom of Saudi Arabia.

[Stations listed from north to south. Coordinates referenced to the World Geodetic System of 1984. w_i are the stacking weights for each phase. *H*, depth to Mohorovičić discontinuity (Moho) in kilometers (km) below the surface (thickness for stations with sedimentary cover); $k = V_P/V_S$ where V_P is P-wave velocity and V_S is S-wave velocity; $2\sigma_H$ and $2\sigma_k$, uncertainty at the two standard deviation level for *H* and *k*, respectively]

Station	Latitude (°N)	Longitude (°E)	w_1	w_2	w_3	*H* (km)	$2\sigma_H$	*k*	$2\sigma_k$
HAQS	29.06	34.93	0.4	0.3	0.3	28.0	0.7	1.77	0.03
JLOS	28.74	35.49	0.4	0.3	0.3	31.4	0.4	1.62	0.02
WTBKS	28.08	35.91	0.5	0.5	0.0	32.4	0.5	1.93	0.03
SHQRE	27.90	36.17	0.5	0.5	0.0	31.2	0.6	1.83	0.03
HIL04	27.76	42.76	0.4	0.3	0.3	39.0	0.6	1.79	0.02
DESA[1]	27.51	36.16	⅓	⅓	⅓	29.0	0.2	1.90	0.01
HIL03	27.25	40.80	0.4	0.3	0.3	36.2	0.7	1.77	0.02
URD04	27.08	37.26	0.4	0.3	0.3	36.8	0.6	1.73	0.02
URD01	26.95	37.66	0.4	0.3	0.3	38.2	0.5	1.75	0.02
BIDS	26.87	36.96	0.4	0.3	0.3	35.6	0.6	1.72	0.03
QSMS	26.67	42.69	0.5	0.5	0.0	36.0	0.7	1.80	0.02
URD03	26.67	37.45	0.4	0.3	0.3	36.8	0.8	1.74	0.03
URD02	26.62	37.86	0.5	0.5	0.0	37.8	0.9	1.69	0.03
OLAS	26.25	37.63	0.5	0.5	0.0	36.2	0.5	1.73	0.03
HIL01	25.83	41.99	0.4	0.3	0.3	36.0	0.7	1.73	0.02
ARSS	25.83	43.15	0.4	0.3	0.3	38.8	0.5	1.74	0.02
UQSK	25.79	42.36	0.4	0.3	0.3	36.8	0.4	1.75	0.02
NUMJS	25.63	37.27	0.4	0.3	0.3	24.4	0.4	1.80	0.02
AFFS	24.56	42.48	0.4	0.3	0.3	35.2	0.4	1.75	0.02
DWDS	24.54	44.84	0.4	0.3	0.3	42.8	0.6	1.74	0.03
RHT06	24.38	39.19	0.4	0.3	0.3	33.4	0.6	1.71	0.04
RHT13	24.21	39.37	0.5	0.5	0.0	36.2	0.6	1.71	0.03
BJDH	24.09	43.40	0.5	0.5	0.0	35.6	0.6	1.75	0.02
AFIF	23.93	43.04	0.4	0.3	0.3	36.8	0.6	1.72	0.02
RHT05	23.91	39.16	0.4	0.3	0.3	35.6	0.8	1.71	0.03
BADR[1]	23.88	36.66	⅓	⅓	⅓	24.2	0.3	1.80	0.02
RAYN	23.52	45.50	0.5	0.5	0.0	39.8	0.6	1.77	0.02
MSTR	23.23	39.00	0.5	0.5	0.0	25.4	0.4	1.90	0.03

Table 6. *H-k* stacking results for the Arabian Shield area stations in the Kingdom of Saudi Arabia.—Continued

Station	Latitude (°N)	Longitude (°E)	w_1	w_2	w_3	H (km)	$2\sigma_H$	k	$2\sigma_k$
NUBA	22.88	39.30	0.5	0.5	0.0	33.4	0.5	1.71	0.02
HALM	22.85	44.32	0.4	0.3	0.3	36.4	0.4	1.75	0.02
HRML	22.01	45.09	0.4	0.3	0.3	41.6	0.3	1.76	0.01
SHRS	21.50	40.20	0.4	0.3	0.3	34.8	0.4	1.72	0.02
RYNS	21.32	42.85	0.5	0.5	0.0	37.0	0.4	1.74	0.02
RANI	21.31	42.78	0.4	0.3	0.3	38.6	0.7	1.70	0.02
TAIF	21.28	40.35	0.4	0.3	0.3	37.4	0.4	1.76	0.02
FRAS	21.06	40.52	0.4	0.3	0.3	39.6	0.7	1.72	0.03
KAMS	20.30	44.57	0.4	0.3	0.3	39.2	0.4	1.78	0.01
BAHS	19.97	41.60	0.4	0.3	0.3	38.0	0.6	1.73	0.03
BLJS	19.96	41.61	0.4	0.3	0.3	38.0	0.6	1.73	0.02
BISH	19.92	42.69	0.5	0.5	0.0	36.4	0.4	1.83	0.02
TATS	19.54	43.48	0.4	0.3	0.3	39.0	0.7	1.83	0.03
NAMS	19.17	42.20	0.4	0.3	0.3	41.6	0.5	1.71	0.02
RHWAS	19.07	44.07	0.5	0.5	0.0	38.4	0.7	1.80	0.02
ENMS	19.07	42.57	0.4	0.3	0.3	42.8	0.6	1.70	0.02
WBHS	18.61	42.72	0.4	0.3	0.3	41.2	0.5	1.74	0.02
KNGHS	18.29	43.50	0.5	0.5	0.0	45.4	0.6	1.76	0.02
SODA	18.29	42.38	0.4	0.3	0.3	38.0	0.6	1.74	0.02
DJNS	17.70	43.54	0.4	0.3	0.3	47.6	0.6	1.66	0.02
NJRNS	17.65	44.19	0.4	0.3	0.3	41.2	0.5	1.82	0.02

[1]Phase-weighted stacking (PWS) *H-k* stacking results.

Table 7. *H-k* stacking results for the Arabian Platform area stations in the Kingdom of Saudi Arabia.

[Stations listed from north to south. Coordinates referenced to the World Geodetic System of 1984. w_i are the stacking weights for each phase. H, depth to Mohorovičić discontinuity (Moho) in kilometers (km) below the surface (thickness for stations with sedimentary cover); $k = V_P/V_S$ where V_P is P-wave velocity and V_S is S-wave velocity; $2\sigma_H$ and $2\sigma_k$, uncertainty at the two standard deviation level for H and k, respectively. Corrected thickness = H–0.6×$h_{s\text{-}SJ2010}$, where $h_{s\text{-}SJ2010}$ is sedimentary thickness from Konert and others (2001; reproduced by Stern and Johnson, 2010) plus elevation above sea level. Where h_s is available from sedimentary *H-k* stacks, corrected thickness = H+h_s–0.6×($h_{s\text{-}SJ2010}$–h_s). —, no value calculated]

Station	Latitude (°N)	Longitude (°E)	w_1	w_2	w_3	H (km)	$2\sigma_H$	k	$2\sigma_k$	Corrected thickness (km)
WELA[1]	31.78	38.91	0.4	0.3	0.3	34.3	0.4	1.60	0.03	34.1
			0.05	0.70	0.25	2.09	0.10	3.60	0.14	
HANO[1]	31.39	38.33	0.5	0.5	0	32.7	0.4	1.73	0.03	33.9
			0.25	0.75	0.0	2.38	0.04	2.05	0.14	
NARAR[1]	31.12	40.75	0.5	0.5	0	38.5	1.0	1.70	0.02	40.7
			0.25	0.75	0.0	5.40	0.20	4.20	0.19	
SARAR[1]	30.38	41.94	0.4	0.3	0.3	34.5	1.2	1.72	0.03	36.7
			0.05	0.70	0.25	5.30	0.40	1.65	0.17	
WRFHA[1]	29.58	43.11	0.4	0.3	0.3	40.0	0.4	1.87	0.02	37.0
			0.05	0.70	0.25	0.72	0.20	1.50	0.59	
JOFS	29.41	38.61	0.4	0.3	0.3	40.0	0.6	1.73	0.03	36.9
HBTS	28.73	46.05	0.5	0.5	0.0	43.6	0.4	1.79	0.02	40.1

Table 7. *H-k* stacking results for the Arabian Platform area stations in the Kingdom of Saudi Arabia.—Continued

Station	Latitude (°N)	Longitude (°E)	w_1	w_2	w_3	H (km)	$2\sigma_H$	k	$2\sigma_k$	Corrected thickness (km)
TBKS	28.23	36.55	0.5	0.5	0.0	35.4	0.5	1.80	0.04	34.6
KFJS	28.19	47.94	0.5	0.5	0.0	47.0	0.8	1.83	0.04	41.5
URD10	28.17	37.10	0.4	0.3	0.3	34.8	0.7	1.74	0.02	34.5
QLABS	27.86	37.93	0.4	0.3	0.3	35.8	0.8	1.76	0.03	34.5
QYSM[1]	27.85	46.88	0.4	0.3	0.3	44.3	0.3	1.74	0.02	41.9
			0.05	0.70	0.25	0.95	0.05	1.60	0.16	
URD12	27.76	37.06	0.5	0.5	0.0	34.6	0.9	1.76	0.04	34.6
URD13	27.54	37.48	0.5	0.5	0.0	35.0	0.6	1.77	0.03	35.0
ASYS[1]	27.50	44.34	0.4	0.3	0.3	40.9	0.4	1.78	0.02	45.4
			0.05	0.70	0.25	3.80	0.1	1.60	0.11	
URD14	27.44	37.74	0.4	0.3	0.3	34.6	0.41	1.74	0.02	34.6
RQBS[1]	27.34	45.96	0.4	0.3	0.3	36.9	0.4	1.95	0.03	35.1
			0.05	0.70	0.25	0.72	0.10	1.60	0.34	
URD15	27.25	37.45	0.5	0.5	0.0	38.0	0.5	1.71	0.02	38.4
NRYS	27.08	49.16	0.5	0.5	0.0	45.8	0.8	1.71	0.02	41.0
MJMS	26.05	45.66	0.5	0.5	0.0	45.2	0.5	1.78	0.02	43.3
BOQS[1]	25.87	49.38	0.5	0.5	0.0	40.5	1.4	1.73	0.04	42.4
			0.25	0.75	0.0	1.60	0.2	4.25	0.34	
SLWS[1]	24.80	50.64	0.4	0.3	0.3	40.4	0.7	1.73	0.04	40.5
			0.05	0.70	0.25	2.89	0.1	3.55	0.15	
RIYD[1]	24.72	46.64	0.4	0.3	0.3	31.0	1.2	2.12	0.04	36.6
			0.05	0.70	0.25	4.50	0.50	1.50	0.57	
BTHS[1]	24.05	50.85	0.4	0.3	0.3	38.7	0.7	1.75	0.03	39.3
			0.05	0.70	0.25	2.95	0.05	1.60	0.18	
KHRJ[1]	23.84	47.68	0.4	0.3	0.3	41.8	0.4	1.78	0.02	40.4
			0.05	0.70	0.25	0.69	0.05	1.60	0.16	
HRDS	22.93	49.46	0.4	0.3	0.3	46.1	0.6	1.79	0.02	42.3
LYLS[1]	22.039	47.24	0.5	0.5	0.0	43.8	0.5	1.77	0.03	42.1
			0.25	0.75	0.0	0.60	0.04	4.60	0.21	

[1]Top row of values are subsedimentary crustal *H-k* stacking results; bottom row of values are sedimentary *H-k* stacking results.

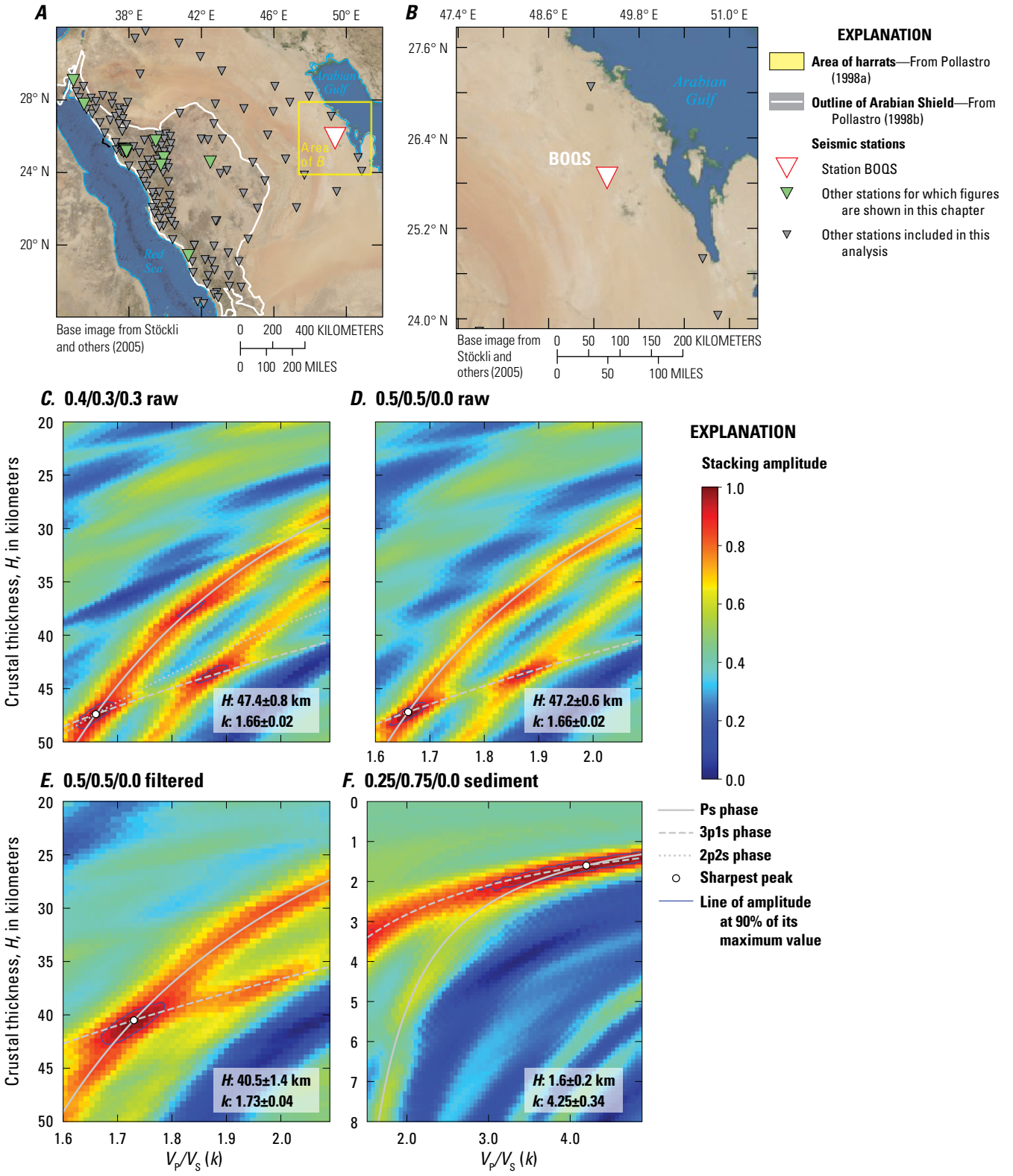

Figure 23. Location maps and plots of the receiver function analysis for Arabian Platform seismic station BOQS in the Kingdom of Saudi Arabia (table 7). *A*, Map of the Arabian Peninsula region. *B*, Zoomed-in map of the region around station BOQS. *C*, Plot of Ps, 3p1s, and 2p2s single-layer multi-peaked *H-k* stack for the raw P-wave receiver functions (PRFs) (with $w_1/w_2/w_3$ stacking weights of 0.4/0.3/0.3). *D*, Plot of Ps and 3p1s single-layer multi-peaked *H-k* stack for the raw PRFs (0.5/0.5/0.0) (see fig. 24*C*). *E*, Plot of optimized Ps and 3p1s *H-k* stack (0.5/0.5/0.0) for the subsedimentary crystalline crust. *F*, Plot of optimized *H-k* stack (0.25/0.75/0.0) for sedimentary crust. Values are given for crustal thickness (*H*), in kilometers (km), and V_P/V_S ratios (*k*). V_P is P-wave velocity and V_S is S-wave velocity; %, percent.

The raw *H-k* stacks (fig. 23*C*, *D*) are multi-peaked and dominated by the two possible Ps phase arrival peaks at ~5 and ~6 s (fig. 24), with *H-k* maxima at ~44 km (earlier and higher amplitude peak at ~6 s, $P_{43.8}s$) and ~47 km (lower amplitude peak at ~5 s, $P_{47.2}s$) (fig. 24*C*). Resonance removal (fig. 23*E*) successfully merges the two bands of high likelihood at ~38 and ~48 km (fig. 23*C*, *D*) into a single focus typical of *H-k* stacks lacking sedimentary effects (for example, fig. 13*F*). In figure 24, we show the filtered (fig. 24*A*) and unfiltered (fig. 24*C*) data and moveout curves for different *H-k* stacking results. The preferred Moho depth of 40.5 km is interpreted as the subsedimentary crustal thickness (not the total crustal thickness), assuming a constant V_p of 6.5 km/s. The sedimentary *H-k* stack (fig. 23*F*) is less well constrained, with implied sedimentary thickness h_s of ~1.5–3.0 km and k of ~3–5. These values of k suggest that sedimentary V_p is <2 km/s based on global compilations (fig. 7) but such an interpretation is inconsistent with the *H-k* stack, which assumes the basin-wide average sedimentary V_p = 4 km/s. The strong Ps conversion at 1.5 s (fig. 24) is from a very shallow converter, far shallower than the ~7-km Phanerozoic sedimentary thickness known in this area (fig. 1*B*; Konert and others, 2001 [reproduced by Stern and Johnson, 2010]). This example illustrates the need to correct the raw crustal thicknesses according to the entire Phanerozoic basin thicknesses reported by Konert and others, 2001 (reproduced by Stern and Johnson, 2010) (fig. 1*B*). *H-k* stacking results for all Arabian Platform stations are given in table 7.

Discussion

Regional Averages

The *H-k* stacking results (fig. 25*A*, *B*) show that the Arabia Plate is thinnest near the coast of the Red Sea and thickens away from the rifted margin, as expected. The average total thickness of the crust across the entire array is 34.9±4.7 km (1σ uncertainty). The average total thicknesses of the coastal (rift margin), Arabian Shield, and Arabian Platform crust (29.1±4.1 km, 36.6±4.8 km, and 38.4±3.4 km, respectively; see table 8) are all within uncertainty of the global averages for these crustal types (30.5±6.0 km, 40.8±7.0 km, and

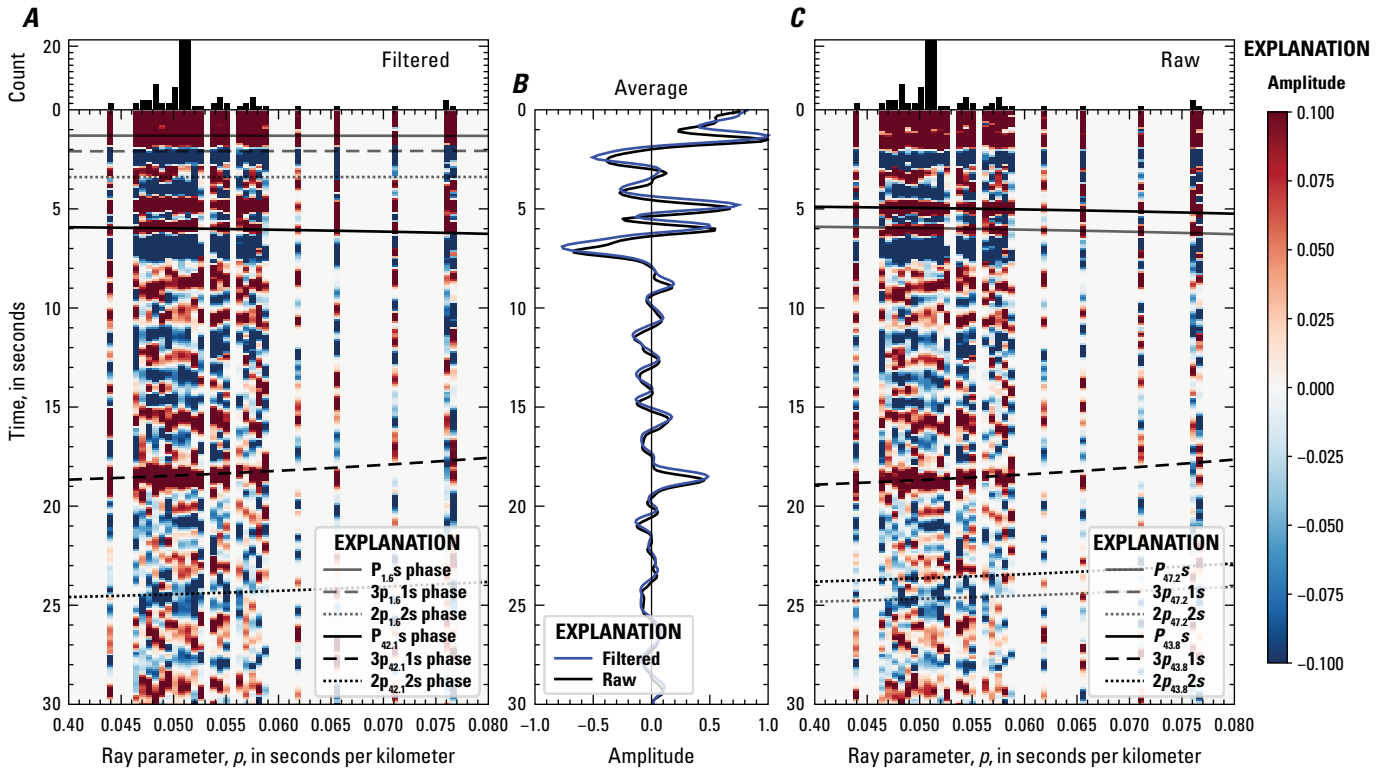

Figure 24. Plots of P-wave receiver function (PRF) gathers for Arabian Platform seismic station BOQS in the Kingdom of Saudi Arabia (fig. 23; table 7). *A*, Radial component of PRFs versus ray parameter (p) after application of the resonance-removal filter. Theoretical moveout curves were determined from *H-k* stacks of sedimentary and subsedimentary crystalline crust. *B*, Comparison of average filtered and raw radial components of PRFs. *C*, Radial component of PRFs without application of the resonance-removal filter and moveout curve for the earliest candidate Ps arrival chosen from standard *H-k* stacking. Note that all panels share the same time axis.

39.0±7.0 km, respectively; Mooney and others, 1998). Analytical errors underestimate the uncertainty in the value for the Arabian Platform because of the inability of the sedimentary *H-k* stack to obtain true sedimentary thicknesses and the necessity to assume an a priori sedimentary V_P when making corrections for sedimentary thickness (as discussed in the "Data and Methods" section). The average total crustal thickness of the harrats is 34.7±1.6 km (table 8).

In map view, the crustal thicknesses show systematic variation (fig. 25*A–C*). Although it may appear that the V_P/V_S ratios have systematically lower values near the Red Sea rift (fig. 25*D*), lower values are not borne out by statistical tests (discussed below) and the appearance is likely caused by the way in which the jet colormap distorts human perception of numerical values (Crameri and others, 2020). The average V_P/V_S ratio for the entire array is 1.76±0.07, deviating only slightly from a Poisson solid (1.73). Averages for each tectonic province are given in table 8. Although crustal thicknesses have distinct averages (fig. 26*A*), all regions of the Arabia Plate have statistically equivalent *k* values (fig. 26*B*).

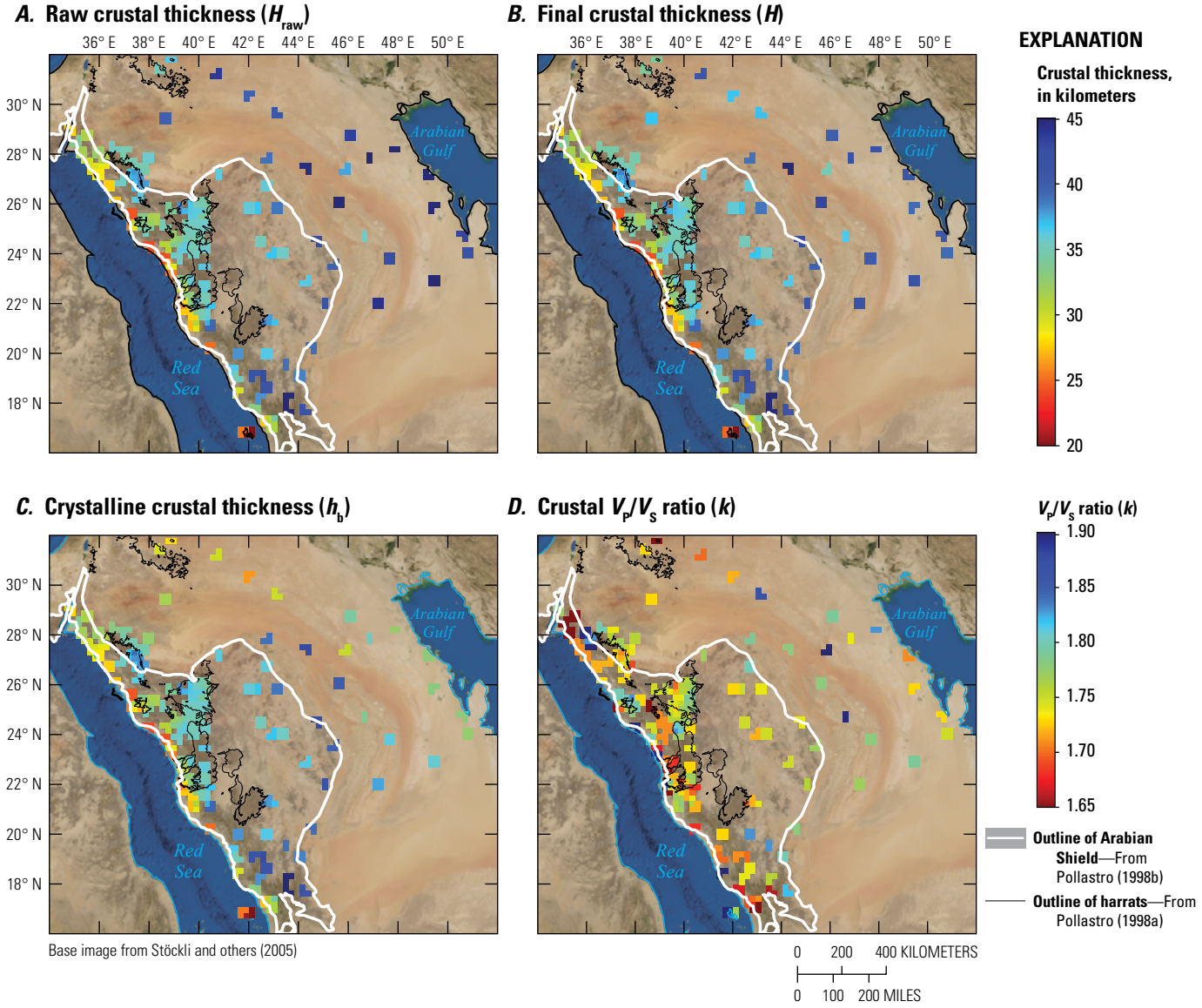

Figure 25. Maps of *H-k* stacking results in the study area in the Kingdom of Saudi Arabia. Values are averaged within bins with radii of 25 kilometers. *A*, Raw crustal thickness (H_{raw}) calculated from *H-k* stacks before sedimentary correction. *B*, Final crustal thickness (H) calculated from *H-k* stacks after sedimentary correction. *C*, Thickness of the crystalline crust (h_b); that is, final crustal thickness minus sedimentary thickness from Konert and others, 2001 (reproduced by Stern and Johnson, 2010). *D*, Crustal V_P/V_S ratio (k) (no sedimentary correction). *H*, depth to Mohorovičić (Moho) discontinuity; $k = V_P/V_S$ where V_P is P-wave velocity and V_S is S-wave velocity.

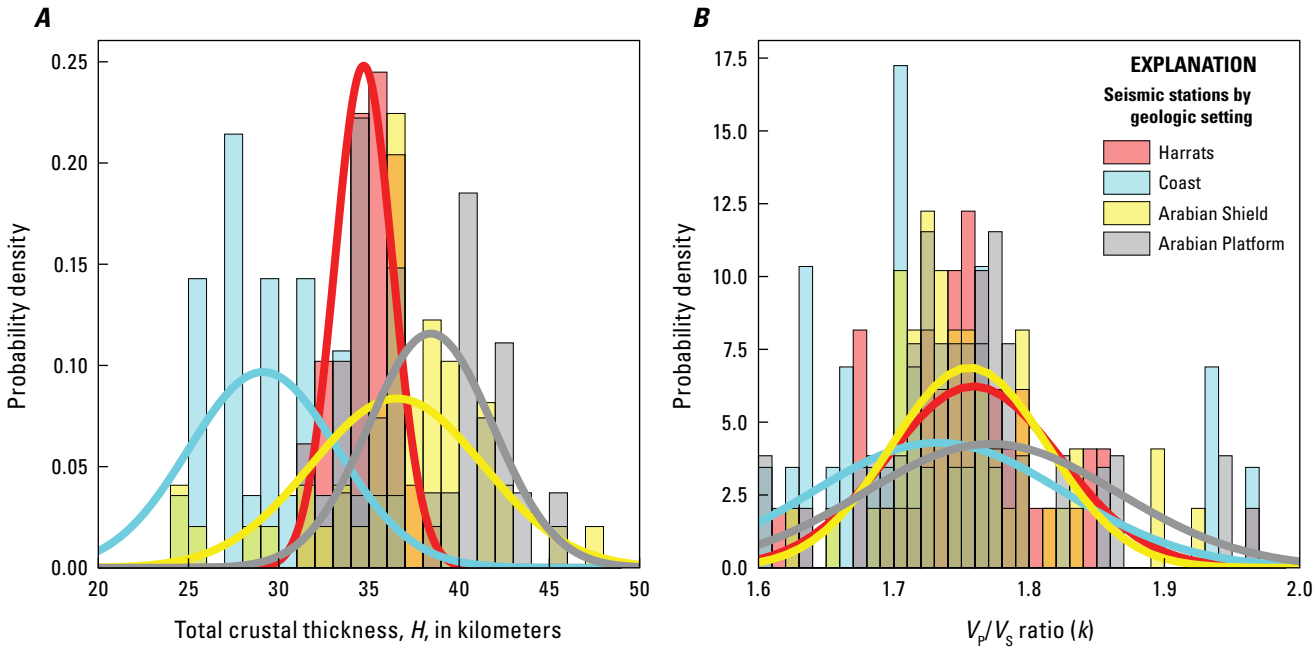

Figure 26. Histograms of the calculated total crustal thickness (*H*) of harrats, coast, Arabian Shield, and Arabian Platform areas in the Kingdom of Saudi Arabia. *A*, Corrected crustal thicknesses by geologic region. *B*, V_P/V_S ratios (*k*) by geologic region. Transparent colors allow the overlap to be visible. Gaussian curves are fits to the data. $k = V_P/V_S$, where V_P is the P-wave velocity and V_S is the S-wave velocity. Total crustal thickness (*H*) is depth to Mohorovičić (Moho) discontinuity.

Table 8. Regional summary of *H-k* results for the Kingdom of Saudi Arabia.

["Same" denotes total crustal thickness equal to crystalline crustal thickness for that geologic setting. *H*, depth to Mohorovičić discontinuity (Moho) in kilometers (km); $k = V_P/V_S$ where V_P is P-wave velocity and V_S is S-wave velocity; MMN line, Makkah-Madīnah-Nafud volcanic line. Uncertainties for individual stations are ±1 standard deviation (±1σ)]

Region	No. of stations	Crystalline crustal thickness (km)	Total crustal thickness (km)	Total crustal *k*
Coastal plain	29	29.1±4.2	29.1±4.1	1.73±0.09
Coastal plain (excluding Jazā'ir Farasān [Farasan Islands])	27	29.7±3.3	29.8±3.2	1.72±0.08
All harrats	49	34.7±1.6	Same	1.76±0.06
Harrats on MMN line	30	35.3±1.2	Same	1.75±0.04
Harrat Lunayyir	19	33.8±1.8	Same	1.77±0.09
Harrat Khaybar	12	35.5±1.3	Same	1.75±0.03
Harrat Rahat	18	35.2±1.1	Same	1.75±0.05
Arabian Shield	49	36.6±4.8	Same	1.76±0.06
Arabian Platform	27	33.8±3.6	38.4±3.4	1.77±0.09

Comparison with Previous P-wave Receiver Function Analyses

This study greatly improves upon the coverage of seismologically determined crustal thicknesses across the Arabia Plate and also includes the distinction between total crustal thickness (sediment + crystalline crust) and crystalline crustal thickness (table 8). Several previous PRF studies of crustal thickness of the Arabia Plate (table 9) all lacked station coverage compared to the results presented here (Sandvol and others, 1998; Julià and others, 2003; Al-Damegh and others, 2005; Tkalčić and others, 2006; Tang and others, 2016, 2019). These previous studies did not distinguish between total crustal thickness and crystalline crustal thickness, nor did they carry out their analysis in the same provincial framework as we have done here. We reorganized their results (table 9) following the regional classification scheme used in this study to enable comparison in sequence: coastal plain (Red Sea rift flank), harrat, Arabian Shield, and Arabian Platform.

For coastal stations, Tang and others (2016) report an average total crustal thickness of 27.9±4.0 km across 11 stations and Al-Damegh and others (2005) report 25.1±6.1 km (6 stations), consistent with the average of 29.1±4.1 km determined in this study. Tkalčić and others (2006) reported 28.0 km for a single coastal station (YNBS), for which we obtained 24.0±0.7 km (table 5). This significant discrepancy is because Tkalčić and others (2006) put a greater emphasis on

Table 9. Regional summary of previous geophysical work on the crustal thickness of the Arabia Plate in the Kingdom of Saudi Arabia.

[Arranged by geologic region; mean crustal thickness and number of stations from this study given in parentheses. No., number; MMN line, Makkah-Madīnah-Nafud volcanic line; km, kilometer. Uncertainties are ±1 standard deviation (±1σ)]

Authors of previous studies	No. of stations	Average thickness (previous studies) (km)
Coastal plain (29.1±4.1 km; 29 stations)		
Al-Damegh and others (2005)	6	25.1±6.1
Tang and others (2016)	11	27.9±4.0
Tkalčić and others (2006)	1	28.0
Harrats (34.7±1.6 km; 49 stations)		
Tang and others (2016)	23	33.5±2.7
MMN line (35.3±1.2 km; 30 stations)		
Tang and others (2016)	12	34.2±2.4
Harrat Lunayyir (33.8±1.8 km; 19 stations)		
Tang and others (2016)	11	32.7±3.0
Harrat Khaybar (35.5±1.3 km; 12 stations)		
Al-Damegh and others (2005)	1	35.2
Tang and others (2016)	1	35.1
Tkalčić and others (2006)	1	35.0
Harrat Rahat (35.2±1.1 km; 18 stations)		
Tang and others (2016)	11	34.1±2.5
Arabian Shield (36.6±4.8 km; 49 stations)		
Al-Damegh and others (2005)	12	35.6±6.0
Sandvol and others (1998)	7	39.1±2.9
Tang and others (2016)	14	36.9±4.7
Tkalčić and others (2006)	5	37.6±2.6
Arabian Platform (38.4±3.4 km; 27 stations)		
Al-Damegh and others (2005)	3	37.1±4.2
Sandvol and others (1998)	1	45.0
Tang and others (2016)	7	42.4±5.6
Tkalčić and others (2006)	3	36.0±2.6

fitting the long-period PRF, instead of the short-period PRF (see their fig. 11*J*), for this station. Tang and others (2016) reported 25.0±0.8 km, close to the result from this study.

All the average harrat results are consistent with the previous studies, likely because of large station numbers, generally high-quality data, and no sedimentary interference. The Arabian Shield result (crustal thickness of 36.6±4.8 km) is lower than most, but within error of all previous studies, likely because we included a greater number of seismic stations in the western Arabian Shield, closer to the coast. On the Arabian Platform, the average raw total crustal thickness (40.4±4.3 km) is within error of previous results. Inclusion of the sedimentary correction (average 38.4±3.4 km) increases the discrepancy from the conventional analysis of Tang and others (2016) (42.4±5.6 km) but agrees with Tkalčić and others' (2006) result (36.0±2.6 km) (table 9), indicating that their inclusion of long-period surface waves in a joint inversion with PRFs reasonably compensated for the sedimentary cover without necessitating an additional sedimentary correction. No previous studies published estimates of crystalline crustal thickness (we estimate the Arabian Platform average is 33.8±3.6 km) (table 8). Although the thickness of the subsedimentary crystalline crust has relatively large uncertainty owing to the uncertain nature of the sedimentary corrections, it indicates that the Arabian Platform crust is ~10 percent (~3 km) thinner than the Arabian Shield.

Statistical Comparisons of Geophysical Characteristics by Region

A long-standing question about the Arabia Plate is whether different crustal terranes have different crustal structures. Stern and Johnson (2010) claim that the Arabian Platform is 3–4 km thicker than the Arabian Shield, and Tang and others (2016) claim they can distinguish between crustal thicknesses of different Proterozoic terranes and that k values at Harrat Lunayyir are anomalously high. However, these claims were not evaluated statistically in their reports. Here, we use various statistical methods to test the equivalence between different geologic regions.

First, we use Welch's t-test method (Welch, 1947), which generalizes the Student's t-test to allow the measurements being compared to contain both different sized populations and different variances. We use a two-tailed test of two scenarios (the null hypothesis, H_0, that the population means are equal versus the alternative hypothesis, H_1, that the population means are different) and calculate the test statistic, t, and the degrees of freedom, associated with the estimated variances. Calculating the Student's distribution with these input values allows us to calculate the probability, p, that the null hypothesis (H_0) is true. At a 95 percent confidence threshold, we reject the null hypothesis (that is, the averages are too different to be explained by random chance) if $p<0.05$, and if

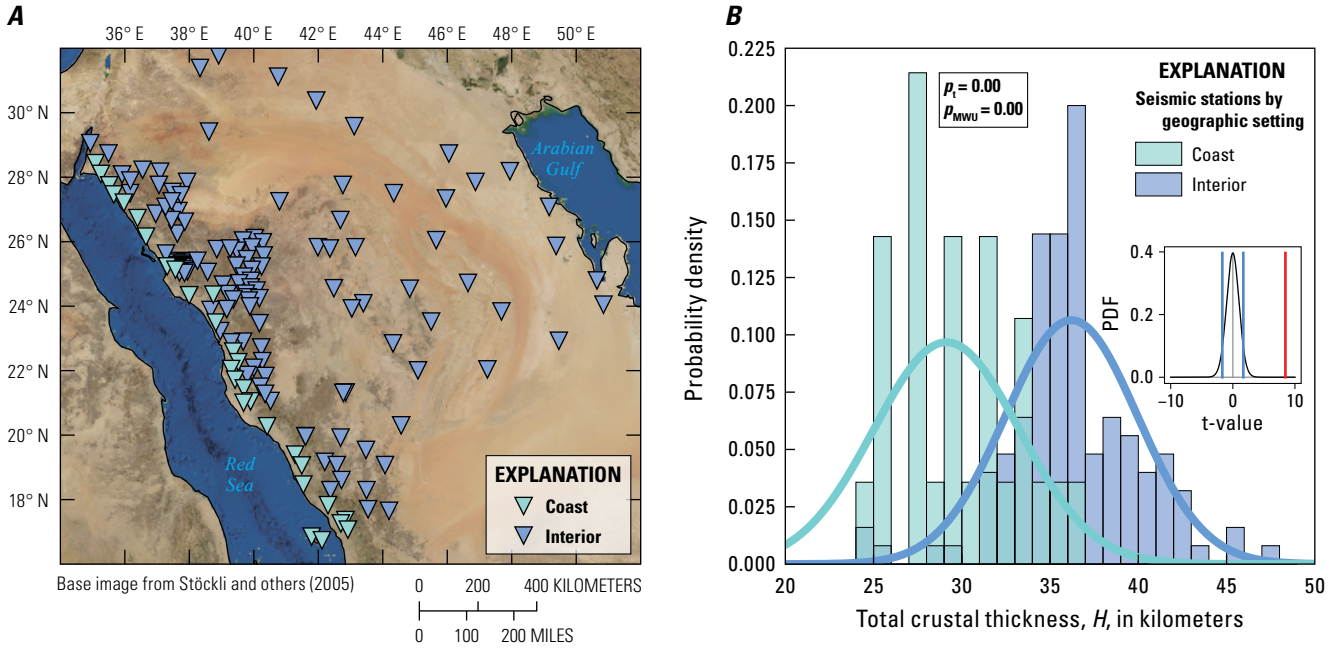

Figure 27. Map and histogram of coastal (that is, Red Sea rift margin) stations and interior stations in the Kingdom of Saudi Arabia. *A*, Map of coastal and interior seismic stations. *B*, Histogram of depth to Mohorovičić discontinuity (Moho) below the surface (total crustal thickness, *H*) for coastal and interior stations. Transparent colors allow the overlap to be visible. Gaussian curves are fits to the data. Inset graph in part *B* is the t-test, showing the probability density function (PDF) of the Student distribution for the two datasets (from Welch, 1947). Blue vertical bars are 95 percent confidence bounds; the red bar is the t-value of this comparison. If the red bar is within the blue bars, then the null hypothesis (H_0) is accepted, otherwise the alternative hypothesis (H_1, the hypothesis that the distributions are different) is accepted. In this case, the two population averages and distributions are very different ($p_t<10^{-4}$, $p_{MWU}<10^{-4}$). We denote the two different p-values as either p_t (t-test) or p_{MWU} (Mann-Whitney U [MWU] test; Mann and Whitney, 1947).

p>0.05, we accept the null hypothesis (that is, any differences between the averages can be explained by random chance).

As an additional test of equivalence between geologic regions we also use the Mann-Whitney U (MWU) test (Mann and Whitney, 1947), which is designed to compare population distributions instead of population means, and to cope with non-normal (for example, skewed) distributions (Fay and Proschan, 2010). We use the same two-tailed test as the t-test and calculate p, the probability that the null hypothesis is true. We denote the two different p-values as either p_t (t-test) or p_{MWU} (MWU test).

The thinnest crust, 16–25 km, is beneath the Jazā‘ir Farasān (Farasan Islands) stations. The two measurements, separated by only 37 km, differ greatly (by 9.4 km; FRSS2 and FRSS; table 5), perhaps because of complex overlying sedimentary structure (Almalki and Bantan, 2016), but bracket the previous active-source measurement (17.5 km; Mooney and others, 1985) and represent the transition from thin oceanic crust to thick continental crust.

The next thinnest crust is beneath the stations along the Red Sea rift margin. The average total thickness of crust beneath the coastal stations is 29.1±4.1 km, or 29.8±3.2 km if the Jazā‘ir Farasān results are excluded (table 8). Even excluding the Jazā‘ir Farasān stations, this value is statistically different from the average thickness of 36.2±3.8 km for the rest of the Arabia Plate (fig. 27). We note that the definition of “coastal” used here is necessarily arbitrary even though geologically informed (within 250 km of the Red Sea rift axis and at elevations ≤400 m above sea level), and other definitions would lead to different mean crustal thickness values.

Within the harrats, crustal thickness of Harrat Lunayyir is 33.8±1.8 km and the V_P/V_S ratio (k) is 1.77±0.09 (±1σ) (table 8). The scatter in k values far exceeds the analytical uncertainty of individual stations; however, this scatter exists between stations that are sufficiently close (fig. 28) that they share many ray paths contributing to their H-k results (fig. 2), and therefore are expected to have similar results. Hence, we conclude that the low analytical uncertainties fail to represent the oblique eccentricity of resolution in the H-k grid search, which we represent as 90 percent amplitude contours. Because crustal H and k represent secular evolutionary processes, we might expect correlations within provinces (fig. 29), as well as differences between them (figs. 26*B*, 29*A*). Figure 29 shows the lack of correlation between H and k, except apparently amongst the harrat stations. However, the slope of the apparent

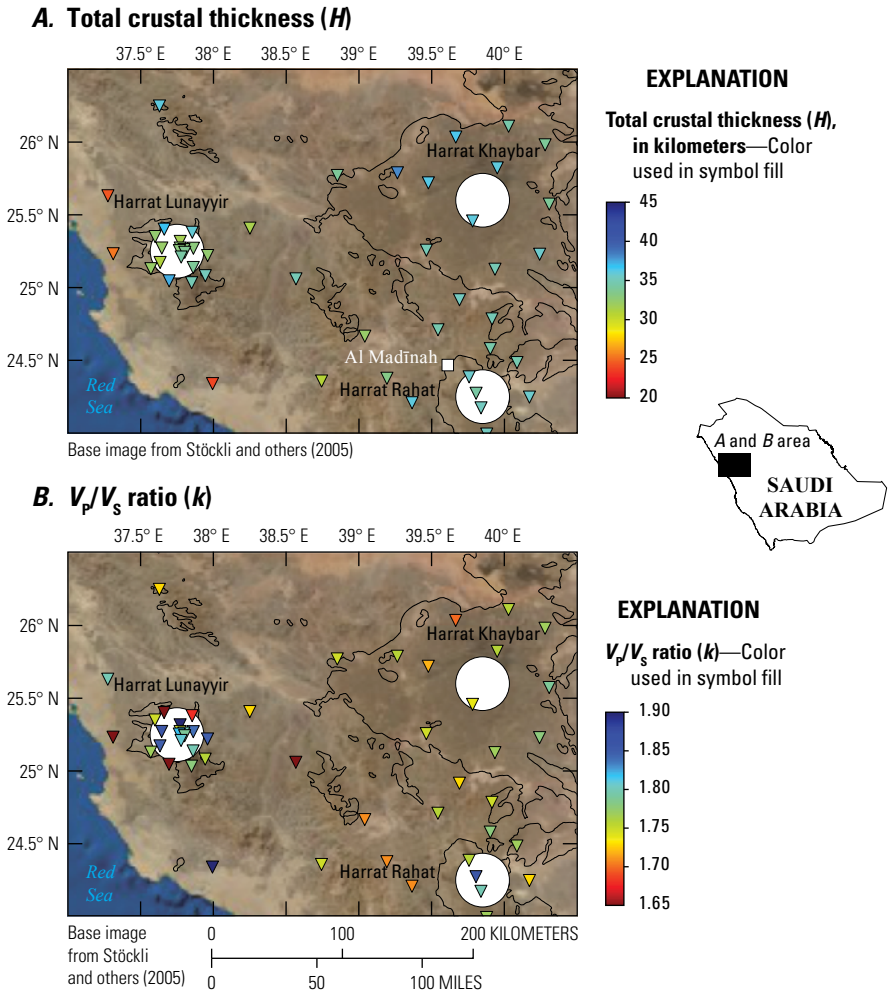

Figure 28. Maps of harrat H-k results in the Kingdom of Saudi Arabia. *A*, Total crustal thickness measurements (H) for each seismic station (triangle symbols). *B*, Crustal V_P/V_S ratio (k) for each seismic station (triangle symbols). Harrats are outlined in black. White circles are approximately located at the center of each harrat and have a radius of 25 kilometers (km). They show the averaging radius used to create figure 25, and the distance over which we anticipate commonality between stations owing to similar ray path coverage (fig. 2). H, depth to Mohorovičić (Moho) discontinuity; $k = V_P/V_S$ where V_P is P-wave velocity and V_S is S-wave velocity.

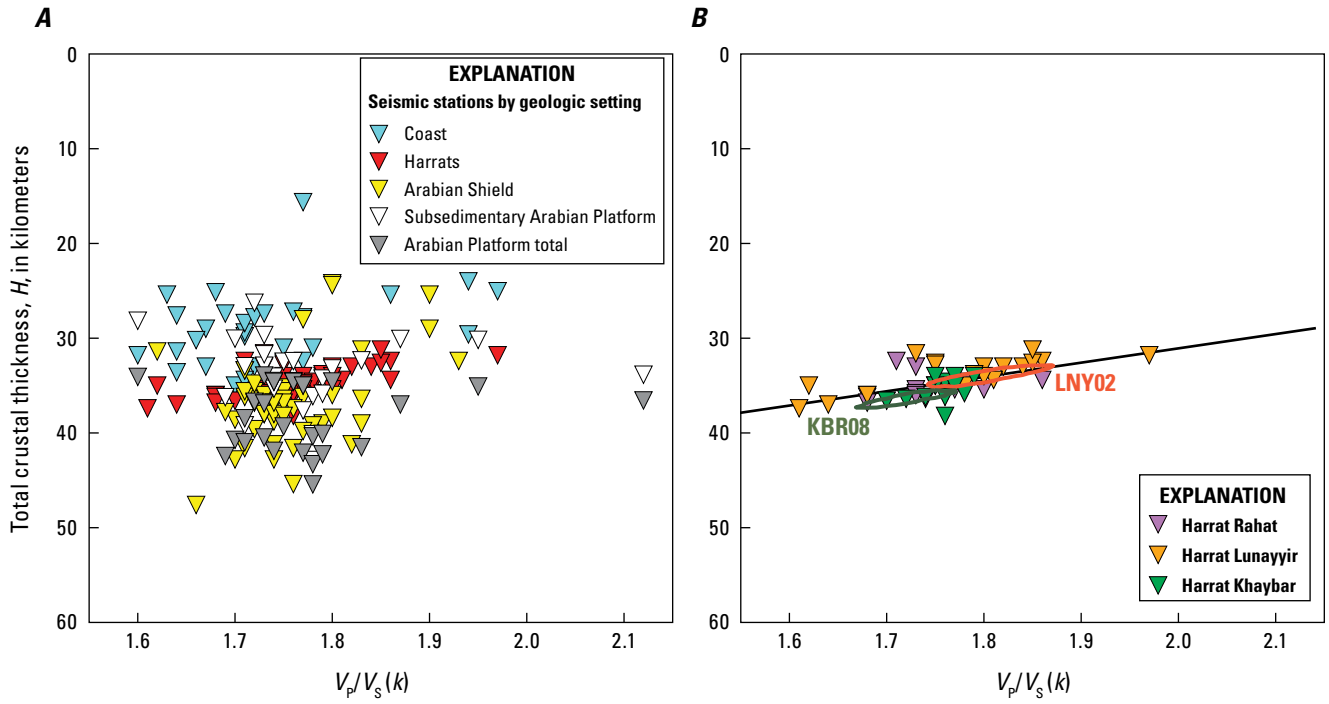

Figure 29. Plots of total crustal thickness (*H*) versus V_P/V_S ratio (*k*) in the Kingdom of Saudi Arabia. *A*, Seismic stations by geologic setting. Arabian Platform total is the total crustal thickness within the Arabian Platform, whereas subsedimentary Arabian Platform is the thickness of the subsedimentary crystalline crust. *B*, Harrat seismic stations only. Straight-line fit (black line) shows apparent crustal thinning with increasing *k*. 90 percent *H-k* confidence ellipses are shown for station KBR08 (blue) (figs. 13, 14; table 2) and station LNY02 (orange) (figs. 9, 10; table 3). *H*, depth to Mohorovičić (Moho) discontinuity; $k = V_P/V_S$ where V_P is P-wave velocity and V_S is S-wave velocity.

trend of *H* versus *k* for the harrat stations is the same as the slope of the *H-k* confidence ellipses (fig. 29*B*), suggesting that the trend is caused by real uncertainty in the *H-k* results, not geological differences. Indeed, adding mafic intrusions to increase *k* would also increase *H*. This is important because Tang and others (2016) proposed that the *k* values at Harrat Lunayyir are elevated in comparison to the Arabian Shield owing to solidified intrusions. The statistical testing methodology used in this study shows that the claim of Tang and others (2016) is not supported by their data, which consist of 11 Harrat Lunayyir measurements of *k* with a mean of 1.78±0.11 and 14 Arabian Shield measurements with a mean of 1.73±0.07. The t-test and MWU test applied to their data yield a p_t value of 0.17 and p_{mwu} value of 0.08, both above the 0.05 threshold, requiring acceptance of the null hypothesis that the *k* values of Harrat Lunayyir are statistically the same as for the rest of the Arabian Shield.

Harrat Khaybar has average crustal thickness of 35.5±1.3 km and average *k* of 1.75±0.03 (table 8). The consistency of results arises from both the low noise levels of the receiver functions and the well-resolved phase arrivals. Harrat Rahat has mean *H* and *k* values of 35.2±1.1 km and 1.75±0.05, respectively (table 8). The highest *k* values for Harrat Rahat (≥1.8) are given by the stations closest to the most volcanically productive part of the harrat (Stelten and others, 2023) where the thickness of Quaternary volcanic rocks is also greatest (Langenheim and others, 2019, 2023), but, as discussed for Harrat Lunayyir, we believe this variability in *k* is likely caused by inherent uncertainty.

The three major harrats in this study (Harrats Lunayyir, Rahat, and Khaybar) all have overlapping *H* and *k* values (fig. 30). The average crustal thickness in and near the harrats is 34.7±1.6 km, between that expected for extended crust and shields (Mooney and others, 1998). The *k* values for the three harrats are not statistically distinct (fig. 30*C*), but Harrat Lunayyir crust is distinctly thinner than that of Harrats Khaybar and Rahat, which are essentially identical (fig. 30*B*). This thickness difference may be explained by Harrat Lunayyir and its seismic stations being closer to the Red Sea rift axis than all the Harrat Khaybar stations and the majority of the Harrat Rahat stations. We expand upon this overall west-to-east crustal thickening trend below, but the trend can be seen by comparing harrat versus Arabian Shield crustal thickness (which are statistically distinct; fig. 26*A*), particularly among stations on the MMN line versus the western Arabian Shield (statistically the same, fig. 31*B*).

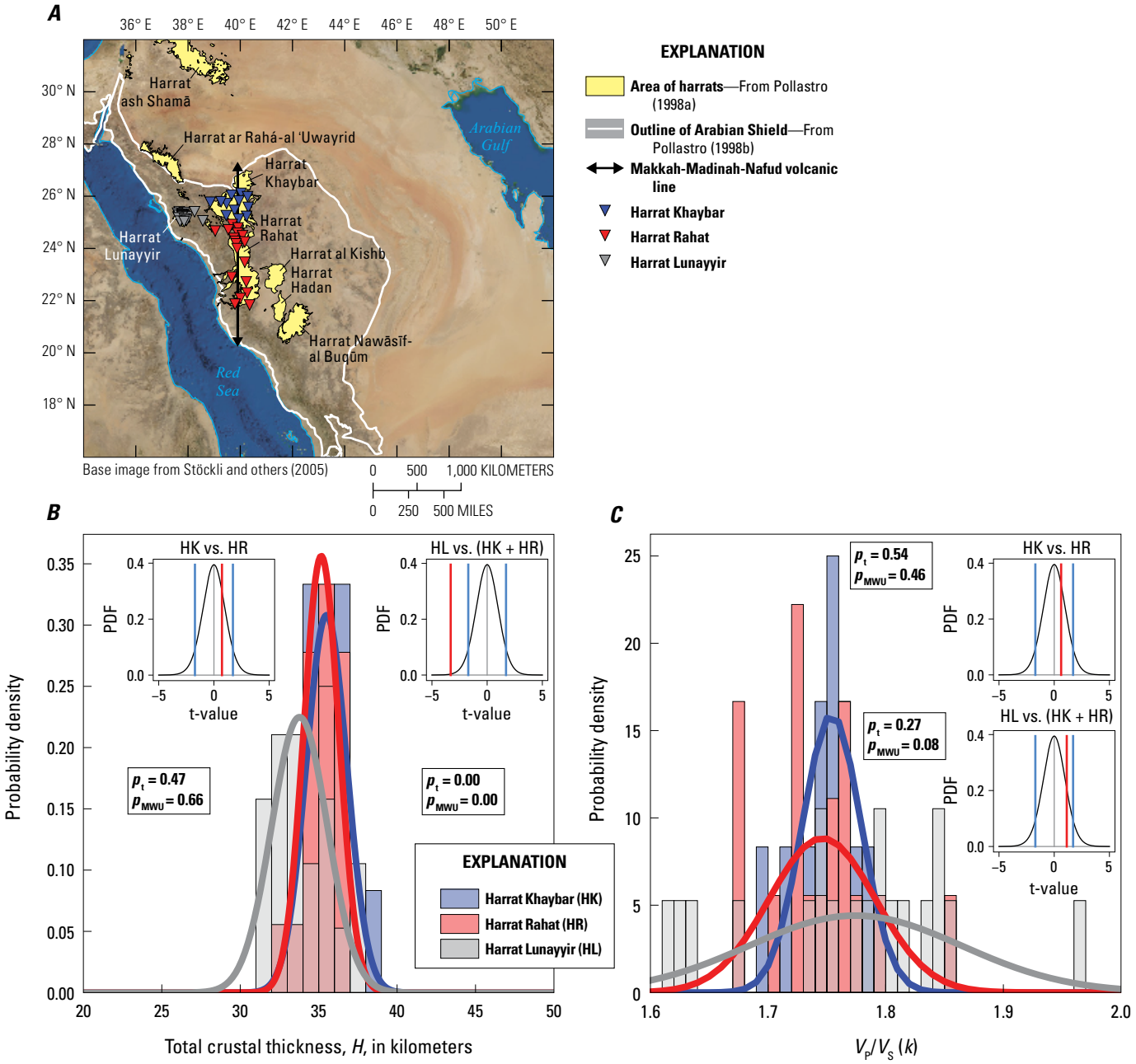

Figure 30. Map and histograms showing a comparison of Harrats Khaybar (HK) and Rahat (HR), and of both with Harrat Lunayyir (HL) in the Kingdom of Saudi Arabia. *A*, Map of harrat seismic stations. Harrat Khaybar and Harrat Rahat comprise the Makkah-Madīnah-Nafud (MMN) volcanic line. *B*, Histograms of crustal thickness by harrat. Transparent colors allow the overlap to be visible. Gaussian curves are fits to the data. Inset plots show the t-tests, plotting the probability density function (PDF) of the Student distribution for the two datasets. Blue vertical bars are 95 percent confidence bounds; the red bar is the t-value of this comparison. If the red bar is within the blue bars, then the null hypothesis (H_0) is accepted, otherwise the alternative hypothesis (H_t, that the distributions are different) is accepted (Welch, 1947). Left inset: Harrat Khaybar tested against Harrat Rahat. Right inset: Harrat Lunayyir tested against the MMN stations (Harrats Khaybar and Rahat). *C*, Histograms of V_P/V_S ratio (k) by harrat. Top inset: Harrat Khaybar tested against Harrat Rahat. Bottom inset: Harrat Lunayyir tested against the MMN stations. Total crustal thickness (H) is depth to Mohorovičić discontinuity. We denote the two different p-values as either p_t (t-test) or p_{MWU} (Mann-Whitney U [MWU] test; Mann and Whitney, 1947). $k = V_P/V_S$ where V_P is P-wave velocity and V_S is S-wave velocity.

Next, we compare the western Arabian Shield (H_{total} = 36.0±5.4 km) to the harrats along the MMN line (Harrats Rahat and Khaybar; H_{total} = 35.3±1.2 km) (fig. 31*B*). The western Arabian Shield and the MMN line have the same mean thicknesses (p_t = 0.44), but significantly different distributions (different variance) (p_{MWU} = 0.04), which we reconcile by looking at the spatial distribution of measurements (fig. 31*A*). The MMN line samples the crust in a small belt, so the measurements are tightly grouped around their mean. The western Arabian Shield stations are spread across a much larger region, including north to the Dead Sea Transform and south nearly to the Yemen flood basalts, and thus has a more diverse range of observations. This is the only example we found where the t-test and MWU test give different results and is simply caused by the different definitions of equivalence (same mean versus same distribution of values).

Finally, we compare the entire Arabian Shield (H_{total} = 36.6±4.8 km) and the Arabian Platform (H_{total} = 38.4±3.4 km, including sedimentary cover) (fig. 31*C*). The Arabian Platform, including its sedimentary cover, may be thicker but it is not statistically different than the Arabian Shield (p_t = 0.07, p_{MWU} = 0.21). However, in a comparison of the crystalline crustal thickness alone (fig. 31*D*), the Arabian Platform average is 33.8±3.6 km, which is 2.8 km thinner than and distinct from the Arabian Shield ($p_t << 0.05$, $p_{MWU} << 0.05$). Although this result appears conclusive, it is heavily dependent on the sedimentary cover correction. We tested this by varying the sedimentary correction factor $\frac{\partial \varepsilon}{\partial h_s}$ from −0.3 to −1.0 (corresponding to assumed sedimentary-basin average V_P of 3.5–4.8 km/s) (circle and squares in fig. 7) and found that within this range, the Arabian Platform crystalline crust is always statistically thinner than the Arabian Shield ($0 < p_t < 0.05$, $0 < p_{MWU} < 0.01$) (fig. 31*D*). In the unlikely case that the sedimentary-basin average V_P is greater than 4.8 km/s, the Arabian Platform crystalline crustal thickness would be statistically indistinguishable from the Arabian Shield crustal thickness.

Another potentially confounding factor is that the relative thicknesses of Arabian Platform crystalline crust and Arabian Shield crust may be biased by the station distribution. Plotting crustal thickness versus distance from the Red Sea rift axis (fig. 32*A*) shows that, at the broadest scale, the Arabia Plate thickens from the rifted margin in the west to the Arabian Platform in the east. The group of Arabian Shield stations with H>40 km at distances of 200–400 km from the Red Sea rift axis does not fit this west-to-east thickening trend, in large part owing to a tendency for the measured Arabian Shield thicknesses to increase to the south (fig. 25*A*, 32*C*), reaching a total crustal thickness of more than 45 km close to the Yemen border. Although this southward increase in crustal thickness might be a product of Cenozoic plume magmatism that produced the Yemen flood basalts (Stern and Johnson, 2010), receiver-function results reported by Ahmed and others (2013) yield crustal thicknesses of 34–36 km beneath the

Figure 31 (page 43). Map and histograms showing a comparison of seismic stations located in the Arabian Shield, Arabian Platform, and harrats that comprise the Makkah-Madīnah-Nafud (MMN) volcanic line in the Kingdom of Saudi Arabia. *A*, Map of seismic stations. Stations in the Arabian Shield are separated into eastern and western locations for easier comparison with the MMN line (Harrats Khaybar and Rahat). *B*, Histogram of total crustal thickness (*H*) of harrats on the MMN line versus the western Arabian Shield. Transparent colors allow the overlap to be visible. Gaussian curves are fits to the data. Inset plot in part *B* is the t-test, showing the probability density function (PDF) of the Student distribution for the two datasets. Blue vertical bars are 95 percent confidence bounds; the red bar is the t-value of this comparison. If the red bar is within the blue bars, then the null hypothesis (H_0) is accepted, otherwise the alternative hypothesis (H_1, that the distributions are different) is accepted (Welch, 1947). *C*, Histogram of total crustal thickness of the Arabian Shield (west plus east) versus Arabian Platform. Dark gray line is the Arabian Platform with a sedimentary correction factor of –1.0 (average sedimentary P-wave velocity [$V_{P, sed}$] = 3.5 kilometers per second [km/s]); white line is the preferred correction factor of –0.6 ($V_{P, sed}$ = 4.0 km/s); light gray is correction factor of –0.3 ($V_{P, sed}$ = 4.8 km/s). Inset plot, same as in part *B*. Solid red line corresponds to the t-test performed for the correction factor of –0.6; dashed red line corresponds to the t-test performed for the correction factor of –0.3; dotted red line corresponds to the t-test performed for the correction factor of –1.0. *D*, Histogram of crystalline crustal thickness of the Arabian Shield (west plus east) versus Arabian Platform. Inset plot, same as in part *C*. We denote the two different *p*-values for each line as either p_t (t-test) (Welch, 1947) or p_{MWU} (Mann-Whitney U [MWU] test; Mann and Whitney, 1947). Total crustal thickness (*H*) is depth to Mohorovičić discontinuity (Moho).

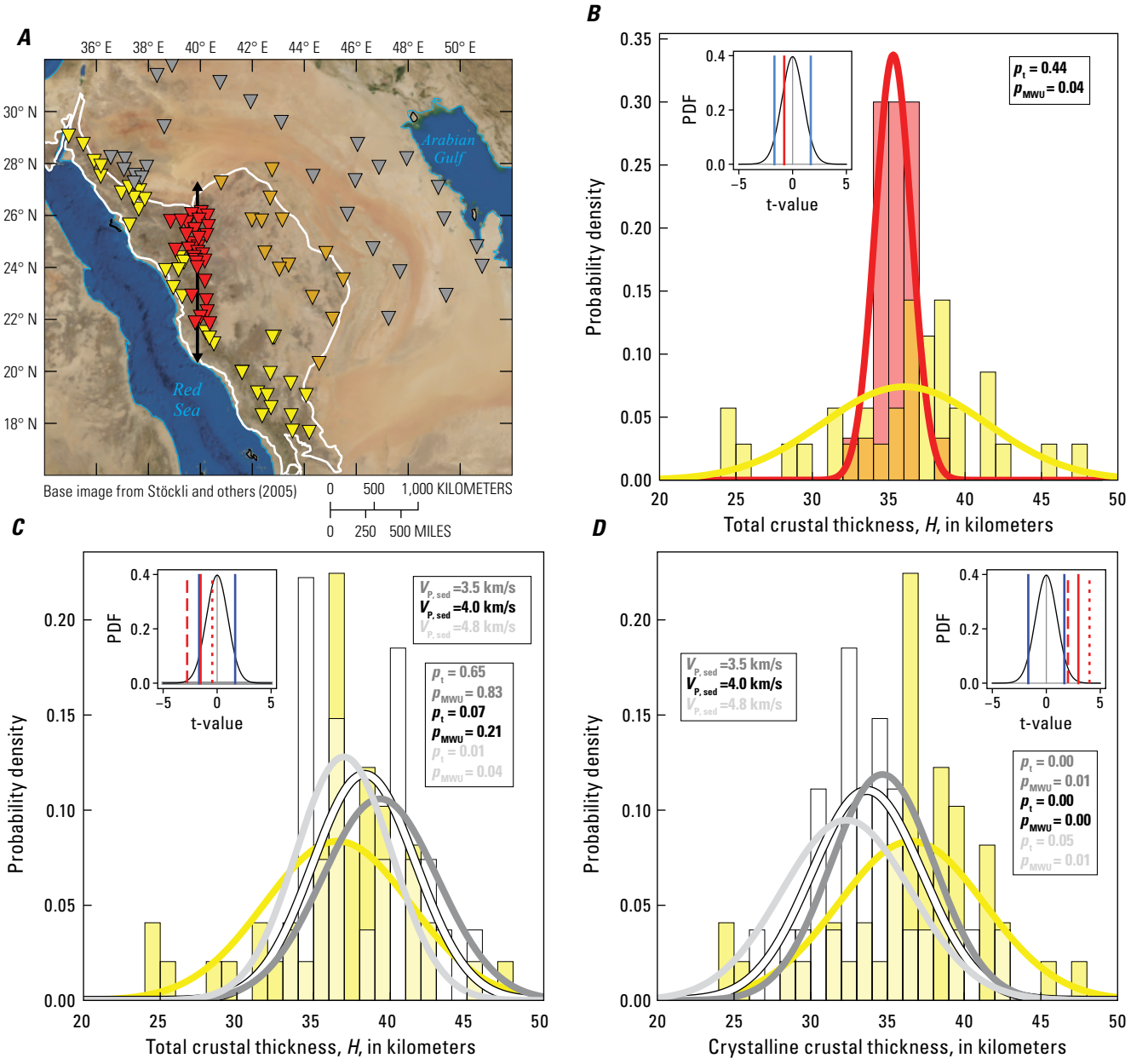

EXPLANATION

A

- **Outline of Arabian Shield**—From Pollastro (1998b)
- **Makkah-Madinah-Nafud volcanic line**
- **Seismic stations by geologic setting**
  - Western Arabian Shield
  - Eastern Arabian Shield
  - Harrats on MMN line
  - Arabian Platform

B

- **Harrats on MMN line**
- **Western Arabian Shield**

C* and *D

- **Arabian Shield**
- **Arabian Platform**

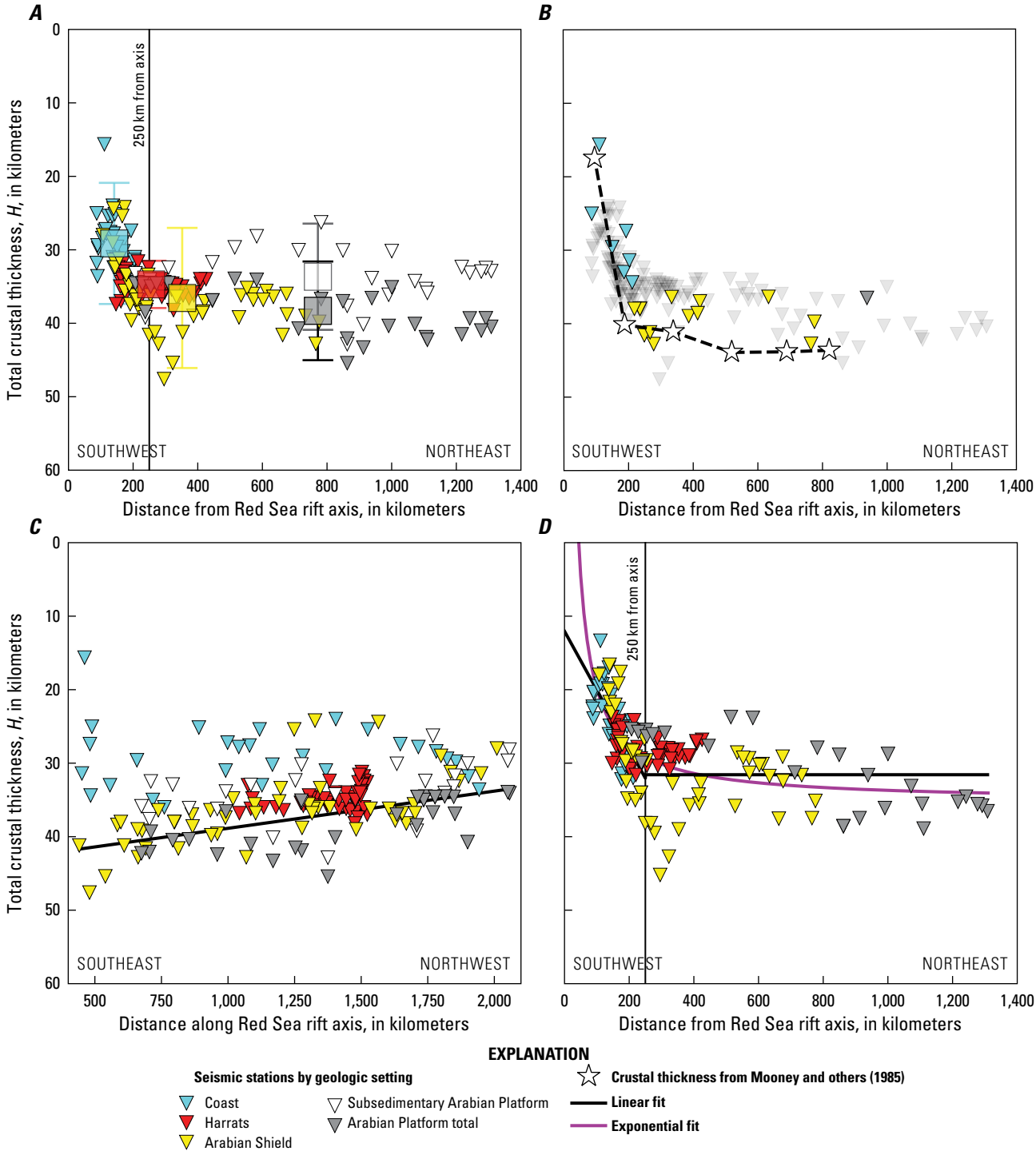

Figure 32. Plots of crustal thickness versus distance parallel and orthogonal to the Red Sea rift axis (see locations in fig. 1*A*). Note crustal thickness increases downward, so plots are comparable with the crustal cross section (fig. 33). *A*, Single-station crustal thickness estimates orthogonal to the Red Sea rift axis by geologic setting. For Arabian Platform stations, we plot both total crustal (gray) and subsedimentary crystalline crustal (white) thicknesses. Squares are regional averages with 2 standard deviation (2σ) error bars. *B*, Same as part *A* with crustal thickness values from Mooney and others (1985) added. All stations more than 125 kilometers (km) away from the Mooney and others (1985) profile are shown by transparent gray symbols; Arabian Platform crystalline crustal thicknesses are omitted. *C*, Crustal thickness parallel to the Red Sea rift axis; distance increases northward. Black line is a linear fit to data points that are more than 250 km away from the Red Sea rift axis; slope is –0.005 km/km. *D*, Same as part *A* with the –0.005 km/km southeast-northwest trend removed from all data points. Purple line is the best-fit exponential line to all data points; horizontal black line is average crustal thickness of all stations >250 km from the Red Sea rift axis; black line with slope of 0.08 km/km is the best-fit line to all stations <250 km from the Red Sea rift axis.

Yemen Highlands, closer to the plume center, confounding simple interpretations of plume magmas having thickened the crust. The southward increase in thickness toward the Yemen border is also seen in the results of active-source seismic studies (Mooney and others, 1985) (fig. 1*A*) that show greater Arabian Shield thicknesses than determined in this study (fig. 32*B*). If we limit the comparison to only southern stations that are within 125 km of Mooney and others' (1985) refraction profile (fig. 32*B*), the discrepancy largely disappears. A linear fit to the crustal thickness of all stations that are more than 250 km from the Red Sea rift axis (fig. 32*C*) shows the crust thins northward at 0.005 km/km. If this northward-thinning trend is representative of the whole Arabia Plate, then the bias in station distribution, with the centroid of Arabian Shield stations located ~200 km south of the centroid of Arabian Platform stations, would explain 1 km of the observed thickness difference between the crystalline crust of the Arabian Platform and Shield. It is possible that when more data become available for the Arabian Platform in southern Saudi Arabia (especially in Ar Rub' al Khālī [Empty Quarter]), the Arabian Shield and the Arabian Platform will be found to be statistically indistinguishable. We note that carrying out the same analysis on spatial averages of the data (instead of station averages) does change the amount of weight different stations contribute to the analysis but does not change the final results.

The observation that crustal thickness increases with distance from the Red Sea rift (fig. 32*A*) remains apparent after correcting all data for 0.005 km/km northward-thinning (fig. 32*D*). These data have the visual appearance of, and can be fit with, an exponential curve (fig. 32*D*). An exponential increase in thickness away from the Red Sea rift is appropriate for an oceanic plate cooling model, but there is no geologic expectation that crustal thickness be controlled by rifting far from the plate interior. We therefore also fit the data with two straight lines: a best-fit line of arbitrary slope (0.08 km/km) for all stations within 250 km of the Red Sea rift axis and a best-fit horizontal line (average thickness) for all stations farther than 250 km from the Red Sea rift axis. That these lines intersect at 250 km from the Red Sea rift reinforces the choice of this distance as the boundary between crust that has been thinned by Red-Sea-rifting processes and the Arabia Plate interior that is unaffected by rifting. The Great Escarpment (fig. 1*B*) that is the geomorphic expression of the rift boundary is approximately 250 km from the Red Sea rift axis (fig. 1*A*), indicating that Red Sea rifting of the Arabia Plate margin extends minimally eastward of its surface geomorphic expression, restricted to a region no broader at depth than at the surface. Excepting Harrat Lunayyir, the harrats lie farther to much farther than 250 km from the Red Sea rift axis, indicating little or no crustal thinning and passive extension contributions to magma generation.

Conclusions

Receiver functions contain valuable information on crustal properties, and extracting that information is straightforward beneath stations with low noise on crust that has relatively simple structure. We have extended use of this method to stations with higher noise and locations with thick surficial sediments by employing three steps: (1) examine each receiver function for quality and retain only the reliable ones, (2) evaluate the stability of the solution depending on different stacking weights for three well-recorded P-to-S-wave converted phases, and (3) employ more advanced forms of the *H-k* stacking algorithm. These three steps must be done in a self-consistent manner that honors the original waveforms. Finally, it is vital to correct crustal thickness estimates for the effects of overlying lower wavespeed sedimentary sections.

Previously available measurements of crustal thickness within Saudi Arabia have either been sparse, low resolution, or highly localized. The P-wave receiver function analysis presented here fills this gap by providing new estimates on the thickness and V_P/V_S ratio of the crust beneath Saudi Arabia using the Saudi Geological Survey seismic array.

The analysis leads to the following conclusions (with 1σ uncertainties reported here; summarized in fig. 33):

1. The thicknesses of the Arabian Shield and Platform crust are 36.6±4.8 km and 38.4±3.4 km, respectively. The average value of the Arabian Shield is on the lower end of global averages for continental shields (40±7.0 km; Mooney and others, 1998), possibly owing to surface erosion during uplift or, in part, to the effects of Red Sea rifting at its western margin. The thickness of the crust of the Arabian Platform matches the global average for continental platforms (39.0±7.0 km; Mooney and others, 1998).
2. The subsedimentary crystalline crustal thickness of the Arabian Platform has an average thickness of 33.8±3.6 km. This value has greater uncertainty owing to the uncertain nature of the sedimentary corrections, but in contrast to some previous estimates (Stern and Johnson, 2010), this value suggests the subsedimentary Arabian Platform crust is ~10 percent (~3 km) thinner than the Arabian Shield.
3. The crust of the harrats has an average thickness of 34.7±1.6 km, which is between that expected for extended crust and shields (Mooney and others, 1998). The harrats have the same thickness as the Arabian Shield at comparable distances from the Red Sea rift margin, implying negligible crustal growth by harrat volcanism. In contrast, Arabian Shield stations closest to Yemen show the largest thicknesses, possibly representing significant crustal growth by Cenozoic

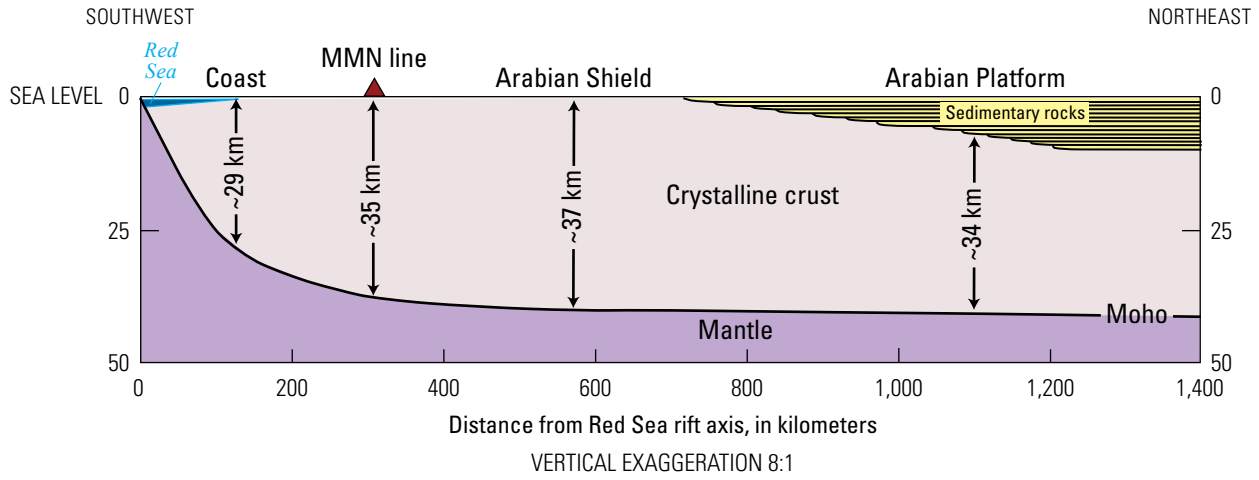

Figure 33. Generalized cross section from the Red Sea rift axis across the Arabia Plate, Kingdom of Saudi Arabia. Location is approximately orthogonal to the Red Sea rift axis (see aqua line in fig. 1*A*). Moho, Mohorovičić discontinuity; MMN line, Makkah-Madīnah-Nafud volcanic line.

plume magmatism; however, crustal thickening does not continue farther southward into the Yemen Highlands closer to the plume center (Ahmed and others, 2013), confounding a simple relation.

4. In contrast to a previous interpretation (Tang and others, 2016), the harrats do not have elevated V_P/V_S ratios with respect to the rest of the Arabian Shield. Nor is it possible to statistically distinguish the crustal thickness of the different terranes that form the Arabian Shield.

5. Thinning of the Arabia Plate extends to (about) the Great Escarpment, diminishing eastward and suggesting uniform extension that is strongly focused beneath the Red Sea Rift axis.

Acknowledgments

We thank Rufus Catchings (U.S. Geological Survey) and Gary Chulick for their useful reviews. The authors also thank Tianze Liu (Scripps Institution of Oceanography) for valuable discussions, which improved the detail, thoroughness, and completeness of this chapter.

References Cited

Ahmed, A., Tiberi, C., Leroy, S., Stuart, G.W., Keir, D., Sholan, J., Khanbari, K., Al-Ganad, I., and Basuyau, C., 2013, Crustal structure of the rifted volcanic margins and uplifted plateau of western Yemen from receiver function analysis: Geophysical Journal International, v. 193, p. 1673–1690, https://doi.org/10.1093/gji/ggt072.

Al-Damegh, K., Sandvol, E., and Barazangi, M., 2005, Crustal structure of the Arabian plate—New constraints from the analysis of teleseismic receiver functions: Earth and Planetary Science Letters, v. 231, nos. 3–4, p. 177–196, https://doi.org/10.1016/j.epsl.2004.12.020.

Almalki, K.A., and Bantan, R.A., 2016, Lithologic units and stratigraphy of the Farasan islands, southern Red Sea: Carbonates and Evaporites, v. 31, no. 2, p. 115–128, https://doi.org/10.1007/s13146-015-0247-4.

Artemieva, I., 2011, Lithosphere—An interdisciplinary approach: Cambridge, Cambridge University Press, 794 p.

Blanchette, A.R., Klemperer, S.L., Mooney, W.D., and Zahran, H.M., 2018, Two-stage Red Sea rifting inferred from mantle earthquakes in Neoproterozoic lithosphere: Earth and Planetary Science Letters, v. 497, p. 92–101, https://doi.org/10.1016/j.epsl.2018.05.048.

Blanchette, A.R., Klemperer, S.L., and Mooney, W.D., 2023, Crustal thickness and the V_P/V_S ratio within the Arabia Plate from P-wave receiver functions at 154 broadband seismic stations: U.S. Geological Survey Open-File Report 2023–1042, 325 p., https://doi.org/10.3133/ofr20231042.

Bosworth, W., 2015, Geological evolution of the Red Sea—Historical background, review and synthesis, *in* Rasul, N.M., and Stewart, I.C.F., eds., The Red Sea: Berlin, Springer-Verlag, p. 45–78.

Bosworth, W., Huchon, P., and McClay, K., 2005, The Red Sea and Gulf of Aden Basins, *in* Catuneanu, O., Guiraud, R., Eriksson, P., Thomas, B., Shone, R., and Key, R., eds., Phanerozoic evolution of Africa: Journal of African Earth Sciences, v. 43, p. 334–378.

Brew, G.E., Litak, R.K., Seber, D., Barazangi, M., Al-Imam, A., and Sawaf, T., 1997, Basement depth and sedimentary velocity structure in the northern Arabian platform, eastern Syria: Geophysical Journal International, v. 128, no.3, p. 617–631, https://doi.org/10.1111/j.1365-246X.1997.tb05323.x.

Brocher, T.M., 2005, Empirical relations between elastic wavespeeds and density in the Earth's crust: Bulletin of the Seismological Society of America, v. 95, no. 6, p. 2081–2092, https://doi.org/10.1785/0120050077.

Camp, V.E., Hooper, P.R., Roobol, M.J., and White, D.L., 1987, The Madinah eruption, Saudi Arabia—Magma mixing and simultaneous extrusion of three basaltic chemical types: Bulletin of Volcanology, v. 49, no. 2, p. 489–508, https://doi.org/10.1007/BF01245475.

Camp, V E., and Roobol, M.J., 1992, Upwelling asthenosphere beneath western Arabia and its regional implications: Journal of Geophysical Research, Solid Earth, v. 97, no. B11, p. 15255–15271, https://doi.org/10.1029/92JB00943.

Camp, V.E., Roobol, M.J., and Hooper, P.R., 1991, The Arabian continental alkali basalt province, Part II—Evolution of Harrats Khaybar, Ithnayn, and Kura, Kingdom of Saudi Arabia: Geological Society of America Bulletin, v. 103, no. 3, p. 363–391, https://doi.org/10.1130/0016-7606(1991)103<0363:TACABP>2.3.CO;2.

Champion, D.E., Downs, D.T., Stelten, M.E., Robinson, J.E., Sisson, T.W., Shawali, J., Hassan, K., and Zahran, H.M., 2023, Paleomagnetism of the northern Harrat Rahat volcanic field, Kingdom of Saudi Arabia—Geologic unit correlations and geomagnetic cryptochron identifications, chap. H *of* Sisson, T.W., Calvert, A.T., and Mooney, W.D., eds., Active volcanism on the Arabian Shield—Geology, volcanology, and geophysics of northern Harrat Rahat and vicinity, Kingdom of Saudi Arabia: U.S. Geological Survey Professional Paper 1862 [also released as Saudi Geological Survey Special Report SGS–SP–2021–1], 31 p., https://doi.org/10.3133/pp1862H.

Coleman, R.G., 1993, Geologic evolution of the Red Sea: Oxford Monographs on Geology and Geophysics, v. 24, 186 p.

Crameri, F., Shephard, G.E., and Heron, P.J., 2020, The misuse of colour in science communication: Nature communications, v. 11, no. 1, p. 1–10, https://doi.org/10.1038/s41467-020-19160-7.

Crotwell, H.P., 2007, High data volume seismology—Surviving the avalanche: Columbia, S.C., University of South Carolina, Ph.D. dissertation, 86 p.

DESERT Group, Weber, M., Abu-Ayyash, K., Abueladas, A., Agnon, A., Al-Amoush, H., Babeyko, A., Bartov, Y., Baumann, M., Ben-Avraham, Z., Bock, G., Bribach, J., El-Kelani, R., Förster, A., Förster, H.-J., Frieslander, U., Garfunkel, Z., Grunewald, S., Götze, H.J., Haak,V., Haberland, C., Hassouneh, M., Helwig, S., Hofstetter, A., Jäckel, K.-H., Kesten, D., Kind, R., Maercklin, N., Mechie, J., Mohsen, A., Neubauer, F.M., Oberhänsli, R., Qabbani, I., Ritter, O., Rümpker,G., Rybakov, M., Ryberg, T., Scherbaum, F., Schmidt, J., Schulze, A., Sobolev, S., Stiller, M., Thoss, H., Weckmann, U., and Wylegalla, K., 2004, The crustal structure of the Dead Sea Transform: Geophysical Journal International, v. 156, no. 3, p. 655–681, https://doi.org/10.1111/j.1365-246X.2004.02143.x.

Dietterich, H.R., Downs, D.T., Stelten, M.E., and Zahran, H., 2018, Reconstructing lava flow emplacement histories with rheological and morphological analysis: the Harrat Rahat volcanic field, Kingdom of Saudi Arabia. Bulletin of Volcanology, v. 80, https://doi.org/10.1007/s00445-018-1259-4.

Dietterich, H.R., Downs, D.T., and Stelten, M.E., 2023, Lava flow emplacement in Harrat Rahat with implications for eruptions in mafic volcanic fields, chap. E *of* Sisson, T.W., Calvert, A.T., and Mooney, W.D., eds., Active volcanism on the Arabian Shield—Geology, volcanology, and geophysics of northern Harrat Rahat and vicinity, Kingdom of Saudi Arabia: U.S. Geological Survey Professional Paper 1862 [also released as Saudi Geological Survey Special Report SGS–SP–2021–1], 49 p., https://doi.org/10.3133/pp1862E.

Earle, P.S., and Shearer, P.M., 1994, Characterization of global seismograms using an automatic-picking algorithm: Bulletin of the Seismological Society of America, v. 8, no. 2, p. 366–376, https://doi.org/10.1785/BSSA0840020366.

El-Isa, Z., Mechie, J., Prodehl, C., Makris, J., and Rihm, R., 1987, A crustal structure study of Jordan derived from seismic refraction data: Tectonophysics, v. 138, nos. 2–4, p. 235–253, https://doi.org/10.1016/0040-1951(87)90042-4.

Endo, E., Zahran, H., Nofal, H., and Hadidy, S., 2007, The Saudi national seismic network: Seismological Research Letters, v. 78, no. 4, p. 439–445, https://doi.org/10.1785/gssrl.78.4.439.

Fay, M.P., and Proschan, M.A., 2010, Wilcoxon-Mann-Whitney or t-test? On assumptions for hypothesis tests and multiple interpretations of decision rules: Statistics surveys, v. 4, no. 1, p. 1–39, https://doi.org/10.1214/09-SS051.

Healy, J.H., Mooney, W.D., Blank, H.R., Gettings, M.E., Kohler, W.M., Lamson, R.J., and Leone, L.E., 1983, Saudi Arabian seismic deep-refraction profiles; final project report (no. 83-390): U.S. Geological Survey Open-File Report 83-390, https://doi.org/10.3133/ofr83390.

Hughes, G.W.G., and Johnson, R.S., 2005, Lithostratigraphy of the Red Sea region: GeoArabia, v. 1, no. 3, p. 49–126, accessed October 8, 2021, at https://pubs.geoscienceworld.org/geoarabia/article/10/3/49/566898/Lithostratigraphy-of-the-Red-Sea-Region.

Julià, J., Ammon, C.J., and Herrmann, R.B., 2003, Lithospheric structure of the Arabian Shield from the joint inversion of receiver functions and surface-wave group velocities: Tectonophysics, v. 371, nos. 1–4, p. 1–21, https://doi.org/10.1016/S0040-1951(03)00196-3.

Johnson, P.R., Halverson, G.P., Kusky, T.M., Stern, R.J., and Pease, V., 2013, Volcanosedimentary basins in the Arabian–Nubian Shield—Markers of repeated exhumation and denudation in a Neoproterozoic accretionary orogen: Geosciences, v. 3, p. 389–445, https://doi.org/10.3390/geosciences3030389.

Karplus, M.S., Klemperer, S.L., Zhao, W., Kind, R., Wu, Z., Mechie, J., Shi, D., Browne, L.D., Chen, C., Su, H., Xue, G., Sandvol, E., Ni, J., Tilmann, F.J., and Yongshun Y.J., 2019, Receiver-function imaging of the lithosphere at the Kunlun-Qaidam boundary, Northeast Tibet: Tectonophysics, v. 759, p. 30–43, https://doi.org/10.1016/j.tecto.2019.03.015.

Konert, G., Afifi, A.M., Al-Harjri, S.A., and Droste, H.J., 2001, Paleozoic stratigraphic and hydrocarbon habitat of the Arabian Plate: GeoArabia, v. 6, no. 3, p. 407–442.

Langenheim, V.E., Ritzinger, B.T., Zahran, H., Shareef, A., Al-dahri, M., 2019, Crustal structure of the northern Harrat Rahat volcanic field (Saudi Arabia) from gravity and aeromagnetic data: Tectonophysics, v. 750, p. 9–21.

Langenheim, V.E., Ritzinger, B.T., Zahran, H.M., Shareef, A., and Al-Dhahry, M.K., 2023, Depth to basement and crustal structure of the northern Harrat Rahat volcanic field, Kingdom of Saudi Arabia, from gravity and aeromagnetic data, chap. K *of* Sisson, T.W., Calvert, A.T., and Mooney, W.D., eds., Active volcanism on the Arabian Shield—Geology, volcanology, and geophysics of northern Harrat Rahat and vicinity, Kingdom of Saudi Arabia: U.S. Geological Survey Professional Paper 1862 [also released as Saudi Geological Survey Special Report SGS–SP–2021–1], 18 p., https://doi.org/10.3133/pp1862K.

Langston, C.A., 1979, Structure under Mount Rainier, Washington, inferred from teleseismic body waves: Journal of Geophysical Research, Solid Earth, v. 84, no. B9, p. 4749–4762, https://doi.org/10.1029/JB084iB09p04749.

Langston, C.A., 2011, Wave-field continuation and decomposition for passive seismic imaging under deep unconsolidated sediments: Bulletin of the Seismological Society of America, v., 101, no. 5, p. 2176–2190, https://doi.org/10.1785/0120100299.

Ligorría, J.P., and Ammon, C.J., 1999, Iterative deconvolution and receiver-function estimation: Bulletin of the seismological Society of America, v. 89, no. 5, p. 1395–1400, https://doi.org/10.1785/BSSA0890051395.

Mann, H.B., and Whitney, D.R., 1947, On a test of whether one of two random variables is stochastically larger than the other: The Annals of Mathematical Statistics, v. 18, no.1, p. 50–60, https://www.jstor.org/stable/2236101.

Mechie, J., Abu-Ayyash, K., Ben-Avraham, Z., El-Kelani, R., Qabbani, I., Weber, M., and DESIRE group, 2009, Crustal structure of the southern Dead Sea basin derived from project DESIRE wide-angle seismic data: Geophysical Journal International, v. 17, no. 1, 457–478, https://doi.org/10.1111/j.1365-246X.2009.04161.x.

Miller, M.S., O'Driscoll, L.J., Porritt, R.W., and Roeske, S.M., 2018, Multiscale crustal architecture of Alaska inferred from P receiver functions: Lithosphere, v. 10, no. 2, 267–278, https://doi.org/10.1130/L701.1.

Mohsen, A., Asch, G., Mechie, J., Kind, R., Hofstetter, R., Weber, M., Stiller, M., and Abu-Ayyash, K., 2011, Crustal structure of the Dead Sea Basin (DSB) from a receiver function analysis: Geophysical Journal International, v. 184, no. 1, p. 463–476, https://doi.org/10.1111/j.1365-246X.2010.04853.x.

Mohsen, A., Hofstetter, R., Bock, G., Kind, R., Weber, M., Wylegalla, K., Rümpker, G., and DESERT Group, 2005, A receiver function study across the Dead Sea Transform: Geophysical Journal International, v. 160, no. 3, p. 948–960, https://doi.org/10.1111/j.1365-246X.2005.02534.x.

Mooney, W.D., 1984, A traveltime interpretation of the 1978 seismic refraction profile in the Kingdom of Saudi Arabia, *in* Mooney, W.D., and Prodehl, P., eds., Proceedings of the 1980 workshop of the International Association of Seismology and Physics of the Earth's Interior on the seismic modeling of laterally varying structures—Contributions based on data from the 1978 Saudi Arabian refraction profile: U.S. Geological Survey Circular 937, 49–81, https://doi.org/10.3133/cir937.

Mooney, W.D., Gettings, M.E., Blank, H.R., and Healy, J.H., 1985, Saudi Arabian seismic-refraction profile—A traveltime interpretation of crustal and upper mantle structure: Tectonophysics, v. 111, nos. 3–4, p. 173–246, https://doi.org/10.1016/0040-1951(85)90287-2.

Mooney, W.D., Laske, G., and Masters, T.G., 1998, CRUST 5.1—A global crustal model at 5° × 5°: Journal of Geophysical Research, Solid Earth, v. 103, no. B1, p. 727–747, https://doi.org/10.1029/97JB02122.

Neumann van Padang, M., 1963, Arabia and the Indian Ocean—Catalogue of the active volcanoes and solfatara fields: Rome, International Association of Volcanology, v. 16, 64 p.

Ogden, C.S., Bastow, I.D., Gilligan, A., and Rondenay, S., 2019, A reappraisal of the H–κ stacking technique: implications for global crustal structure: Geophysical Journal International, v. 219, no. 3, p. 1491–1513, https://doi.org/10.1093/gji/ggz364.

Pallister, J.S., McCausland, W.A., Jónsson, S., Lu, Z., Zahran, H.M., El Hadidy, S., Aburukbah, A., Stewart, I.C.F., Lundgren, P.R., White, R.A., and Moufti, M.R.H., 2010, Broad accommodation of rift-related extension recorded by dyke intrusion in Saudi Arabia: Nature Geoscience, v. 3, no. 10, p. 705–712, https://doi.org/10.1038/ngeo966.

Pellaton, C., 1981, Geologic map of the Al Madinah quadrangle, Sheet 24D, Kingdom of Saudi Arabia (with text): Saudi Arabian Directorate General of Mineral Resources Geologic Map GM-52C, scale 1:250,000, 19 p.

Pollastro, R.M., 1998a, Bedrock geology of the Arabian Peninsula and selected adjacent areas (geo2bg): U.S. Geological Survey data release, accessed October 15, 2018, at https://catalog.data.gov/dataset/bedrock-geology-of-the-arabian-peninsula-and-selected-adjacent-areas-geo2bg.

Pollastro, R.M., 1998b, Geologic Provinces of the Arabian Peninsula and adjacent areas, 2000 (prv2bg): U.S. Geological Survey data release, accessed October 15, 2018, at https://catalog.data.gov/dataset/geologic-provinces-of-the-arabian-peninsula-and-adjacent-areas-2000-prv2bg.

Roobol, M.J., and Camp, V.E., 1991, Geologic map of the Cenozoic lava fields of Harrats Khaybar, Ithnayn, and Kura, Kingdom of Saudi Arabia: Saudi Arabian Deputy Ministry for Mineral Resources Geoscience Map GM-131, scale 1:250,000 scale, pamphlet 40 p.

Sandvol, E., Seber, D., Barazangi, M., Vernon, F., Mellors, R., and Al-Amri, A., 1998, Lithospheric seismic velocity discontinuities beneath the Arabian Shield: Geophysical Research Letters, v. 25, no. 15, p. 2873–2876, https://doi.org/10.1029/98GL02214.

Savage, M.K., 1998, Lower crustal anisotropy or dipping boundaries? Effects on receiver functions and a case study in New Zealand: Journal of Geophysical Research, Solid Earth, v. 103, no. B7, p. 15069–15087, https://doi.org/10.1029/98JB00795.

Seber, D., Barazangi, M., Chaimov, T.A., Al-Saad, D., Sawaf, T., and Khaddour, M., 1993, Upper crustal velocity structure and basement morphology beneath the intracontinental Palmyride fold-thrust belt and north Arabian platform in Syria: Geophysical Journal International, v. 113, no. 3, p. 752–766, https://doi.org/10.1111/j.1365-246X.1993.tb04666.x.

Schulte-Pelkum, V., and Mahan, K.H., 2014, A method for mapping crustal deformation and anisotropy with receiver functions and first results from USArray: Earth and Planetary Science Letters, v. 402, p. 221–233, https://doi.org/10.1016/j.epsl.2014.01.050.

Stelten, M.E., Downs, D.T., Champion, D.E., Dietterich, H.R., Calvert, A.T., Sisson, T.W., Mahood, G.A., and Zahran, H.M., 2023, Eruptive history of northern Harrat Rahat—Volume, timing, and composition of volcanism over the past 1.2 million years, chap. D *of* Sisson, T.W., Calvert, A.T., and Mooney, W.D., eds., Active volcanism on the Arabian Shield—Geology, volcanology, and geophysics of northern Harrat Rahat and vicinity, Kingdom of Saudi Arabia: U.S. Geological Survey Professional Paper 1862 [also released as Saudi Geological Survey Special Report SGS–SP–2021–1], 46 p., https://doi.org/10.3133/pp1862D.

Stern, R.J., and Johnson, P., 2010, Continental lithosphere of the Arabian Plate—A geologic, petrologic, and geophysical synthesis: Earth-Science Reviews, v. 101, no. 1, p. 29–67, https://doi.org/10.1016/j.earscirev.2010.01.002.

Stöckli, R., Vermote, E., Saleous, N., Simmon, R., and Herring, D., 2005, The Blue Marble Next Generation—A true color earth dataset including seasonal dynamics from MODIS: National Aeronautics and Space Administration Earth Observatory, 13 p., accessed March 10, 2020, at https://earthobservatory.nasa.gov/ContentFeature/BlueMarble/bmng.pdf.

Tang, Z., Julià, J., Zahran, H., and Mai, P.M., 2016, The lithospheric shear-wave velocity structure of Saudi Arabia—Young volcanism in an old shield: Tectonophysics,v. 680, p. 8–27, https://doi.org/10.1016/j.tecto.2016.05.004.

Tang, Z., Mai, P.M., Julià, J., and Zahran, H., 2019, Shear velocity structure beneath Saudi Arabia from the joint inversion of P and S wave receiver functions, and Rayleigh wave group velocity dispersion data: Journal of Geophysical Research: Solid Earth, v. 124, no. 5, p. 4767–4787, https://doi.org/10.1029/2018JB017131.

Thurner, S., Margolis, R., Levander, A., and Niu, F., 2015, PdS receiver function evidence for crustal scale thrusting, relic subduction, and mafic underplating in the Trans-Hudson Orogen and Yavapai province: Earth and Planetary Science Letters, v. 426, p. 13–22, https://doi.org/10.1016/j.epsl.2015.06.007.

Tkalčić, H., Pasyanos, M.E., Rodgers, A.J., Gök, R., Walter, W.R., and Al-Amri, A., 2006, A multistep approach for joint modeling of surface wave dispersion and teleseismic receiver functions—Implications for lithospheric structure of the Arabian Peninsula: Journal of Geophysical Research, Solid Earth, v. 111, no. B11, 25 p., https://doi.org/10.1029/2005JB004130.

ten Brink, U.S., Al-Zoubi, A.S., Flores, C.H., Rotstein, Y., Qabbani, I., Harder, S.H., and Keller, G.R., 2006, Seismic imaging of deep low-velocity zone beneath the Dead Sea basin and transform fault—Implications for strain localization and crustal rigidity: Geophysical Research Letters, v. 33, no. 24, 6 p., https://doi.org/10.1029/2006GL027890

Vernon, F., 1995, Broadband seismic characterization of the Arabian Shield: International Federation of Digital Seismograph Networks [database], https://doi.org/10.7914/SN/XI_1995.

Welch, B.L., 1947, The generalization of students' problem when several different population variances are involved: Biometrika, v. 34, nos. 1–2, p. 28–35, https://doi.org/10.1093/biomet/34.1-2.28.

Yu, Y., Song, J., Liu, K.H., and Gao, S.S., 2015, Determining crustal structure beneath seismic stations overlying a low-velocity sedimentary layer using receiver functions: Journal of Geophysical Research, Solid Earth, v. 120, no. 5, p. 3208–3218, https://doi.org/10.1002/2014JB011610.

Zhu, L., and Kanamori, H., 2000, Moho depth variation in southern California from teleseismic receiver functions: Journal of Geophysical Research, Solid Earth, v.105, no. B2, 2969–2980, https://doi.org/10.1029/1999JB900322.

Moffett Field Publishing Service Center, California
Manuscript approved February 9, 2022
Edited by Lisa Binder and Monica Erdman
Layout and design by Kimber Petersen
Illustration support by Katie Sullivan

Blanchette and others—**Thickness of the Saudi Arabian Crust**—Professional Paper 1862–M

ISSN 1044-9612 (print)
ISSN 2330-7102 (online)
https://doi.org/10.3133/pp1862M